Controlling Hot Carriers in Photoexcited Graphene

Controlling Hot Carriers in Photoexcited Graphene

Xiaoyu Jia

Xiaoyu Jia

MAX-PLANCK-INSTITUT
FÜR POLYMERFORSCHUNG

Controlling Hot Carriers in Photoexcited Graphene

ACADEMISCH PROEFSCHRIFT

ter verkrijging van de graad van doctor

aan de Universiteit van Amsterdam

op gezag van de Rector Magnificus

prof. dr. ir. K.I.J. Maex

ten overstaan van een door het College voor Promoties ingestelde commissie,

in het openbaar te verdedigen

op dinsdag 29 juni 2021, te 12.00 uur

door Xiaoyu Jia

geboren te Shandong

Controlling Hot Carriers in Photoexcited Graphene

Dutch title:

Controle van hete ladingsdragers in foto-geëxciteerd grafeen

三人行，必有我师焉。择其善者而从之，其不善者而改之。

——《论语·述而》

When I walk along with two others, they may serve me as my teachers. I will select their good qualities and follow them, their bad qualities and avoid them.

Analects of Confucius
(Translated by James Legge)

Contents

Introduction

Graphene, a single layer of carbon atoms in a honeycomb lattice, has shown to have many superb physical properties since its first experimental demonstration in 2004 [1–3]. For instance, graphene has been reported to possess ultrahigh charge carrier mobility, up to $350,000 \text{ cm}^2\text{V}^{-1}\text{s}^{-1}$ at room temperature [4], owing to the massless nature of charge carriers in graphene. In addition, the conduction band of graphene meets its valence band at the so-called Dirac point, i.e., it is a semimetal. Thanks to its gapless properties, graphene's optical photoresponse covers a wide range of electromagnetic spectrum from ultraviolet, visible, infrared, terahertz (THz), even to gigahertz (GHz) and microwave frequencies. These remarkable electronic and optical properties of graphene provide exciting opportunities for various optoelectronic devices. To date, graphene has been integrated into different applications, including transparent electrodes for solar energy harvesting and ultrasensitive and broadband photodetectors and plasmonic applications [5–9].

Ultrafast dynamics of photoexcited charge carriers, in particular, the ultrafast hot carrier cooling processes in graphene are relevant for both fundamental physics studies and practical applications [10–14]. Following optical excitation, charge carriers in graphene can be heated up efficiently in sub-100 femtosecond (fs) timescale, leading to the generation of hot electrons with a defined electron temperature obeying Fermi-Dirac distribution [15,11,13]. Subsequently, these hot carriers cool down in a few picoseconds (ps) or sub-picosecond by dissipating their energy into the environment via, e.g., phonon emissions in the lattice and substrate [16,17]. Both fast and slow dynamics of hot

carriers in graphene could be desirable, depending on the specific application. For instance, long-lived hot carriers following photoexcitation can increase the photoresponse for hot carrier-based photodetection applications. On the other hand, other applications such as ultrafast electrical or optical modulators could benefit from a fast photoresponse, i.e., short-lived hot carriers in photoexcited graphene, leading to a larger modulation bandwidth and higher speed [18]. Therefore, it is crucial to understand the mechanism underlying the hot-carrier cooling process in photo-excited graphene and further achieve effective control over the hot carrier lifetime.

Outline of this thesis

This thesis aims to understand and further control the hot carrier cooling dynamics in several unique graphene systems employing THz spectroscopy. The thesis contains the following chapters:

Chapter 1: We review the related fundamental theory of graphene and its charge carrier dynamics following optical excitation, with a particular focus on the energy relaxation mechanisms of hot carriers in graphene, via, e.g., optical and acoustic phonon emission and disorder-assisted (so-called "supercollision") cooling.

Chapter 2: We present the working principle of our experimental technique – THz spectroscopy. We show fundamentals on the THz generation and detection. We discuss how the photoconductivity dynamics measured by THz spectroscopy can serve as a powerful probe to study the ultrafast hot carrier dynamics in graphene with sub-picosecond time resolution.

Chapter 3: The first experimental chapter deals with the intrinsic cooling dynamics and mechanism in high-quality graphene samples with/without interactions to the substrate. Previously, hot-carrier cooling is reported to be fast, with a $2 - 4$ ps cooling time, in graphene supported by substrates. There are many scenarios to account for the fast cooling, including substrate cooling and defect-assisted acoustic phonon emission (so-called "supercollision" cooling) in graphene. To study the intrinsic hot-carrier cooling dynamics in graphene, we should exclude these extrinsic effects. In this chapter, we achieve this by studying the hot-carrier cooling in one high-quality graphene system – suspended graphene single crystals. The high enough mobility of such graphene ($> 10{,}000 \, \mathrm{cm^2 V^{-1} s^{-1}}$) indicates the disorder density is low enough that "supercollision" cooling is inefficient. Furthermore, in this system, the coupling to the substrate is absent (as the sample is suspended). After excluding these extrinsic factors, we still observe an efficient cooling process with a cooling time of a few picoseconds. To account for the result, we propose that hot carriers in the high-energy tail in the hot-carrier distributions can strongly couple to optical phonons, which effectively dissipates energy from hot carriers. Critically, the electronic system can continuously re-thermalize, creating hot carriers that can further couple to optical phonons. We develop an analytical model that explains the observed dynamics, where cooling is ultimately limited by optical-to-acoustic phonon coupling.

Chapter 4: To achieve control over the carrier dynamics, we study the hot-carrier dynamics of graphene in a series of dielectric solvents using optical pump-THz probe spectroscopy. The results show that graphene's hot-carrier cooling can be controlled by varying the environmental dielectric constant ϵ:

the cooling time in graphene is found to increase with ϵ (for $\epsilon < 20$). The observation may be rationalized by a physical picture in which the high interfacial dielectrics suppress the electron-electron scattering. This gives rise to the direct cooling of nonthermalized hot carriers via electron-optical phonon emissions. For solvents with ϵ higher than about 20, we found that the cooling time decreases with further increasing ϵ. We explain the results by arguing that in the high dielectric regime, the actual ϵ experienced by graphene at the interface is much lower than the bulk due to immobilization of the molecules in solvents and/or the ϵ drops with high frequency.

Chapter 5: We finally explore potential applications of graphene hot-carrier dynamics. We investigate the impact of ubiquitous cations (Li^+, Na^+, K^+, and Ca^{2+}) in aqueous solutions on the hot-carrier response in SiO_2-supported graphene. We find that, without applying any external potential, cations can shift the Fermi energy of initially hole-doped graphene by ~ 200 meV up to the Dirac point, thus counteracting the initial substrate-induced hole doping. Remarkably, the cation concentration and cation hydration complex size determine the kinetics and magnitude of this shift in the Fermi level. Combined with theoretical calculations, we show that the ion-induced Fermi level shift of graphene involves cationic permeation through graphene. The interfacial cations located between graphene and SiO_2 electrostatically counteract the substrate-induced hole doping effect in graphene. These findings will be useful for graphene's comprehensive applications in electrochemical systems.

1 Hot carriers in graphene

Graphene is a single layer of carbon atoms arranged in two-dimensional (2D) honeycomb lattices [19]. Graphene has been studied theoretically for over seventy years and used as an ideal simplification to describe the properties of varied carbon-based materials [20–22] before its experimental discovery. Early studies predicted that graphene and other monolayer 2D atomic lattices do not exist because they were believed to be thermodynamically unstable [19,23]. In 2004, via "peeling off" the top layer of graphite by scotch tape, Konstantin Novoselov and Andre Geim successfully obtained the first monolayer graphene on SiO_2/Si substrates [1,2]. This discovery opened the gate for exploring fascinating physical properties in graphene and many other 2D materials [24].

To date, researchers have explored many properties of graphene, for example, massless charge carriers [2], universal light absorption [25], high electrical mobility [4], and room-temperature quantum Hall effect [3,26]. These properties are associated with the electrons' relativistic behavior in graphene as massless Dirac fermions. In this chapter, we start by reviewing the related fundamental theory of graphene and its charge carrier dynamics following optical excitations. In particular, we pay special attention to the energy relaxation mechanisms of hot carriers in graphene, via, e.g., carrier-carrier scattering, optical and acoustic phonon emission, and disorder-assisted "supercollision".

1.1 Graphene

1.1.1 Massless Dirac fermions in graphene

We start by introducing the electronic band structure of graphene following the references [20,27–30].

One can see graphene as a single layer of lamellar graphite crystal. Mono-layer graphene has a thickness of 3.7 Å, slightly thicker than the distance 3.35 Å between carbon layers in graphite [31]. The crystal structure of graphene is shown in **Figure 1.1a**. The lattice vectors are:

$$a_1 = a\left(\frac{\sqrt{3}}{2}, \frac{1}{2}\right), a_2 = a\left(\frac{\sqrt{3}}{2}, -\frac{1}{2}\right) \tag{1.1}$$
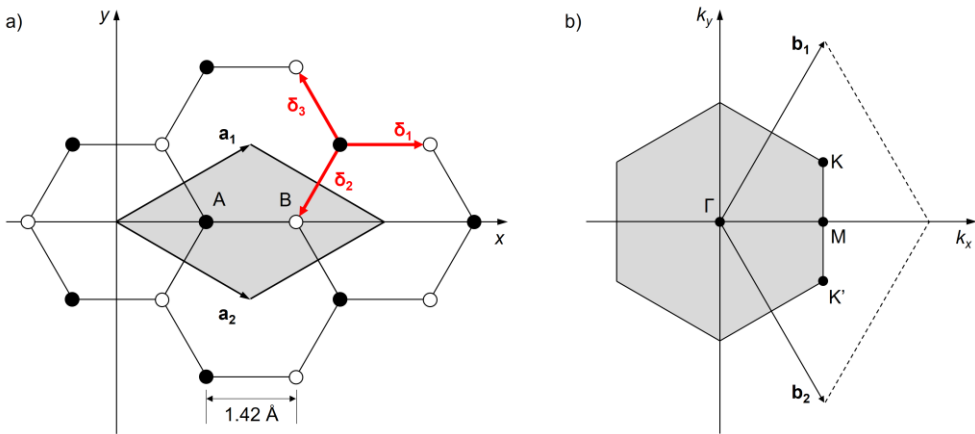
Figure 1.1 | Honeycomb lattice (a) and its Brillouin zone (b) of graphene. A basic unit cell contains two carbon atoms A and B in the lattice structure of graphene. a_1 and a_2 are the lattice vectors. The shaded area marks one unit cell. The corresponding first Brillouin zone (solid hexagonal) also shows a honey-comb structure, where the reciprocal lattice of graphene is defined by b_1 and b_2.

in the (x, y) coordinates, where $a \approx 1.42$ Å is the distance between neighboring carbon atoms. By applying the relation between real and reciprocal space

$\boldsymbol{a_i} \cdot \boldsymbol{b_j} = 2\pi\delta_{ij}$, the corresponding reciprocal lattice vectors can be obtained as:

$$b_1 = \frac{4\pi}{\sqrt{3}a}\left(\frac{1}{2}, \frac{\sqrt{3}}{2}\right), b_2 = \frac{4\pi}{\sqrt{3}a}\left(\frac{1}{2}, -\frac{\sqrt{3}}{2}\right). \qquad (1.2)$$

As shown in **Figure 1.1a**, it is clear that one primitive cell in the graphene lattice contains two carbon atoms. For every single atom, there are four valence electrons, among which three contributes to the in-plane chemical bonding, forming σ bonds via sp^2 hybridization (a combination of $1s$, $2p_x$, and $2p_y$ orbitals). The one remaining electron occupies a $2p_z$ orbital, in the out-of-plane direction. These p_z orbitals are overlapped and together forming two half-filled bands, π and π^* bands, of freely moving electrons [32]. These bands are relevant to most of the electronic properties of graphene.

The band structure of graphene can be calculated using the tight-binding method. Such an approach was first developed by Wallace in 1947 [20], nearly 60 years before discovering graphene [1–3]. In the tight-binding Hamiltonian for electrons in graphene, only electron hopping to the nearest-neighbor atom is considered. Here, one denotes the operator $\hat{a}_i$ $(\hat{b}_j)$ for annihilating an electron at position $\boldsymbol{r}_i$ of sites in sublattice $A(B)$ and similarly $\hat{a}_i^\dagger$ $(\hat{b}_j^\dagger)$ for creating an electron at position $\boldsymbol{r}_j$ of sites in sublattice $A(B)$. One sets the on-site energy to zero. This leads to a Hamiltonian

$$\hat{H} = -t \sum_{i,j} \left(\hat{a}_i^\dagger \hat{b}_j + \hat{b}_j^\dagger \hat{a}_i\right). \qquad (1.3)$$

The nearest-neighbor hopping energy t is 2.7 eV for hopping between different sublattices. The exact value of t does not affect the band calculation results.

Here vectors in the real space for three nearest neighboring atoms for each *A* sublattice atom are introduced

$$\boldsymbol{\delta_1} = a(1,0), \boldsymbol{\delta_2} = \frac{a}{2}\left(-1, -\sqrt{3}\right), \boldsymbol{\delta_2} = \frac{a}{2}\left(-1, \sqrt{3}\right). \tag{1.4}$$

Then one can rewrite **Eq. (1.3)** as

$$\hat{H} = -t \sum_{i \in A} \sum_{\delta} \left(\hat{a}_i^\dagger \hat{b}_{i+\delta} + \hat{b}_{i+\delta}^\dagger \hat{a}_i\right) \tag{1.5}$$

where the operator $\hat{b}_{i+\delta}(\hat{b}_{i+\delta}^\dagger)$ annihilates (creates) an electron at the position $\boldsymbol{r}_i + \boldsymbol{\delta}$, which corresponds to the *B* site. Using

$$\hat{a}_i^\dagger = \frac{1}{\sqrt{\mathcal{N}/2}} \sum_k e^{i\boldsymbol{k}\cdot\boldsymbol{r}_i} \hat{a}_k^\dagger \tag{1.6}$$

where $\mathcal{N}/2$ is the number of *A* sites. Similarly for $\hat{b}_{i+\delta}^\dagger$, one can write the Hamiltonian as

$$\hat{H} = -\frac{t}{\mathcal{N}/2} \sum_{i \in A} \sum_{\delta, k, k'} \left(e^{i(k-k')\cdot r_i} e^{-ik'\cdot\delta} \hat{a}_k^\dagger \hat{b}_{k'} + \text{H.c.}\right) \tag{1.7}$$

where H. c. is the Hermitian conjugate, using

$$\sum_{i \in A} e^{i(k-k')\cdot r_i} = \frac{\mathcal{N}}{2} \delta_{kk'}. \tag{1.8}$$

One has

$$\hat{H} = -t \sum_{\delta, k} \left(e^{-ik\cdot\delta} \hat{a}_k^\dagger \hat{b}_k + e^{ik\cdot\delta} \hat{b}_k^\dagger \hat{a}_k\right). \tag{1.9}$$

Then one can write the Hamiltonian as

$$\hat{H} = \sum_k \boldsymbol{\Psi}^\dagger h(k) \boldsymbol{\Psi}. \tag{1.10}$$

With

$$\boldsymbol{\Psi} = \begin{pmatrix} \hat{a}_{\boldsymbol{k}} \\ \hat{b}_{\boldsymbol{k}} \end{pmatrix}, \boldsymbol{\Psi}^{\dagger} = \begin{pmatrix} \hat{a}_{\boldsymbol{k}}^{\dagger} & \hat{b}_{\boldsymbol{k}}^{\dagger} \end{pmatrix} \tag{1.11}$$

and

$$\boldsymbol{h}(\boldsymbol{k}) = -t \begin{pmatrix} 0 & \Delta_{\boldsymbol{k}} \\ \Delta_{\boldsymbol{k}}^{*} & 0 \end{pmatrix} \tag{1.12}$$

which represents the Hamiltonian in a matrix, where

$$\Delta_{\boldsymbol{k}} = \sum_{\boldsymbol{\delta}} e^{i\boldsymbol{k}\cdot\boldsymbol{\delta}}. \tag{1.13}$$
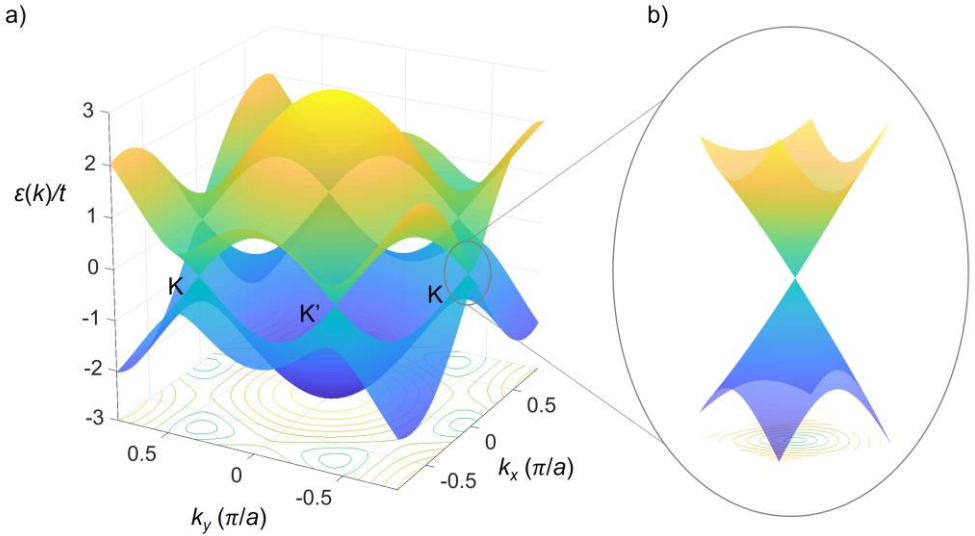
Figure 1.2 | The electronic structure of the honeycomb lattice calculated using the tight-binding approach. (a) First Brillouin zone and band structure of graphene by plotting **Eq. (1.14)**. The energy spectrum is plotted in units of t, introduced in **Eq. (1.3)**. **(b)** Band structure near one of the Dirac points. Blue and yellow colors represent the valence and conduction band correspondingly.

With the eigenvalues $E_{\pm} = \pm t\sqrt{\Delta_{\boldsymbol{k}}\Delta_{\boldsymbol{k}}^{*}}$ of the matrix in **Eq. (1.12)**, one now

calculates it using **Eq. (1.13)**, and gets the expression of energy bands

$$\varepsilon_{\pm}(\boldsymbol{k}) = \pm t \sqrt{1 + 4\cos\left(\frac{3}{2}k_x a\right)\cos\left(\frac{\sqrt{3}}{2}k_y a\right) + 4\cos^2\left(\frac{\sqrt{3}}{2}k_x a\right)}. \tag{1.14}$$

The plus and minus signs stand for conduction and valence band, respectively. At the corners of the first Brillouin zone in the momentum space, $K = (\frac{2\pi}{3a}, \frac{2\pi}{3\sqrt{3}a})$ and $K' = (\frac{2\pi}{3a}, -\frac{2\pi}{3\sqrt{3}a})$, the conduction band touches the valence band, where the K and K' points are the Dirac points (see **Figure 1.1b**).

Dirac points are important for graphene physics since electrons' dispersion near these points has an unusual conical shape (shown in **Figure 1.2**). One can Tayler expand the band structure **Eq. (1.14)** near the Dirac point to obtain the expression to describe such conical dispersion by substituting $k = K + \kappa$, where κ is the wave vector measured relatively to the Dirac point, and $|\kappa| \ll |K|$. k is simply used to devote the wavevector measured relatively to the K (or K') point in graphene, unless it is stated otherwise. This gives:

$$\varepsilon_\pm(\kappa) = \pm\hbar v_g |\kappa| \qquad (1.15)$$

where the v_g is the group velocity of electrons, given by $v_g = \frac{3|t|a}{2\hbar} = 1 \times 10^6$ m/s. Since the same expression can be used to describe the electron energy near K', it shows that near Dirac points, electrons have a two-fold degeneracy. This takes the name of valley degeneracy. Such degeneracy is 2 for graphene.

The group velocity of electrons in graphene does not depend on the energy or momentum, which is the most noticeable difference between electrons following the linear dispersion **Eq. (1.15)** and free electrons in parabolic-like bands. The energy dispersion of a free electron, in fact, relates to the square of its momentum: $\varepsilon(k) = \frac{(\hbar k)^2}{2m}$, where m is the mass of an electron [33]. Therefore one has $v_g = \frac{\hbar k}{m} = \sqrt{2\varepsilon/m}$ for free electrons. In graphene, this velocity equals to Fermi velocity $v_g = v_F$, and is a constant for a relatively wide range

of Fermi energy. Importantly, the energy-momentum dispersion in graphene is an explicit solution of the Dirac equation with a zero mass term and v_F replacing the speed of light.

Next, one derives the density of states (DOS), which is also associated with the dispersion relation. One sets a function $Q(\boldsymbol{k})$ for mathematic purpose, which only depends on $\boldsymbol{k}$ through the energy $\varepsilon(\boldsymbol{\kappa})$. The following relation is found in solid state physics textbooks [34]:

$$v \int \frac{d\boldsymbol{k}}{(2\pi)^n}\, Q(\boldsymbol{k}) = \int d\varepsilon N(\varepsilon)\, Q(\varepsilon) \tag{1.16}$$

where $n = 2$ stands for the dimensionality of the system, which is 2 in the case of graphene, v is the degeneracy of states, and $N(\varepsilon)$ is the DOS. For graphene's conduction band near Dirac points, the integral in **Eq. (1.16)** is (here, the function $Q(\boldsymbol{k})$ is omitted for a compact form):

$$v \int \frac{d\boldsymbol{k}}{(2\pi)^2} = v \int \frac{k dk}{2\pi} = v \int \frac{\frac{\varepsilon}{\hbar v_F} d\left(\frac{\varepsilon}{\hbar v_F}\right)}{2\pi}$$
$$= \int d\varepsilon \frac{v\varepsilon}{2\pi(\hbar v_F)^2} = \int d\varepsilon N(\varepsilon). \tag{1.17}$$

Accordingly, the expression for the DOS is $N(\varepsilon) = \frac{g_s g_v |\varepsilon|}{2\pi(\hbar v_F)^2}$, here $g_s = 2$ is the spin degeneracy and $g_v = 2$ is the valley degeneracy. The $|\varepsilon|$ means that one can obtain the same expression for the valence band but with an opposite sign. Thus, the expression for the DOS of graphene close to the Dirac points is:

$$N(\varepsilon) = \frac{2|\varepsilon|}{\pi(\hbar v_F)^2}. \tag{1.18}$$

The DOS in graphene is linear in energy near Dirac points, shown in **Figure 1.3d**.

1.1.2 Momentum relaxation mechanisms of electrons in graphene

Electrons in high-quality graphene samples can travel with an extraordinarily high velocity due to their relativistic and massless nature. This results in a long mean free path over multiple lattice constants for charge conductions. On the other hand, electrons can scatter as well with impurities and defects in lattice and substrate, phonons, and ripples, etc., present in graphene [32]. All these interactions limit the electron mean free path l, which is proportional to the scattering time τ_{scat}:

$$l = v_F \tau_{scat}. \tag{1.19}$$

By employing the semiclassical Boltzmann transport theory to describe the statistical behavior of the electronic system of disequilibrium, one can gain further insight into the scattering mechanisms and their effects on the electronic conductivity σ [35]:

$$\sigma = \frac{e^2 v_F \tau_{scat}}{\hbar} \sqrt{\frac{n}{\pi}}. \tag{1.20}$$

This equation is valid in doped graphene when the Fermi level E_F is away from the Dirac point. The scattering time τ_{scat} is defined by the average time between two sequential scattering events, which changes the momentum of charge carriers. Following Matthiessen's rule, the scattering rate τ_{scat}^{-1} is the sum of multiple independent scattering channels: $\tau_{scat}^{-1} = \tau_1^{-1} + \tau_2^{-1} + \cdots$. Applying the classical Drude conductivity model, $\sigma = ne\mu_m$, where n is the charge carrier density, e is the elementary charge, and μ_m is the electron mobility, this leads to:

$$\mu_m = \frac{e v_F \tau_{scat}}{\hbar \sqrt{\pi n}} = \frac{e \tau_{scat}}{m^*}. \tag{1.21}$$

To distinguish the zero mass of electron in the band structure, here one uses the cyclotron effective mass m^* in graphene. This effective mass is a result of the semiclassical motion of the electron. The cyclotron effective mass for graphene is typically extracted by measuring electron cyclotron motion in a closed loop in k-space under a magnetic field – Shubnikov-de Haas oscillation [36]. We note that the effective mass usually used for graphene electronic transport properties is this cyclotron effective mass, with a finite value depending on the carrier density [37]. Such effective mass of electrons in graphene has a function with Fermi energy, $m^* = \frac{\hbar k_F}{v_F} = \frac{E_F}{v_F^2}$ [27,29], a fictitious "relativistic" mass [3]. Thus one gets

$$\mu_m = \frac{e\tau_{scat}v_F^2}{E_F}. \tag{1.22}$$

By measuring the mobility μ_m and Fermi energy E_F of graphene experimentally, one can directly estimate the scattering time τ_{scat} and electron mean free path l, using **Eq. (1.19)** and **(1.22)**.

The "extrinsic" scattering mechanisms existing in graphene contain both short- and long-range contributions. Impurities or defects in graphene lattice and substrate contribute to long-range scattering. Coulomb scattering is typically caused by those long-range variations of the electrostatic potential [38,39], which is commonly seen as randomly charged impurities located near the graphene/substrate interface [40]. The scattering time is given by $\tau_{scat} \propto \frac{\sqrt{n}}{n_i}$ for charged impurities in graphene, where n_i is the charged impurity concentration. This leads to the graphene conductivity to be proportional

to n, for long-range scattering. On the other hand, for short-range disorder scattering, the scattering time is given by $\tau_{scat} \propto \frac{1}{n_d\sqrt{n}}$, where n_d is short-range neutral impurity density [38,39]. The conductivity is independent of carrier density for short-range scattering at low carrier densities. In higher carrier densities, the short-range scattering contributes to the sub-linearity of conductivity σ.

The "intrinsic" scattering originates mainly from the electron-phonon scattering in graphene. Lattice vibrations (phonons) inevitably contribute as sources of scattering and limit the charge transport properties for graphene near room temperature [29]. The electron-phonon scattering dominates the carrier transport of high-quality graphene with limited defects, which has a limited amount of extrinsic scattering contributions. Due to the very high energy of optical phonons (~200 meV in graphene [29]), the electron-optical phonon scattering is therefore negligible in the perspective of charge transport at room temperature. Here we only discuss the scattering due to acoustic phonons in graphene near room temperature for two reasons: i) the coupling strength to other phonon modes is too low; ii) the optical phonon modes have too high an energy to provide an effective scattering channel.

The electron-acoustic phonon scattering may be considered quasi-elastic [29]. There are two regimes depending on the degeneracy of the phonon system, which are separated by the Bloch-Grüneisen temperature T_{BG} defined by $k_B T_{BG} = 2\hbar k_F v^{AP}$, where v^{AP} is the acoustic phonon velocity. When the lattice temperature T_L is far above T_{BG} ($T_L \gg T_{BG}$), the phonon system is nondegenerate, which is relevant for our experiments. The relaxation time for electron-acoustic phonon scattering is given by [41–43]

$$\tau_{scat} = \frac{4\hbar^2 v_F}{\sqrt{\pi n}} \frac{\rho_m v^{AP^2}}{D^2} \frac{1}{k_B T_L} \tag{1.23}$$

where $\rho_m = 7.6 \times 10^{-7}$ kg/cm^2 is the mass density of graphene, $v^{AP} \approx 2 \times 10^6$ cm/s is the in-plane acoustic phonon velocity of graphene and D is the screened acoustic deformation potential [43,44].

As a non-polar material, quasi-static deformation of the graphene lattice essentially contributes to the scattering [29]. The deformation potential relates the lattice deformations to the change in energy bands [45]. D is on the order of the atomic energy $\frac{1}{4\pi\varepsilon_0}\frac{e^2}{a}$, which is about 10 eV for graphene. The value of D can be estimated by **Eq. (1.23)**, and are generally higher from experiments in comparison to the theoretical values. For instance, D is found to be 18 ± 1 eV in [46], and 20.5 eV in [47].

Experiments show that the electronic conductivity σ of graphene scales almost linearly with carrier density n and behaves symmetrically for electrons and holes. Moreover, graphene at the charge-neutrality point exhibits a finite quantum-limited minimum conductivity when the Fermi energy equals the Dirac point energy [48–50].

1.1.3 Fermi-Dirac distribution of charge carriers in graphene

Referring to textbook [34], the probability of the one-electron level with energy ε_i being occupied at temperature T_e in an n-electron system follows a Fermi-Dirac distribution given by:

$$f_i^n = \frac{1}{e^{\frac{\varepsilon_i - \mu}{k_B T_e}} + 1} \tag{1.24}$$

where μ is the chemical potential, and k_B is the Boltzmann constant. The total number of electrons n is just the sum of the number of electrons at all energy levels:

$$n = \sum_i f_i = \sum_i \frac{1}{e^{\frac{\varepsilon_i - \mu}{k_B T_e}} + 1}. \tag{1.25}$$

Considering a gas of free and independent electrons, the one-electron levels are specified by the wave vector $\boldsymbol{k}$. In the ground-state ($T_e = 0$) the energy levels are occupied with $\varepsilon(\boldsymbol{k}) \le E_F$, so the ground-state distribution function must be:

$$\lim_{T \to 0} f_k = \begin{array}{ll} 1, & \varepsilon(\boldsymbol{k}) < E_F \\ 0, & \varepsilon(\boldsymbol{k}) > E_F \end{array}. \tag{1.26}$$

In the low temperature limit ($T \to 0$),

$$\lim_{T \to 0} \mu = E_F \tag{1.27}$$

where E_F is the chemical potential at zero temperature, which is called the Fermi energy.

Using the Fermi-Dirac statistics, we can calculate the electron heat capacity by

$$C_e(T_e) = \frac{\partial Q}{\partial T_e}. \tag{1.28}$$

Q is the sum over one-electron levels of ε times the mean number of electrons in the energy level:

$$Q = \int_{-\infty}^{\infty} \varepsilon f(\varepsilon) d\varepsilon \tag{1.29}$$

where $f(\varepsilon)$ is the Fermi function

$$f(\mu, T, \varepsilon) = \frac{1}{e^{\frac{\varepsilon - \mu}{k_B T_e}} + 1}. \tag{1.30}$$

The electron in graphene follows the linear dispersion relation in **Eq. (1.18)**. Thus the total number of electrons in graphene with a certain chemical potential is

$$n_e = \int_0^\infty N(\varepsilon) f_e(\mu, T_e, \varepsilon) d\varepsilon \tag{1.31}$$

where $f_e(\mu, T_e, \varepsilon)$ is the Fermi equation for electrons. Here we use T_e to indicate the electron temperature, to distinguish with the lattice temperature T_L. In graphene, we should consider two types of charge carriers - electrons and holes. Similar to electrons, the Fermi equation for holes reads: $f_h(\mu, T_e, \varepsilon) = \frac{1}{e^{(\varepsilon+\mu)/k_B T_e}+1}$. The total number of charge carrier is:

$$n = \int_0^\infty N(\varepsilon) [(f_e(\mu, T_e, \varepsilon) - f_h(\mu, T_e, \varepsilon)] d\varepsilon. \tag{1.32}$$

The total energy of the charge carriers contains the energy of both electrons and holes. The total energy of the system is

$$Q_{total}(T_e) = \int_0^\infty \varepsilon N(\varepsilon) f_e(\mu, T_e, \varepsilon) d\varepsilon + \int_0^\infty \varepsilon N(\varepsilon) f_h(\mu, T_e, \varepsilon) d\varepsilon. \tag{1.33}$$

1.2 Hot carrier dynamics in graphene

Graphene has been intensively proposed as an ideal platform for next-generation optoelectronics and optical communication systems. The superb properties of graphene both in terms of electrical (high mobility and tunable carrier density) and optical (broadband optical absorption covering a wide range of wavelengths, from optical frequencies to THz [6,51]) are highly suited for high-performance devices in optoelectronics. Moreover, the single atomic feature allows for easy tuning and control of carriers and heat coupling between layers when graphene is fabricated together with other 2D materials into heterostructures [52].
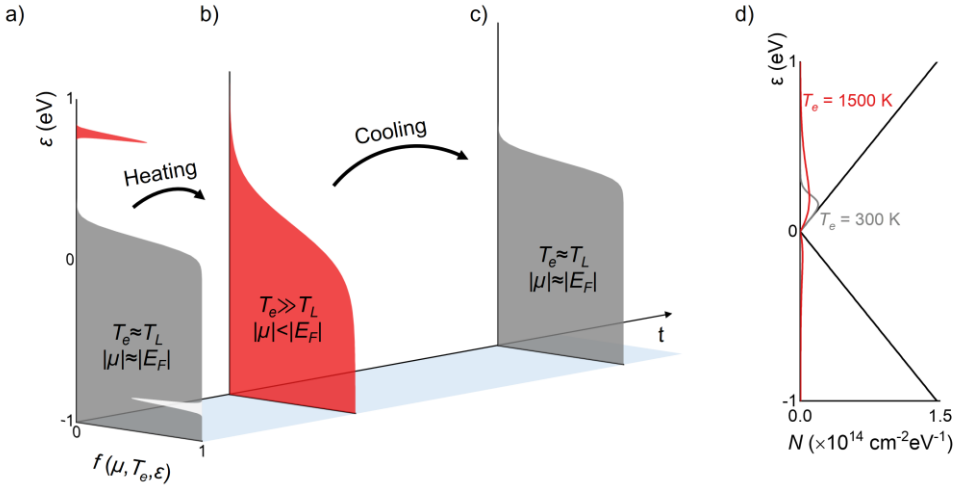
Figure 1.3 | Hot carrier heating and cooling dynamics in graphene. (a) Initially, the carriers are photoexcited with the energy of E_{photon}. From **(a)** to **(b)**, the carriers cascade from high energies down to low energies, losing energy via scattering with carriers near the chemical potential. This process leads to fast thermalization over timescales approximately tens to hundreds of femtoseconds, producing a quasi-thermalized "hot-electron" Fermi-Dirac distribution in **(b)** with high electron temperature (T_e), while the lattice temperature (T_L) stays close to the ambient. The chemical potential μ shifts towards the Dirac point from the Fermi energy E_F due to the particle number conservation. This process is called carrier heating. From **(b)** to **(c)**, cooling mediated by phonons takes place over longer time scales, which relaxes the hot carrier distribution back to equilibrium. **(d)** The occupancy of the states of electrons in the conduction band (above 0 eV) and holes in the valence band (below 0 eV) before the photoexcitation ($T_e = 300$ K, room temperature, shown as the grey curve) and after a carrier heating process ($T_e = 1500$ K, shown as the red curve). Here we illustrate the hot carrier distribution following cooling for a case of *n*-doped graphene ($E_F = 0.2$ eV). The black curve shows the density of states near the Dirac point, plotted by **Eq. (1.18)**. We see that the total density of states is proportional to the energy.

In the early days, researchers have studied the strong thermoelectric response of graphene [53,54]. Recent progress on large-scale graphene production [55,56] and integration with silicon-based photodevices shows increasing

potentials for future success in boosting device performance using graphene [57]. These achievements reveal many novel electric and optoelectronic properties [12,58–64]. Among those studies, the ultrafast hot-carrier effects in graphene show great promise for high speed, and gate-tunable manipulation of charge and energy flows on the nanoscale. Practical and real-world uses based on such hot-carrier effects, including gigahertz bandwidth graphene-silicon phase modulators [65] show more opportunities for this atomically thin material.

This section focuses on the hot carrier cooling process in graphene, relevant for both fundamental physical studies and practical applications [10–14]. This is because both fast and slow dynamics of hot carriers can be helpful, depending on which application graphene aims as mentioned earlier.

The hot-carrier effects in graphene involve two main stages – carrier heating and cooling. As shown in **Figure 1.3a**: for doped graphene (*n*-doping in this case) photons with energy $E_{photon} > 2\mu$ create electron-hole pairs with high-energy above the chemical potential μ [10,14,66,67]. The non-thermalized high-energy carriers then scatter with low-energy carriers heating the electronic system in tens of femtoseconds [10,12–15,66,68–74]. Following the carrier-heating process, the thermalized hot carriers in graphene follow Fermi-Dirac distribution and establish a broadened distribution with a defined electron temperature T_e [12,14,16,58,64,66,75], as shown in **Figure 1.3b**. It is worth noting that the amount of energy captured by the electronic system (and thus the electronic temperature of the hot carrier) is determined by the competition between carrier-carrier scattering and other competing processes (e.g., electron-optical phonon scattering, see later discussion). Following ultrafast

heating, the thermalized hot carriers dissipate their energies into the environment via phonon emissions. This so-called cooling process takes place in several picoseconds and eventually brings the system back to its initial equilibrium (**Figure 1.3c**) [67]. Both processes, the fast electron-electron scattering and the slow cooling through phonon emissions, contribute to optoelectronic devices' performance [12,16,58]. We provide a detailed review of the existing mechanisms on carrier heating and cooling in graphene in the following subsections.

1.2.1 Electron-electron scattering in photoexcited graphene

We begin by examining carrier heating – a process in which the excitation energy flows into the electronic systems to generate thermalized hot carriers in photoexcited graphene. When a laser pulse hits the sample, electrons are excited from the valence to the conduction band by absorbing a photon with energy $E_{photon} = hf$, where h is Planck's constant and f is the photon frequency, illustrated in **Figure 1.4a**. The resulting hot-electron possess excess energy of $E_{photon}/2$ (about 0.8 eV for 800 nm light), which is generally much higher than the Fermi energy E_F induced via electrostatic doping of graphene (up to 100s of meV). Relaxation of the photoexcited electrons occurs via a photoexcitation cascade (electron-electron scattering), forming a hot-electron gas. This has been shown theoretically and experimentally [12,14,66,76]. As illustrated in **Figure 1.4b**, the high-energy electron transfers its energy to multiple electrons close to E_F by exciting them slightly above E_F [68,77]. It turns out that electron-electron scattering is highly efficient and outcompetes other energy dissipation processes (e.g., optical phonon emissions), resulting in large parts of the photon energy E_{photon} stored within the electronic system. The heating efficiency η_{heat} of this process, defined as

the ratio of the energy stored in the electron system versus the total absorbed energy, can exceed 50%, depending on both the Fermi energy of graphene, and the photon energy [12] for the excitations. The number of secondary hot electrons N depends on E_{photon}, and measurements have observed the extraction of multiple carriers per absorbed photon [78].
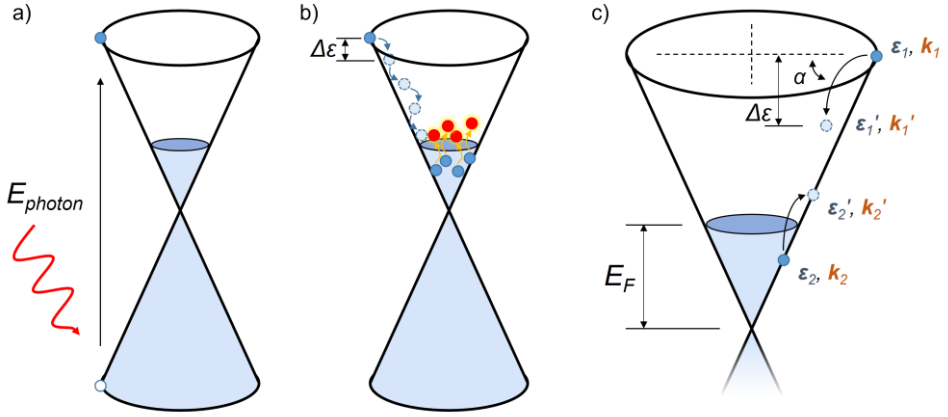
Figure 1.4 | Carrier heating in graphene. (a) Electrons are excited by absorbing a photon with the energy of E_{photon}. **(b)** The carrier heating cascade following the photoexcitation, which heats the electronic system. Each cascade step involves electron-hole pair excitations near the Fermi energy with energy $\Delta\varepsilon$ transferred from the initial photoexcited high-energy electron. **(c)** The scattering process between two electrons at different energy levels involves a photoexcited electron with high energy and momentum $\varepsilon_1 \gg E_F$, $|k_1| \gg k_F$ which is scattered to a lower energy state, which has a momentum k_1' with recoil momentum $q = k_1 - k_1'$ given to an electron near Fermi energy E_F. An angle α between the k_1 and q originates from the Dirac cone structure in three dimensions to ensure momentum conservation [76]. $\Delta\varepsilon$ is the energy transferred from the high energy electron.

Carrier heating caused by such carrier-carrier scattering attracted much attention for graphene-based energy conversion applications [16,68,70,76, 77,80]. Depending on where the electrons are located in the bands, there are

two distinct types of electron-electron scattering allowed in graphene – intra-band electron-electron scattering and interband electron-electron scattering (Auger heating) [80]. While the intraband electron-electron scattering mostly conserves the number of electrons in each band, interband electron-electron scattering generates additional electrons in the conduction band, sometimes called carrier multiplication, when there are an increased amount of interband electron-hole pairs [12]. For graphene with high $|E_F|$, intraband scattering is the dominant mechanism for carrier heating because interband electron-elec-tron scattering is blocked by kinematic constraints arising from energy and momentum conservation [67,76,81]. When $|E_F|$ is close to the Dirac point, in-terband heating can dominate. In addition to scattering process between elec-trons, electron-hole recombination processes also exist due to Auger recombi-nation. Previous studies have analyzed these processes in detail, and the inter-ested readers are referred to reference [68,70,77,82] for further studies.

Analytical explanations of the energy relaxation rate of a photo-excited car-rier via carrier-carrier scattering. have been given by Song *et al.* in [67,76]. The electron-electron scattering rate is expressed by [76]

$$\Gamma(\varepsilon) = \frac{E_F}{\hbar} \int_0^{\varepsilon/E_F} \tilde{P}(x) dx \qquad (1.34)$$

where $\tilde{P}(x) = \hbar P(x)$ is defined as the dimensionless transition probability. $P(x)$ (in units of $\hbar^{-1}$) depends on $\Delta\varepsilon$ essentially via the dimensionless param-eter $x = \Delta\varepsilon/E_F$. And the energy relaxation rate is given by [76]

$$\mathcal{J}_{el}(\varepsilon) = \int_{-\infty}^{\infty} \Delta\varepsilon P(\Delta\varepsilon) d\Delta\varepsilon = \frac{E_F^2}{\hbar} \int_0^{\varepsilon/E_F} x \tilde{P}(x) dx \,. \qquad (1.35)$$

During the thermalization cascade, photoexcited carriers' energy is trans-ferred not only into electrons but also phonons [67]. The main type of energy

relaxation path through phonons after the photoexcitation in a short sub-pico-second timescale is electron-optical phonon emission [69,72,74]. Only the carrier-carrier scattering contributes to carrier heating because the energy lost to phonons has a negligible impact on the temperature due to the $10^3 - 10^4$ times larger phonon heat capacity [82,83]. In other words, the same amount of energy transferred to the phonon system is much less effective in increasing the temperatures.

1.2.2 Electron-optical phonon scattering
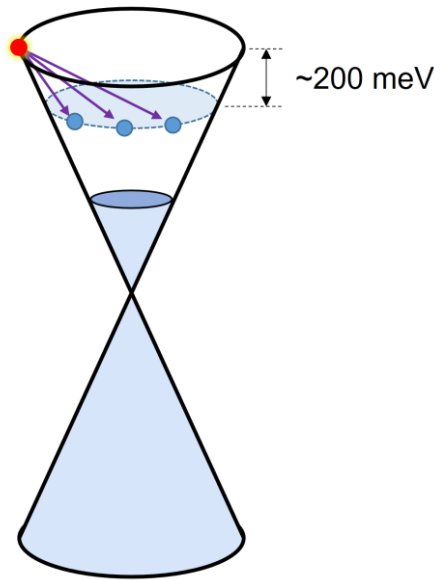
Figure 1.5 | Optical phonon collision cooling. Schematic of electron scattering with optical phonons. The electrons stay in a circle with a constant energy difference from their initial energy level.

As discussed earlier, both carrier-carrier scattering and electron-optical phonon emission happen on a tens to hundreds of femtoseconds timescale after the photoexcitation [76]. The competition between the two relaxations determines the amount of energy that the graphene electronic system captures from

the photoexcited high-energy carriers. We discuss the second energy relaxation pathway, electron-optical phonon emission, in this subsection.

We start to evaluate the collision between the excited electron and an optical phonon (OP). One can write the energy and momentum conservation laws of the initial and final state of an electron emitting an optical phonon as:

$$\varepsilon^{initial} = \varepsilon^{final} + \varepsilon^{OP}$$
$$\boldsymbol{k}^{initial} = \boldsymbol{k}^{final} + \boldsymbol{k}^{OP}.$$

(1.36)

The optical phonons have very little dispersion. Thus their energy ε^{OP} is nearly constant for all momentum $\boldsymbol{k}^{OP}$. This relaxes the momentum conservation condition for hot-carrier cooling: as long as the energy difference between the initial and final state equals the energy of the optical phonon. There are two optical phonon modes at the Γ and K points in graphene with an energy of 0.2 eV and 0.16 eV, respectively [84]. The previous works on hot carrier dynamics generally use the optical phonon energy of 0.2 eV [85,86]. As **Figure 1.5** illustrated in the graphene Dirac cone, the final state of an electron after its emission with optical phonon is a circle with energy about 0.2 eV below the initial state of the excited electron. For an electron at an energy $E_{photon}/2 \approx$ 0.8 eV (e.g., for 800 nm excitation), the electron-optical phonon emission time is less than ~50 fs [87]. This is an efficient energy dissipation pathway compared to other phonon relaxation processes, for example, collisions between electrons and acoustic phonons, which we will discuss later. This collision with optical phonons can only couple with very high energy electrons [69,73,81,85]. Thus if the electron temperature $T_e \lesssim 2000$ K, it is believed that the optical phonon collision becomes inefficient. The required electron scattering time due to optical phonon scattering increases two orders of magnitude to several

picoseconds when the energy of electrons decreases to $\lesssim 0.2$ eV [87]. Therefore, optical phonon scattering occurs during the carrier heating, and the cooling for hot electrons with sufficiently high electron temperature [69,73,81,85].

Similar to carrier-carrier scattering, one can describe the energy relaxation rate for the photoexcited electron at energy ε scattering with the optical phonon [67,76]:

$$\mathcal{J}_{OP}(\varepsilon) = \frac{\pi\mathbb{N}}{\hbar}\omega_0 g_0^2 [1 - f(\varepsilon - \omega_0)](\mathbb{N}(\omega_0) + 1)N(\varepsilon - \omega_0) \qquad (1.37)$$

with $\mathbb{N}(\omega_q)$ a Bose function, g_0 the electron-optical phonon coupling constant [88], $f(\varepsilon)$ the Fermi function and $N(\varepsilon)$ the electron density of states in graphene.

The comparison between electron-electron scattering energy relaxation rate $\mathcal{J}_{el}$ in **Eq. (1.35)** and electron-optical phonon scattering energy relaxation rate $\mathcal{J}_{OP}$ determine the ratio of energy transfer into the electronic system following the photoexcitation. It is estimated to be $\mathcal{J}_{el}/\mathcal{J}_{OP} > 1$ for graphene with typical doping level $|E_F| > 0.1$ eV [76], leading to over 50% excitation energy maintaining in thermalized hot carriers. Experimentally, $\mathcal{J}_{el}/\mathcal{J}_{OP}$ as high as 4 has been achieved and reported [12], confirming the efficient electronic heating effect in graphene.

The amount of energy by the electronic system absorbed from a photoexcited electron with energy $\varepsilon = E_{photon}/2$ after time t_0 is [67]

$$\Delta Q_{el} = \int_0^{t_0} \mathcal{J}_{el} dt = \int_{E_F}^{E_{photon}/2} \frac{1}{1 + \mathcal{J}_{OP}/\mathcal{J}_{el}} d\varepsilon. \qquad (1.38)$$

The electron temperature is a key indicator of hot carriers in photoexcited graphene. It is vital to have an estimation of the initial electron temperature T_e

of the hot-electron gas following optical excitations and heating processes. Ac-
cording to **Eq. (1.28)**, one can estimate the electronic temperature in graphene
by the electronic heat capacity following [89]. However, such methods simply
divide graphene into two phases ($|E_F| \approx 0$), metal-like and semiconductor-like
($|E_F| \gg 0$), and neglects the fact that the chemical potential does shift follow-
ing the heating process, depending on the electronic temperature. Here we take
into account the chemical potential by considering the two conservations: (I)
energy conservation and (II) particle number conservation.

We have the conservation of energy before and after the photoexcitation:

$$Q_{total}(T_e) = Q_0 + \Delta Q \tag{1.39}$$

where, ΔQ is the increased energy in the electronic system, of the incident en-
ergy Q_{in} times the absorption efficiency $\gamma = 2.3\%$ for idea graphene and heat
efficiency η_{heat}

$$\Delta Q = \gamma \eta_{heat} Q_{in}. \tag{1.40}$$

We take $\eta_{heat} = 50\%$ as reported in [12]. According to **Eq. (1.33)**, we can
write $Q_{total}(T_e)$, while the energy is conserved, as:

$$Q_{total}(T_e) = \int_0^\infty \varepsilon v(\varepsilon) f_e(\mu, T_e, \varepsilon) d\varepsilon + \int_0^\infty \varepsilon v(\varepsilon) f_h(\mu, T_e, \varepsilon) d\varepsilon$$
$$= Q_0 + \Delta Q \tag{1.41}$$

and Q_0 as:

$$Q_0 = \int_0^\infty \varepsilon v(\varepsilon) f_e(E_F, T_L, \varepsilon) d\varepsilon + \int_0^\infty \varepsilon v(\varepsilon) f_h(E_F, T_L, \varepsilon) d\varepsilon \tag{1.42}$$

where T_L is the lattice temperature before the photoexcitation, which is 300 K
at room temperature. We usually assume that the chemical potential at room
temperature is equal to the Fermi energy E_F.

Eq. (1.41) indicates the total amount of absorbed energy converted into electronic heat [90,91]. The energy absorbed by graphene electrons raises their electronic temperature T_e above the lattice temperature T_L.

Furthermore, along with energy conservation, the conservation of particle numbers needs to be considered, i.e., the total carrier density should stay constant at any electron temperature. We consider both densities of electrons and holes. According to **Eq. (1.32)**, we can easily write the total carrier density before and after the carrier heating, assuming the electron temperature before photoexcitation equals the lattice temperature T_L:

$$n = \int_0^\infty v(\varepsilon)[(f_e(\mu, T_e, \varepsilon) - f_h(\mu, T_e, \varepsilon)]d\varepsilon$$
$$= \int_0^\infty v(\varepsilon)[(f_e(E_F, T_L, \varepsilon) - f_h(E_F, T_L, \varepsilon)]d\varepsilon. \qquad (1.43)$$

This relation results in a shift of chemical potential when the electron temperature changes. Frenzel *et al.* [92] first applied this conservation relation to explaining THz photoconductivity in graphene.
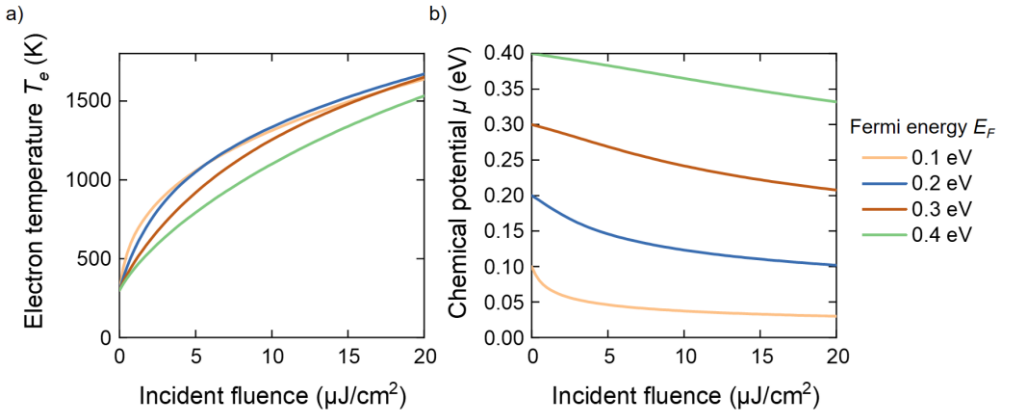
Figure 1.6 | Electron temperature (a) and chemical potential (b) after the carrier heating with a specific incident laser fluence. The results are obtained by numerically solving **Eq. (1.41)** and **(1.43)**.

To follow the energy conservation law and particle number conservation law, after the excitation by an incident laser pulse with the energy of Q_{in}, both electron temperature T_e and chemical potential μ changes. We can numerically calculate the electron temperature T_e and chemical potential μ by solving these two conservation laws with an incident energy Q_{in} in graphene with a specific Fermi energy E_F ranging from 0 eV to 0.3 eV, as shown in **Figure 1.6**.

1.2.3 Acoustic phonon collision cooling

After the electron-electron scattering cascade, a hot-electron gas with a defined electron temperature is established. This is followed by slower cooling processes mediated by phonon emissions, occurring on a picosecond timescale. For energetic hot electrons, cooling via optical phonons has been proposed before, as discussed in the last section. On the other hand, hot carriers with an
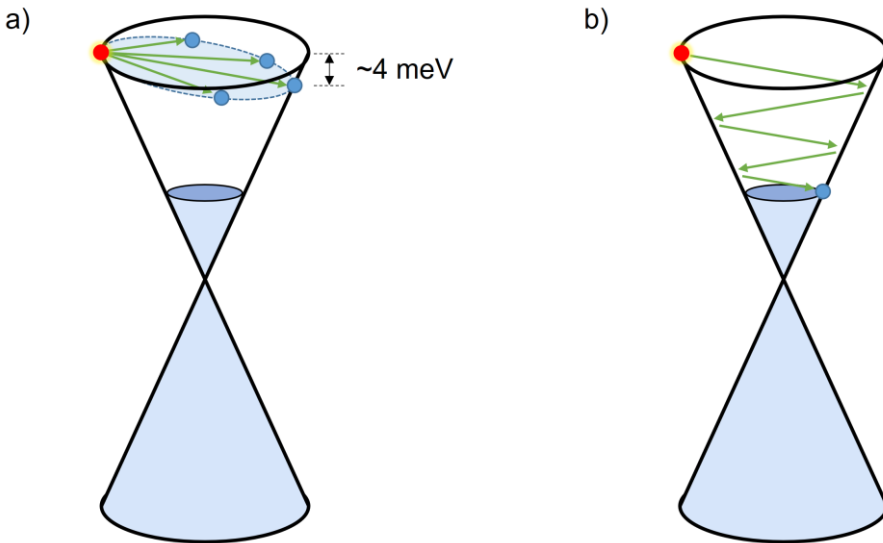
Figure 1.7 | Acoustic phonon collision cooling. (a) Schematic of electron scattering with acoustic phonons. The electrons relax and drop to a tilted circle which is slightly below the initial energy level. **(b)** Multiple acoustic phonon collisions are required for an electron at a high energy level to cool down fully.

energy lower than the optical phonon emission requirements ($\varepsilon < 0.2$ eV) were believed to cool down by the electron-acoustic phonons (AP) emission [16,75,81,85,86,93].

We evaluate the collision between electrons with acoustic phonons. The acoustic phonon (AP) in graphene has an approximately linear dispersion $\varepsilon^{AP} = v^{AP} k^{AP}$, with a velocity about 100 times smaller than the electron velocity $v^{AP} \ll v_F$ [81,85]. By solving the energy and momentum conservation relations below

$$\begin{aligned} \varepsilon^{initial} &= \varepsilon^{final} + \varepsilon^{AP} \\ \boldsymbol{k}^{initial} &= \boldsymbol{k}^{final} + \boldsymbol{k}^{AP}. \end{aligned} \tag{1.44}$$

One can see that the final state for the excited electron is a tilted circle that is slightly below the initial state, shown in **Figure 1.7a**. This limits the maximum transferred energy to about 4 meV at each collision event. Thus, more than 40 acoustic phonon emission events are required to cool a hot electron from its initial energy at 0.2 eV [81,94]. Such an inefficient process imposes a bottleneck during carrier cooling, resulting in a long cooling time, exceeding 300 ps [85,95].

Bistritzer and MacDonald [85] have calculated the cooling time required for acoustic phonon collision cooling. They proposed a differential equation to describe the electron temperature considering the electron-acoustic phonon scattering rate defined by Fermi's Golden Rule [85]

$$\frac{dT_e}{dt} = -\gamma T_e^2 (T_e - T_L) \tag{1.45}$$

where $\gamma = \frac{7\pi^4 D^2}{540 \xi(3) \rho_m v_F^4} = 1.18 \times 10^3 D^2$ $(\text{meV}^2 \text{s})^{-1}$ with screened deformation potential D measured in eV. We can then simulate the transient electron

temperature dynamics by plotting the rate equation (**Figure 1.8**), with $D = 19$ eV. The cooling process extends to hundreds of picoseconds.
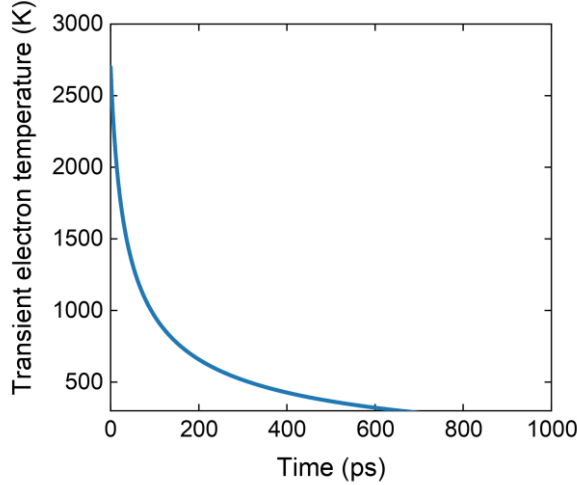
Figure 1.8 | Modelled cooling dynamics via normal acoustic phonon collisions based on Eq. (1.45). The initial electron temperature is 3000 K. The cooling takes hundreds of picoseconds.

1.2.4 Disorder-assisted "supercollision" cooling

While in the acoustic phonon emission, the momentum conservation and velocity mismatch between v^{AP} and v_F dramatically limits the cooling rate for hot electrons, the presence of disorder in graphene can provide additional momentum required for the electron-phonon emission. Disorder-assisted cooling, or so-called "supercollision", relax the momentum conservation condition and does not constrain the energy exchange per collision event [86]. A "supercollision" event consists of the emission of a phonon with a much larger momentum than the electron momentum, accompanied by the emission of a recoil phonon to conserve the total momentum, shown in **Figure 1.9**.

With the disorder presented in the collision events, the momentum conservation and energy conservation can be written as:

$$\varepsilon^{initial} = \varepsilon^{final} + \varepsilon^{AP}$$
$$\boldsymbol{k}^{initial} = \boldsymbol{k}^{final} + \boldsymbol{k}^{defect\cdot}$$

(1.46)

Following the "supercollision" model, the hot electron temperature relaxation rate can be described by a differential equation following [86]:

$$\frac{dT_e}{dt} = -\frac{A}{\alpha}\frac{(T_e^3 - T_L^3)}{T_e}.$$

(1.47)

The theoretical estimate of the parameter $\frac{A}{\alpha}$ has been given by [86] as

$$\frac{A}{\alpha} = \frac{6\xi(3)}{\pi^2}\frac{\lambda}{k_F l}\frac{k_B}{\hbar} \cong \frac{2}{3}\frac{\lambda}{k_F l}\frac{k_B}{\hbar}$$

(1.48)
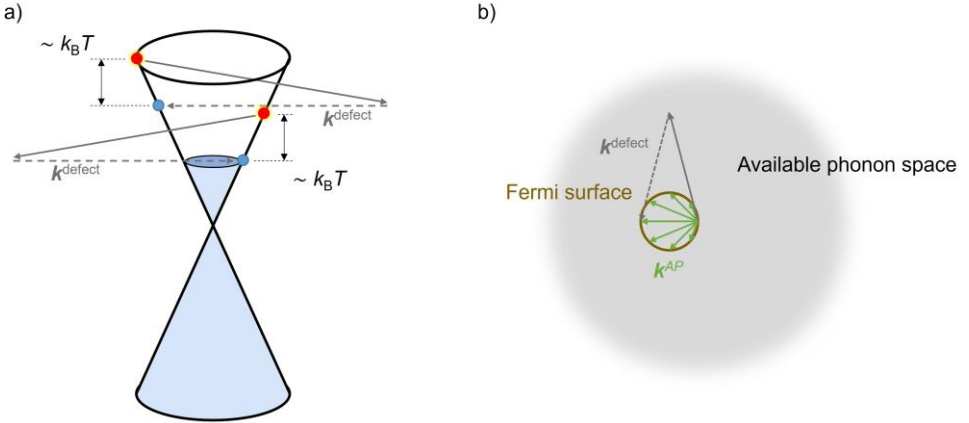
Figure 1.9 | Supercollision model for hot-carrier cooling (a) The disorder (defect) in graphene lattice relaxes momentum restriction of acoustic phonon emission. In a "supercollision" event, efficient cooling by the emission of high-energy ($\sim k_B T$) acoustic phonons is enabled. **(b)** Kinematics of "supercollision" compared to normal acoustic phonon collisions. The scattering via defects serves as recoil momentum.

where $\lambda = \frac{D^2}{\rho v_s^2}\frac{2E_F}{\pi(\hbar v_F)^2} \propto E_F$ is the electron-phonon coupling strength [86], with ρ being the mass density and v_s being the sound velocity. This has been used to explain experimental observations of ultrafast picoseconds cooling in graphene in [16]. We use the electrical mobility to get a lower bound for the

disorder scattering (short-range Coulomb impurities, e.g., small isolated de-
fects appearing within the lattice [96]), although there is actually a large con-
tribution from long-range Coulomb scattering. This type of scattering does not
contribute to disorder-assisted cooling, which means that one can obtain a
lower bound for the cooling time by assuming disorder-dominated electrical
mobility. As discussed in **Eq. (1.19)** and **(1.22)**, the mobility μ_m and Fermi
energy E_F of graphene determine the mean free path l. By varying the mobility
and Fermi energy, we can simulate the cooling dynamics and cooling time
$\tau_{cooling} = (3\frac{A}{\alpha}T_L)^{-1}$ (**Figure 1.10**).
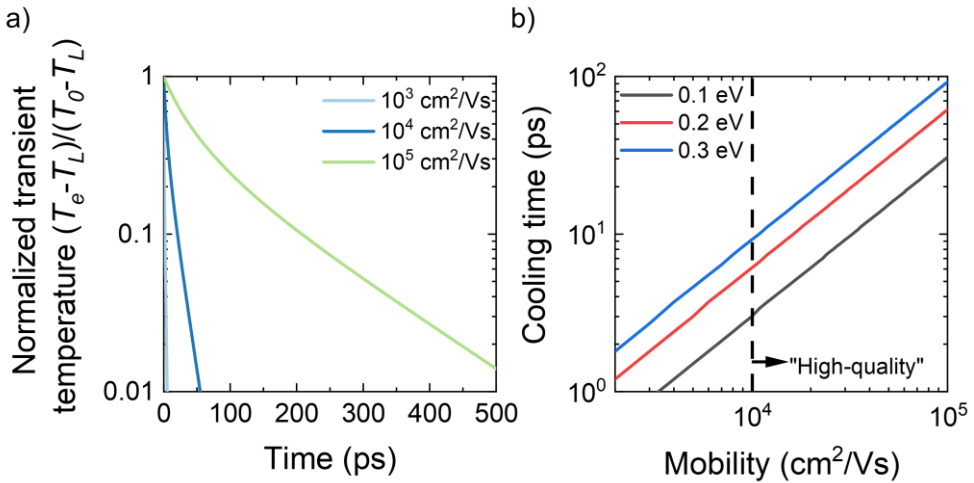
**Figure 1.10 | Calculated "supercollision" cooling time as a function of
charge carrier mobility.** **(a)** Normalized transient temperature dynamics of
"supercollision" cooling starting from an initial temperature T_0 of 3000 K,
when graphene has the Fermi energy 0.2 eV and three different orders of mo-
bility value. **(b)** Cooling time as a function of graphene mobility. We define
the "high-quality" graphene when its mobility is higher than 10^4 cm²/Vs,
where the "supercollision" cooling effect can be neglected because the disorder
density is low enough.

1.2.5 Other cooling mechanisms

Other external cooling pathways have been explored and revealed, e.g., through the phonon emissions in the supported substrates [97–99], and in the encapsulated graphene sandwiched by other two layers of 2D materials. Hyperbolic phonon-polaritons in hexagonal boron nitride (*h*-BN) flakes have recently been proposed and demonstrated as a new hot carrier cooling pathway [17,100].

Substrates play an essential role in dissipating energy from graphene. Graphene is often placed on polarizable substrates such as SiO_2 and SiC. The remote interfacial polar optical phonons on/near the SiO_2 surface should be considered as a cooling channel [98,99]. In addition, when graphene stays on a substrate, the substrate's surface roughness will give rise to ripples in graphene. Such ripples correlate to long-range fluctuations, which act as random uncorrelated impurities to scatter electrons [101,102]. Those ripple impurities eventually serve as disorders in the "supercollision" process [67].

Recent developments of van der Waals heterostructure fabrication [24] offer the possibility to use other 2D materials, for instance, *h*-BN as atomic-flat substrates for graphene [103]. Graphene-based 2D heterostructures led to numerous exciting optoelectronic applications, including photovoltaic devices [104] and photodetectors [7]. Despite the high mobility feature of graphene encapsulated by *h*-BN (often above $30,000 \text{ cm}^2\text{V}^{-1}\text{s}^{-1}$) which indicates the disorder density is so low that "supercollision" has been strongly suppressed, there is no notable slowdown of the cooling process. The reason is that in these heterostructures, another cooling channel exists: hot electrons in graphene can couple with hyperbolic phonon polaritons of the *h*-BN [17,100,105]. Hyperbolic phonon polaritons occur in spectral regions,

where the in- and out-of-plane permittivities ($\epsilon_\parallel$ and $\epsilon_\perp$, respectively) have opposite signs, i.e., the permittivity product $\epsilon_\parallel \cdot \epsilon_\perp$, is negative [105–107]. These hyperbolic spectral regions contain a high density of optical modes, which are accessible via near-field interaction with a large range of momentum vectors. Those make the hot carriers in *h*-BN encapsulated graphene cool down in a few picoseconds at room temperature [17,100,105].

In addition to hot-carrier cooling via phonons in graphene and nearby environments, plasmon emission has been proposed as another competing decay pathway in several theoretical studies [108,109]. Unlike the thermalization via carrier-carrier scattering, which brings both electrons and holes onto higher energy states (e.g., as hot carriers), the plasmon emission directly drives electrons and holes from high energy to low energy states. Moreover, hot-carrier emitted plasmons interact with phonons, eventually dissipating energy [108]. The carrier recombination of photoexcited carriers due to plasmon emission is calculated to happen in tens of femtoseconds timescale [109] after photoexcitation. Optically generated non-equilibrium plasmons were studied experimentally as relaxation pathways for hot carriers in 100s fs timescale [110].

2 Terahertz spectroscopy

Figure 2.1 | The electromagnetic spectrum. Photons in THz radiations have wavelengths on the order of 10^{-3} m, frequencies of $\sim 10^{12}$ s^{-1}, and oscillation periods of $\sim 10^{-12}$ s. Those periods correspond to the typical timescales involved in electronic transport (for example, Drude scattering times).

The THz radiation, also known as submillimeter radiation, consists of electromagnetic frequencies ranging from 0.1 THz (equivalent to 100 GHz) to 10 THz. The THz radiation covers an energy range between about 0.4 to 41 meV. These frequencies are between the infrared and microwave frequencies shown in the electromagnetic spectrum in **Figure 2.1**. Spectroscopy work-

ing in the THz frequency range can be powerful because THz radiation is sensitive to the responses of motion of charge carriers, for example, free carriers (electrons and holes), polarons (bound states of electrons and ions), and excitons (bound electron-hole pair). Moreover, the charge carrier responses are on the 100 fs to 10 ps time scale, which corresponds to THz frequencies, i.e., $0.1 - 10$ THz.

There were technical limitations for THz generation and detection in history due to the lack of THz emitters and detectors, leading to a known electromagnetic gap, the so-called "THz gap" [111]. 1 THz corresponds to a wavelength of 300 μm. A photon with a frequency of 1 THz has an energy of 4.2 meV, far below the room-temperature thermal energy ($k_B T \approx 26$ meV). Therefore, THz frenquencies typically do not have enough energy required for the electronic transitions for optical emitters and detectors. Besides, generation and detection solutions for megahertz and gigahertz waves also do not work in THz frequencies. In the late 1980s, it became possible to generate and detect free propagating THz pulses, when the application of photoconductive antennas [112,113] and later optical rectification techniques [114] were developed. In this chapter, we focus on discussing the THz generation process by optical rectification.

2.1 Nonlinear optical processes

Interaction between electromagnetic radiation and polarization of material is nonlinear when the incident electric field strength (usually in a laser pulse) is strong enough. For linear optics, one can write the polarization as

$$P(t) = \epsilon_0 \chi^{(1)} E(t). \tag{2.1}$$

The $\chi^{(1)}$ represents the linear susceptibility and ϵ_0 is the vacuum permittivity. One can consider the polarization as the dipole moment per unit volume.

In nonlinear optics, one describes the optical response by generalizing $P(t)$ as a power series of the field strength $E(t)$, as

$$P(t) = \epsilon_0\left[\chi^{(1)}E(t) + \chi^{(2)}E^2(t) + \chi^{(3)}E^3(t) + \cdots\right]$$
$$= P^{(1)}(t) + P^{(2)}(t) + P^{(3)}(t) + \cdots. \tag{2.2}$$

$\chi^{(2)}$ is the second-order nonlinear susceptibility, which describes second-order effects, e.g., second-harmonic generation (SHG). Similarly, $\chi^{(3)}$ is the third-order nonlinear susceptibility and describes third-order effects e.g., third-harmonic generation, four-wave mixing, and the intensity dependence of the index of refraction (e.g., Kerr effect). When the amplitude of the applied field E is comparable to the characteristic atomic electric field strength $E_{at} = e/(4\pi\epsilon_0 a_0^2)$, the lowest-order correction term $P^{(2)}$ is expected to be comparable to the linear response $P^{(1)}(t)$. e is the elementary charge and a_0 is the Bohr radius. According to [115], one can find that $E_{at} = 5.14 \times 10^{11}$ V/m. This leads to the second-, third-order susceptibility $\chi^{(2)}$ and $\chi^{(3)}$ on the order of 10^{-12} m/V and 10^{-12} m^2/V^2, respectively.

We now discuss that $\chi^{(2)}$ vanishes for a material possessing a center of inversion symmetry (i.e., a centrosymmetric medium), **Figure 2.2a**. For centrosymmetric medium, one writes

$$P(E) = \epsilon_0\left[\chi^{(1)}E + \chi^{(2)}E^2 + \chi^{(3)}E^3 + \chi^{(4)}E^4 \ldots\right]. \tag{2.3}$$

Then one applies inversion symmetry operation

$$P(-E) = \epsilon_0\left[-\chi^{(1)}E + \chi^{(2)}E^2 - \chi^{(3)}E^3 + \chi^{(4)}E^4 \ldots\right]. \tag{2.4}$$

On the other hand,

$$P(-E) = -P(E) = \epsilon_0\left[-\chi^{(1)}E - \chi^{(2)}E^2 - \chi^{(3)}E^3 - \chi^{(4)}E^4 \ldots\right]. \tag{2.5}$$

We can see that including $\chi^{(2)}$, all $\chi^{(even)}$ should equal to zero.

On the other hand, for non-centrosymmetric media, see **Figure 2.2b**, $\chi^{(odd)}$ alone can not describe the rectified polarization, and $\chi^{(even)}$ need to be included, thus $\chi^{(even)} \neq 0$. As a result, the solution of polarization with an applied oscillating electric field (light) in a non-centrosymmetric media is rectified oscillation.

a)　　　　　　　　　　　　　　　　b)
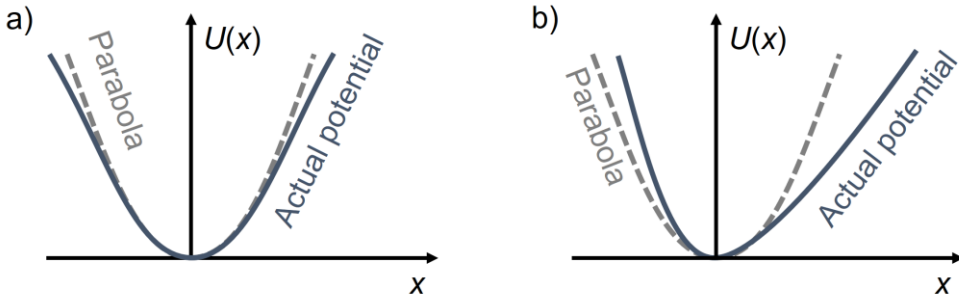
Figure 2.2 | Potential functions of a centrosymmetric medium and a non-centrosymmetric medium. **(a)** A medium possesses a center of inversion symmetry, which can be seen as symmetric under the operation $x \to -x$. **(b)** The potential well that the electron in material experiences is not symmetric in a non-centrosymmetric medium.

For a given laser beam with an electric field

$$\bar{E}(t) = E_0 e^{-i\omega t} + \text{c.c.} = 2E_0 \cos(\omega t) \tag{2.6}$$

where ω is the angular frequency. One has

$$\bar{P}^2(t) = \epsilon_0 \chi^{(2)} \bar{E}^2(t) = 2\epsilon_0 \chi^{(2)} E_0^2 \cos(2\omega t) + 2\epsilon_0 \chi^{(2)} E_0^2 \tag{2.7}$$

where the first term shows the second harmonic generation and the second shows the optical rectification (OR). As clearly shown, OR is not frequency-dependent quantity (i.e., it is a DC contribution), and it scales lineally with $\chi^{(2)}$.

2.2 THz generation and detection

In this section, we present an overview of the THz generation by employing optical rectification. We refer to the generation methods demonstrated

by [116,117]. As shown in **Eq. 2.7**, efficient optical rectification requires a large $\chi^{(2)}$ coefficient and thus nonlinear optical crystals without central inversion symmetry. Standard choices of nonlinear crystals for optical rectification using a Ti:sapphire laser are zinc telluride (ZnTe), gallium selenide (GaSe), and gallium phosphide (GaP) [118]. We use the ZnTe crystals in our experiments, which can emit frequencies covering the $0-3$ THz range.

As discussed earlier in a nonlinear optical process, non-centrosymmetric media gives rise to $\chi^{(even)}$, including the second-order term $P_2 = \chi^{(2)}E^2$. Here one omits the dielectric constant of vacuum ϵ_0 for simplification. It is crucial for the THz generation that the ultrafast laser pulses have the matching frequency bandwidth $\Delta\omega$ in the THz frequency, which is the condition for the difference-frequency generation that produces THz-radiation. The laser pulse duration Δt is very short (~ 100 fs), corresponding to a bandwidth of ~ 10 THz in the Fourier frequency domain estimated by $1/\Delta t$ neglecting a prefactor due to the Gaussian temporal profile of the pulsed laser. The laser pulse can be seen as a Gaussian function of time variance σ_t^2 and mean frequency ω_0:

$$E(\omega) = \exp\left(-\frac{(\omega-\omega_0)^2}{2\sigma_t^2}\right). \qquad (2.8)$$

In a short laser pulse, multiple frequencies are present. In the time domain, we describe the electric field as an oscillating harmonic field. For any given two frequencies with in the bandwidth of the laser pulse, one can assume $E_1(t) = E_0 \cos(\omega_1 t)$ and $E_2(t) = E_0 \cos(\omega_2 t)$. When these two harmonic waves reach a THz-generation crystal at the same moment, one can write the second-order term P^2 as:

$$P^2 = \chi^{(2)}E_1(t)E_2(t) = \chi^{(2)}E_0^2 \cos(\omega_1 t)\cos(\omega_2 t)$$

$$= \chi^{(2)} \frac{E_0^2}{2} [\cos(\omega_1 - \omega_2)\, t + \cos(\omega_1 + \omega_2)\, t].\qquad(2.9)$$

The ZnTe crystal facilitates the generation of a new electromagnetic wave with a different frequency $\omega_1 - \omega_2$ in the terahertz regime. Radiation with sum frequency $\omega_1 + \omega_2$ is produced but does not meet the phase match condition. The THz intensity scales with the incoming electric field strength and with the $\chi^{(2)}$ coefficient (see optical rectification term in **Eq. 2.7**).

a)
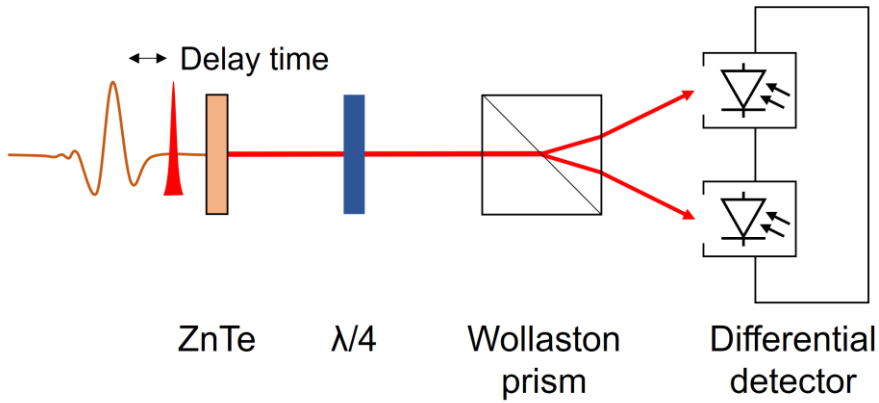
b)
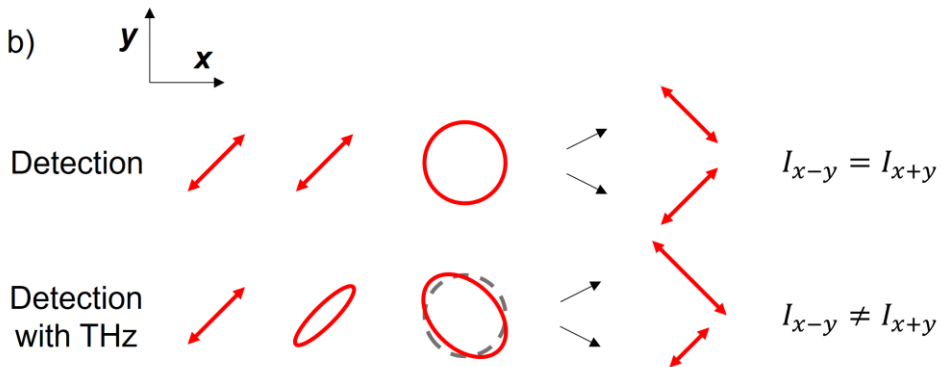
Figure 2.3 | Balanced detection of THz. (a) the elements required for balanced diode detection of THz signal. **(b)** Polarizations are different in front of and behind each polarization optics depending on whether there is a THz field reaching ZnTe crystal.

The THz detection relies on the polarization change of the detection beam in the ZnTe crystal. Next, we explain it based on the concept of polarization, referring to [119,120]. Light (electromagnetic waves) is the synchronized oscillations of the electric field $\vec{E}$ and $\vec{B}$ in space, where they are perpendicular to each other and to the direction of propagation of the wave. One can take the $\vec{z}$ direction as the propagation direction of the light. The electric field $\vec{E}$ can be decomposed to two electric fields orthogonal to each other: one oscillating in the $\vec{x}$ direction and the other in the $\vec{y}$ direction. The electric field $\vec{E}$ can then be expressed by the following formula, with the frequency ω, the wavevector k, and the amplitude $\vec{A}$ [121,122],

$$\vec{E}(z,t) = A_x e^{i(kz-\omega t)}\vec{x} + A_y e^{i(kz-\omega t+\varphi)}\vec{y} \qquad (2.10)$$

where φ is the phase difference between $\vec{E}_x$ and $\vec{E}_y$. When $\varphi = 0$, the wave is linearly polarized. When $\varphi \neq 0$, the $\vec{E}_x$ and $\vec{E}_y$ are out of phase. If there is a phase difference of $\frac{\pi}{2}$, the light is circularly polarized if $A_x = A_y$. The direction of the sum for the two electric fields $\vec{E}$ is rotating in a circle. For other phase differences, $\vec{E}$ is rotating in an ellipse.

Detection of THz field relies on electro-optical sampling effect in optical nonlinear crystals (e.g., ZnTe) [116,123]. In the detecting process, the incident THz field introduces a birefringence. THz radiation absorption in the crystal changes the refractive index n for both two polarization directions, with however different amplitude: that is $\Delta n = \Delta n_e - \Delta n_o \neq 0$. Here, Δn_e represents the refective index change for light propagating perpendicular to the optic axis and Δn_o for light propagating parallel to the optic axis. Hereby n_0 is a constant

and δn_x is the change of refractive index, which is induced by the THz electric field $\vec{E}$

$$n_x = n_0 + \delta n_x(\vec{E})$$
$$n_y = n_0$$
(2.11)

The incoming beam for detection is written as $\vec{E}(z,t) = A_x e^{i(kz-\omega t)}\vec{x} + A_y e^{i(kz-\omega t+\varphi)}\vec{y}$ with a zero phase difference $\varphi = 0$. One can set $z = 0$ at the incident surface of the crystal. Then the incident detection beam is:

$$\vec{E}_{det,in} = \left(A_x\vec{x} + A_y\vec{y}\right)e^{-i\omega t}.$$
(2.12)

The wavevector in the $\vec{z}$ direction is k_0. In the crystal with a thickness of d, the different refractive index will cause a delay in the $\vec{x}$ and $\vec{y}$ polarized light. One can then write the outcoming wave as:

$$\vec{E}_{det,out} = \left(A_x e^{ik_0(n_0+\delta n_x)d}\vec{x} + A_y e^{ik_0n_0d}\vec{y}\right)e^{-i\omega t}$$
$$= \left(A_x e^{ik_0\delta n_x d}\vec{x} + A_y\vec{y}\right)e^{i(k_0n_0d-\omega t)}.$$
(2.13)

As we can see, the $\vec{E}_x$ and $\vec{E}_y$ have a phase difference with the factor $k_0\delta n_x d$ caused by the THz field. Hence, the outcome detection beam becomes elliptically polarized.

The detection beam then goes through a quarter-waveplate ($\lambda/4$) after the detection crystal. This waveplate converts the linear polarized optical detection beam into a circularly polarized beam when there is no birefringence effect in the detection crystal. When the crystal elliptically polarizes the detection beam with the THz incidence, the waveplate will convert the detection beam to elliptically polarized. In **Figure 2.3b**, we present an overview of the change in polarization directions for the detection line. After the quarter-waveplate, a Wollaston prism splits the polarization components of sampling pulses into two beams (I_{x-y} and I_{x+y}). When there is no incident THz field, the sampling

beam after the quarter-waveplate is perfectly circularly polarized. So, the intensity (field strength) of the two components is equal, i.e., $I_{x-y} = I_{x+y}$. When there is a THz field reaching the ZnTe crystal, the light after the quarter-wave plate will be elliptical. The intensity of the two components after the Willaston prism is different, $I_{x-y} \neq I_{x+y}$. The intensity difference $\Delta I = I_{x-y} - I_{x+y}$ is proportional to the incident THz electrical field. Balanced diodes measure the difference between the two beams after the Wollaston prism. This method reduces the overall noise by correcting the temporal intensity fluctuations of the laser beams.
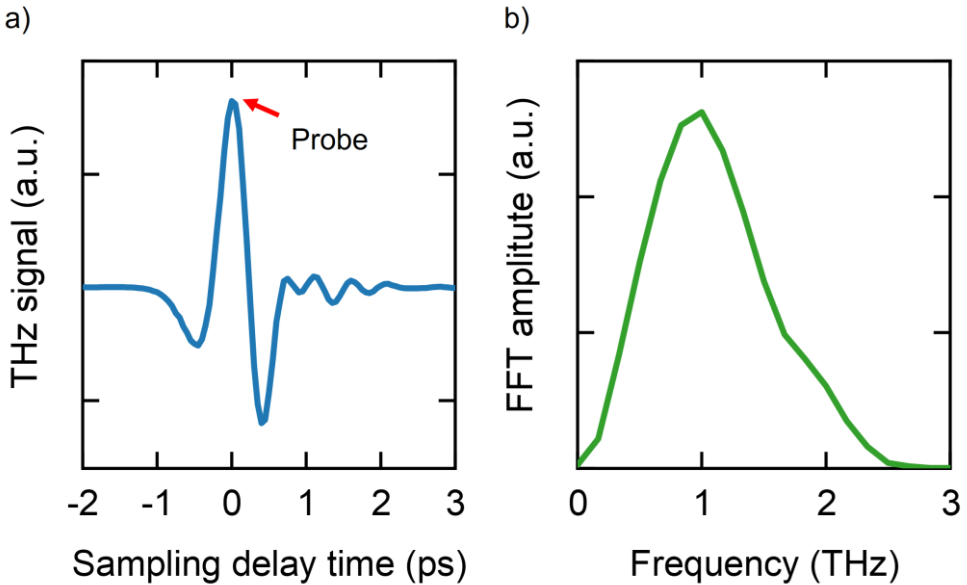
Figure 2.4 | THz signal generated and measured by ZnTe nonlinear crystal. (a) The THz signal in the time domain. The waveform is measured for 5 ps with a step size of 0.05 ps. **(b)** The frequency-resolved THz signal by performing a numerical fast Fourier transform (FFT) transformation of the signal presented in (a). The frequency range is between 0 and 3 THz.

The detection pulse is sub-100 fs, being much shorter than the THz pulse with a typical duration of a few picoseconds. By adjusting the time delays between the THz and detection beams, one can sample out the entire waveform of the THz field in the time domain. We can achieve it by placing an optical delay stage in one of the beams' optical paths. The delay stage moves with a 1 µm resolution, which corresponds to a time delay of 3.3 fs. Note that the time resolution of the THz spectroscopy is limited by the cross-correlation dispersion and velocity mismatch happening in the ZnTe crystal. The THz spectroscopy described in this thesis has a time resolution of about $200 - 300$ fs.

We place the first optical chopper in the path of the THz generation beam. The chopper chops one of every two neighboring pulses. Since the detection and generation pulses have the same repetition rate 1000 Hz, half of the detection pulses detect the signal without a THz reaching the ZnTe crystal as a reference. Another half of the detection pulses detect the signal with the THz field reaching the ZnTe crystal. By deducting the reference signal, one can calculate the difference of signal between the two sequential pulses, which gives the signal of the THz electric field $\vec{E}$, shown in **Figure 2.4**.

Furthermore, we do our measurements in a nitrogen-purging environment. The water vapor existing in the air absorbs specific frequencies in the THz range and gives wiggles in the measured signal. All those settings compose a terahertz time-domain spectroscopy (THz-TDS).

2.3 Optical pump-THz probe (OPTP) spectroscopy

In addition to the THz generation and detection beams, we have a third beam from the same pulsed laser source – pump beam. By combining this op-

tical pump with the THz-TDS, we can use THz to detect photogenerated carriers' photoconductivity following optical excitations. This is termed optical pump-THz probe spectroscopy, in short, OPTP spectroscopy, shown in **Figure 2.5**.
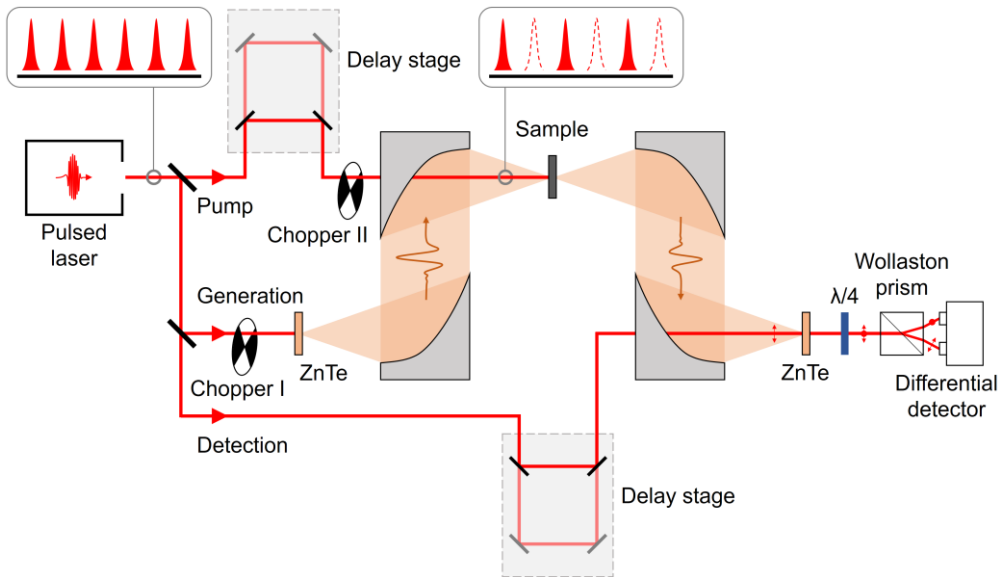
Figure 2.5 | Sketch of an optical pump-THz probe experimental setup. Ultrafast laser pulses enter the setup from the upper left corner. Two beam splitters then split the laser into three: the pump beam, which photoexcites the sample, and two other beams for the THz pulse generation and detection. Two mechanical choppers (I and II) block half of the beam frequency in either the pump or THz generation beam, depending on which experiment runs. THz pulses transmit through the sample and eventually meet the detection beam at a second ZnTe crystal. The differential detector then measures the THz field-induced polarization change of the detection pulse in a balanced detection scheme (including a $\lambda/4$ waveplate, a Wollaston prism, and a differential detector). Two optical delay lines control the relative delay times between the three pulses. See **Figure 2.6** for a more detailed illustration of how the three beams travel in time.

We first place the THz generation and detection beams with a fixed time delay at the maximum of the THz field. Next, we add a second delay stage in the path of the pump beam, which can control the time difference between the
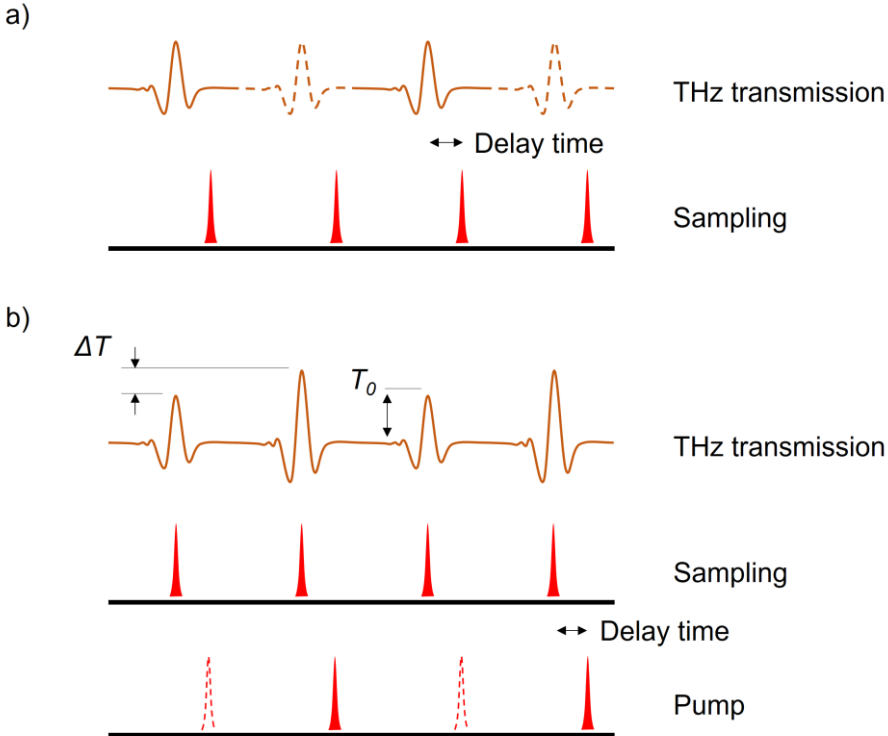
Figure 2.6 | Temporal scheme of the pump-probe laser pulses. (a) By controlling the delay time between sampling (detection) and THz pulses (generated by the generation beam), the THz-TDS monitors THz's waveform in the time domain. The signal is the differentials between nearby two sampling pulses. Only the first pulse meets a THz pulse in the time domain. **(b)** The OPTP measurements monitor the different THz transmission through the sample, with and without a pump excitation. One measures the change of THz transmission in the time domain by tuning the delay time between THz sampling and pump pulses. In contrast, the time difference between THz detection and sampling is fixed.

pump beam and THz pulse reaching the sample. Then, we place a second chopper in the pump beam path, which chops half the pump pulses. We remove the chopper in the THz generation beam during the OPTP measurements, which results in no difference between signals from the two neighboring detection beams. After we introduce the third pump beam, at half of the repetition rate of 500 Hz, the nearby two detection beams will probe the difference between the THz transmission signal through the sample with and without a pump pulse excitation, illustrated in **Figure 2.6b**. The signal from the balanced diodes gives ΔT – the change of the THz transmission through the photoexcited sample. We usually normalize it by the THz transmission through the sample without the excitation and get $\frac{\Delta T}{T_0}$.

We set the detection at the THz field's peak position and run measurements while moving the optical pump delay stage. Probing the time-dependent transmission change at the THz peak following optical excitation provides information on the charge carriers' dynamics in a material.

2.4 Graphene conductivity measured by THz spectroscopy

The principle of using THz radiation to measure the conductivity of a material is that the photoexcited charge carriers change the complex reflective index $\tilde{n}$ of the material. The complex reflective index has a relationship with the complex wavevector $\widetilde{\mathbb{k}}$ given by $\tilde{n} = \frac{c\widetilde{\mathbb{k}}}{\omega}$, where c is the speed of light and ω is the frequency. Therefore, one can write $\tilde{n}$:

$$\tilde{n} = n_1 + in_2 = \frac{c\mathbb{k}_1}{\omega} + i\frac{c\mathbb{k}_2}{\omega} \qquad (2.14)$$

with complex wave vector $\widetilde{\mathbb{k}} = \mathbb{k}_1 + i\mathbb{k}_2$. So if the refractive index of the sample is changed, this will also change the wavevector $\widetilde{\mathbb{k}}$ of the passing THz wave. The THz waveform can be written as:

$$\boldsymbol{E}_{THz}(z,t) = \boldsymbol{E}_0 e^{i(\widetilde{\mathbb{k}}z - \omega t)} = \boldsymbol{E}_0 e^{-\kappa z} e^{i(\mathbb{k}_1 z - \omega t)}. \qquad (2.15)$$

Thus, the real part of the index of refraction n_1, which is linked to $\mathbb{k}_1$, will cause a phase difference in the THz waveform. The imaginary part of the index of refraction n_2, which is linked to $\mathbb{k}_2$, will cause attenuation or absorption.

As already mentioned, in THz measurements, we effectively measure the conductivity σ. This is because the index of refraction and the conductivity are linked together. First of all, the complex index of refraction $\tilde{n}$ can be expressed in terms of the complex permittivity $\tilde{\epsilon}$ in the following way [124]. Here the $\tilde{\epsilon}_r$ stands for the complex relative permittivity, refer to $\epsilon = \epsilon_r \epsilon_0 = (1 + \chi_e)\epsilon_0$, where χ_e is the electric susceptibility. The two sets of optical constants are interchangeable ($\tilde{n} = n_1 + in_2$ and $\tilde{\epsilon} = \epsilon_1 + i\epsilon_2$), following:

$$\begin{aligned} \epsilon_0 \tilde{n}^2 &= \tilde{\epsilon} \\ \text{or} \quad \epsilon_0(n_1 + in_2)^2 &= \epsilon_1 + i\epsilon_2 \end{aligned} \qquad (2.16)$$

Next, the electric current density $\boldsymbol{J}$ as a vector, the optical conductivity σ as a scalar and the electric field vector $\boldsymbol{E}$ have the relation:

$$\boldsymbol{J}(\omega) = \sigma(\omega)\boldsymbol{E}(\omega) \qquad (2.17)$$

while the relation between the electrical displacement field $\boldsymbol{D}$, permittivity and the electric field:

$$\boldsymbol{D}(\omega) = \epsilon(\omega)\boldsymbol{E}(\omega). \qquad (2.18)$$

The connection between the above two response functions gives:

$$\sigma(\omega) = i\omega[\epsilon_0 - \epsilon(\omega)]. \qquad (2.19)$$

Therefore, the real part of the complex permittivity is related to the imaginary part of the optical conductivity and vice versa. Now let us investigate the relationship between the THz signal $\frac{\Delta T}{T_0}$ and photoconductivity. For this, we have to approximate the index of refraction as a sum of the initial sample n_{eff} and a perturbation Δn contribution due to excitation:

$$n = n_{\text{eff}} + \Delta n \qquad (2.20)$$

where $n_{\text{eff}} \gg \Delta n$. It is shown that [125]:

$$\Delta \sigma \cong -\frac{\Delta T}{T_0}\frac{2c\epsilon_0 n_{\text{eff}}}{d} \qquad (2.21)$$

where d is the sample thickness. We note that in real measurements where we study thin-film materials on a substrate with a refractive index of n_s, for example, graphene on SiO₂, the photoconductivity is proportional to the signal by $\Delta \sigma = -\frac{\Delta T}{T_0}\frac{n_s+1}{Z_0}$ [12]. Here Z_0 is the free space impedance.

There are currently three approaches to build up the theoretical understanding of graphene photoconductivity in OPTP measurements, done by (1) Tielrooij *et al.* [12], (2) Frenzel *et al.* [92], and (3) Tomadin *et al.* [80], respectively. Each of those three approaches involves some approximations. Approach (1) considers screening and mobility dominated by long-range Coulomb scattering. However, this works only for graphene at high doping and weak carrier heating (caused by low photoexcitation intensity). Approach (2) assumes phonon-dominated scattering (rather than long-range Coulomb) and equal temperatures for lattice and electron systems. Approach (3) is an entire microscopic approach. This approach does a proper description of the scattering time based on long-range Coulomb scattering and dynamical screening. It explains properly the positive-to-negative photoconductivity transition trend

observed in graphene with different doping levels, which we discuss later, without the need to considering phonon scattering.

Here we use the third approach to interpret graphene photoconductivity in OPTP measurements. One first solves a semiclassical Boltzmann equation, which considers carrier-carrier and carrier-optical phonon scattering in graphene. Those methods are described with detailed mathematics in [13,126]. For graphene at a given Fermi level, the Fermi-Dirac distribution has finite carrier density in the conduction band ($E_F > 0$). The values of electron temperature and the chemical potentials are obtained by the best fit of the electron distribution, as shown in **Figure 1.6**. Then one can use the semiclassical Boltzmann equation linearized around the quasi-equilibrium distribution, which considers the scattering between carriers and long-range Coulomb impurities, to calculate the photoconductivity. This approach indicates that by measuring the photoconductivity ($\Delta\sigma$) of graphene via tracking the pump-induced THz transmission change $\frac{\Delta T}{T_0}$, one can monitor the electron temperature dynamics as a function of the pump-probe delay time.

2.5 OPTP response of graphene at different Fermi energies

Along with charge carrier cooling dynamics, another fascinating effect for photoresponse in graphene is related to its Fermi level-dependent photoconductivity: the photoconductivity is reported to be positive ($-\frac{\Delta T}{T_0} > 0$) for intrinsic graphene (with $|E_F| \approx 0$), and negative ($-\frac{\Delta T}{T_0} < 0$) for graphene with high charge carrier density (with $|E_F| \gg 0$) [80,89,92]. Such transition from a semiconductor-like (the photoexcitation increases carrier density, which in-

creases the conductivity) to a metal-like (the photoexcitation decreases the carrier mobility, which decreases the conductivity) behavior depending on the doping level is specific to zero bandgap materials like graphene. In the following, we will review the critical processes and parameters leading to this fascinating optoelectronic effect.
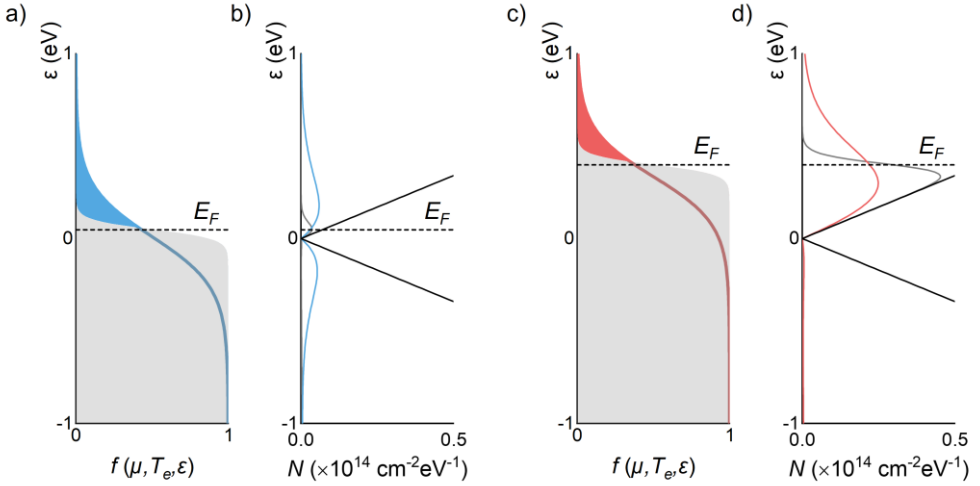
Figure 2.7 | Hot-carrier distribution in low ($E_F = 0.05$ eV) **and high doped** ($E_F = 0.4$ eV) **graphene.** **(a)** and **(c)** illustarte the calculated Fermi distribution $f_e(\mu, T_e, \varepsilon)$ before the photoexcitation ($T_e = T_L = 300$ K, room temperature, shown as the grey area) and after a carrier heating process after absorbing light (800 nm) with a fluence of 20 µJ/cm² (light blue and red lines and areas). The T_e after the photoexcitation reaches 1598 K for low doped graphene and 1496 K for high doped graphene. **(b)** and **(d)** show the corresponded occupancy of the states of electrons in the conduction band (above 0 eV) and holes in the valence band (below 0 eV). The black curves show the DOS near the Dirac point.

Here we study and compare the carrier distribution before and after photoexcitation in graphene for two cases: one with low ($E_F = 0.05$ eV) and the other with high electron density ($E_F = 0.4$ eV). In **Subsection 1.2.2**, we calculate the electron temperature and chemical potential following thermalization

(**Figure 1.6**), considering both energy and particle number conservations. Then we plot the carrier distribution at certain electron temperatures with related chemical potentials, shown in **Figure 2.7**. Before photoexcitation, the charge carrier distribution is slightly broadened due to thermal broadening. The thermalization following optical excitation further broadens the distribution. However, the broadened distributions are qualitatively different depending on the Fermi energy, owing to different relaxation processes that dominate the dynamics. At $E_F = 0.05$ eV, the heated carrier distribution contains a significant electron density (see the light blue area in **Figure 2.7a**) in the conduction band and hole density in the valence band (see the light blue curve in **Figure 2.7b**). This indicates the heating involves interband transitions. On the contrary, for highly electron-doped graphene ($E_F = 0.4$ eV), the carrier heating does not generate holes in the valence band; instead, it leads to an increase in hot-electron density (see **Figure 2.7c-d**). In other words, photoexcitation of highly doped graphene involves an interband heating process.

The conductivity change of graphene after photoexcitation can be expressed by $\Delta\sigma = (e(n_{after} + n_{before})\mu_{m,after} - en_{after}\mu_{m,before}) \propto e\Delta(n\mu_m)$, where e is the elementary charge, n_{after} and n_{before} are the carrier density after and before photoexcitation, $\mu_{m,after}$ and $\mu_{m,before}$ are the carrier mobility after and before photoexcitation, respectively, Δn is the change of carrier density in graphene and $\Delta\mu_m$ is the change of the carrier mobility in graphene. In low-doped graphene ($E_F \lesssim 0.1$ eV), the interband heating process after photoexcitation generates additional electrons and holes, which increase the number of free carriers. This increase of carrier density dominates the change in $n\mu_m$ following optical excitation, thus leading to a positive OPTP signal ($-\frac{\Delta T}{T_0} \propto$

$\Delta\sigma > 0$). By contrast, in highly doped graphene ($E_F \gtrsim 0.1$ eV), while charge carriers are redistributed following optical excitation, the total number of charge carriers do not substantially enhance (i.e., n_{after} is on the order of n_{before}). Microscopic simulations indicate that hot carriers are subject to a reduced screening of the impurities, leading to a reduction in the momentum scattering time [80], in comparison to cold carriers. Consequently, the hot carriers in highly-doped graphene possess lower mobility than the equilibrium ones: i.e., $\Delta\mu_m < 0$. Such change in charge scattering and thus mobility dominants the ultrafast photoconductivity, leading to a transient reduction in charge carrier conductivity, i.e., negative photoconductivity in graphene ($-\frac{\Delta T}{T_0} \propto \Delta\sigma \propto \Delta\mu_m < 0$): With increasing E_F, the hot-carrier density increases correspondingly, leading to an enhanced "negative" photoconductivity of graphene.

Several studies have reported this Fermi level-dependent photoconductivity in graphene, unveiling the peculiar transition from positive to negative photoconductivity while increasing the charge carrier density in graphene [82,89,92]. Here we illustrate and confirm such effect by measuring the THz photoconductivity of a graphene sample gated by ionic gating techniques. We deposit four-terminal geometry metal contacts on chemical vapor deposition (CVD) grown graphene on fused silica, enabling us to measure graphene resistance (shown in **Figure 2.8a**) electrically.
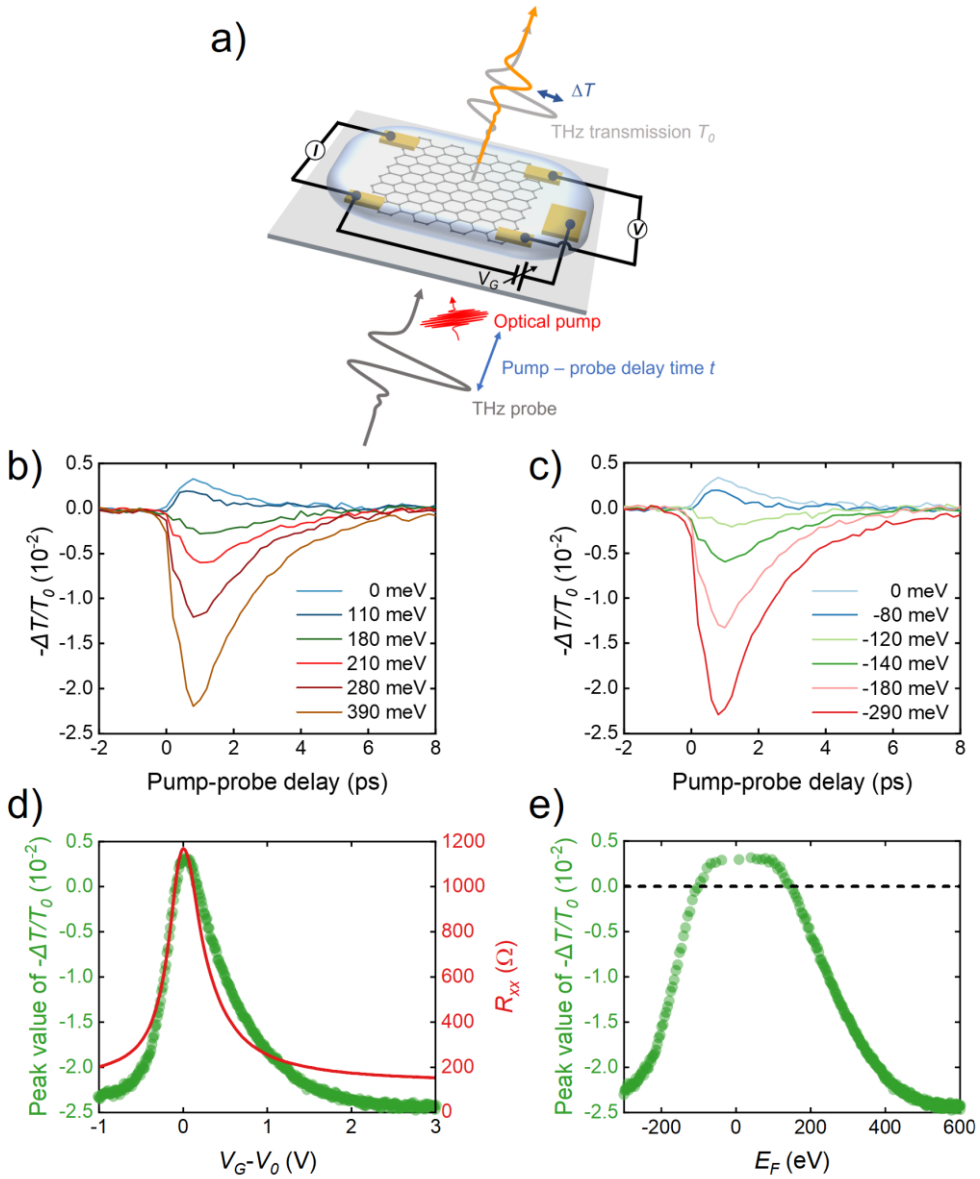
Figure 2.8 | OPTP dynamics of graphene controlled by ionic gating. (a) Schematic illustration of the measurement geometry. **(b)-(c)** OPTP dynamics $(-\Delta T/T_0)$ of graphene at different Fermi energies. **(d)** The gate voltage $(V_G - V_0)$-dependent peak value of $-\Delta T/T_0$, corresponding to the electrical resistance of graphene (red curve). **(e)** The Fermi energy-dependent peak value of $-\Delta T/T_0$.

Then we apply a gate voltage V_G via a gate electrode through a polyethylene glycol (PEO)-based LiClO$_4$ electrolyte to one of the four metal contacts. Such ionic gating techniques have been widely used to provide a large shift in chemical potential in graphene [89] and other thin layer materials such as 1T-TaS$_2$ [127]. We run OPTP measurements with the pump excitation wavelength of 800 nm and THz probe of ~1 THz while sweeping the gate voltage from -1 V to 3 V, *in situ* with electrically measuring graphene's resistance. We use the equation $|E_F| = \left(346\sqrt{V_G - V_0}\right)[\text{meV}]$ [89], where V_0 is the gate voltage when graphene reaches the charge neutrality point (highest electrical resistance), to determine the Fermi energy while changing the gate voltage. The time-resolved OPTP dynamics shown in **Figure 2.8b-c** clearly show the transitions from positive conductivity signal from graphene at low Fermi energy to negative conductivity at high Fermi energy (for both *n-* and *p-* doping regimes). We plot the peak values of $-\Delta T/T_0$ (highest value when the signal is positive and lowest value when the signal is negative) as a function of $V_G - V_0$ shown in **Figure 2.8d**. This Fermi level dependent photoconductivity can be employed to probe the modulation of the Fermi energy in graphene due to e.g., the environmental effect (see **Chapter 5**).

3 Hot-carrier cooling dynamics in high-quality graphene

Many promising optoelectronic devices, such as broadband photodetectors, nonlinear frequency converters, and building blocks for data communication systems, exploit photoexcited charge carriers in graphene. For these systems, it is essential to understand and eventually control the cooling dynamics of the photoinduced hot-carrier distribution. There is, however, still an active debate on the different mechanisms that contribute to hot-carrier cooling. In particular, the intrinsic cooling mechanism that ultimately limits the cooling dynamics remains an open question.

This chapter addresses this question by studying a technologically relevant system consisting of high-quality graphene with a mobility > 10,000 $cm^2V^{-1}s^{-1}$. Specifically, we study graphene in environments that do not efficiently take up the electronic heat from graphene, i.e., suspended graphene. We study the cooling dynamics of this high-quality graphene system using ultrafast pump-probe spectroscopy at room temperature. Cooling via disorder-assisted acoustic phonon scattering and out-of-plane heat transfer to the environment is relatively inefficient in this system, predicting a cooling time of tens of picoseconds. However, we observe much faster cooling on a time-scale of a few picoseconds. We attribute this to an intrinsic cooling mechanism, where carriers in the hot-carrier distribution with enough kinetic energy emit optical phonons. During phonon emission, the electronic system continuously re-thermalizes, re-creating carriers with enough energy to emit optical phonons.

We develop an analytical model that explains the observed dynamics, where cooling is eventually limited by optical-to-acoustic phonon coupling. These fundamental insights into the intrinsic cooling mechanism of hot carriers in graphene will play a key role in guiding the development of graphene-based optoelectronic devices.

3.1 Debate on graphene hot-carrier cooling mechanism

The ultrafast dynamics of photoexcited charge carriers in graphene have received ample attention, initially driven by a fundamental scientific interest in the intriguing electron-electron and electron-phonon interactions, *cf.* Refs. [10–14]. More recently, interest has multiplied due to the emergence of up-and-coming technological applications that exploit these ultrafast dynamics. One example is ultrafast photodetection of visible (VIS) and infrared light [7,128], and even terahertz (THz) radiation [129–131]. The ultrafast electronic response of graphene to incoming light has also led to the development of several concepts with relevance for data communication technologies, including modulators and receivers [18,132,133], and was demonstrated to be crucial for tailoring nonlinear photonics applications [134–137]. Part of the aforementioned applications, for instance, photodetectors and receivers, exploit the ultrafast photo-thermoelectric effect in graphene [58,138], where a longer hot-carrier cooling time leads to an increased photoresponse. Other applications, such as modulators, could instead benefit from a short cooling time, as this can lead to a higher modulation speed, i.e., to a larger bandwidth. Generally, these applications require high-quality graphene with high electrical

mobility. Clearly, it is crucial to understand the cooling dynamics of hot carriers in graphene properly, and in particular, to identify the intrinsic mechanism that ultimately determines the cooling process in high-quality systems.

The decay of photoexcited charges in graphene occurs through various dynamical processes that result from the specific properties of Dirac electrons and graphene phonons, as detailed described in **Section 1.2**. The hot-carrier state relaxes back to the ground state with the electronic system at ambient temperature after the carrier heating. These phonon-induced relaxation mechanisms have intricate dependencies on intrinsic (sample-dependent) parameters (such as disorder density and intrinsic doping), as well as extrinsic experimental parameters (such as photon energy, incident fluence, and ambient temperature). Thus, determining the dominant cooling channel(s) for excited graphene charge carriers has been challenging and is still a subject of debate.

It is generally believed that charge carriers with enough kinetic energy can relax on an ultrafast timescale of a few hundred femtoseconds by interacting with strongly-coupled optical phonons [11,69,139]. These are the optical phonons at the Γ and K points with an energy of 0.2 eV and 0.16 eV, respectively [84]. Thus, charge carriers with an energy > 0.16 eV above the chemical potential can efficiently cool by optical phonon emission [140]. Carriers with an energy < 0.16 eV can only couple to acoustic phonons, theoretically resulting in very inefficient cooling with decay times up to the nanosecond range [85]. In the case of graphene with a significant disorder, however, coupling to acoustic phonons becomes efficient through disorder-assisted scattering. By scattering with defects, the large momentum mismatch between electrons and acoustic phonons is overcome [86]. This disorder-assisted "supercollision" cooling process leads to typical cooling times of a few picoseconds at

room temperature, as measured by electrical [141], optical [75,142], and opto-electronic [16] techniques. Since disorder also limits electrical mobility, this disorder-assisted cooling mechanism plays an increasingly important role for graphene with lower electrical mobility, typically well below about 10,000 $cm^2V^{-1}s^{-1}$.
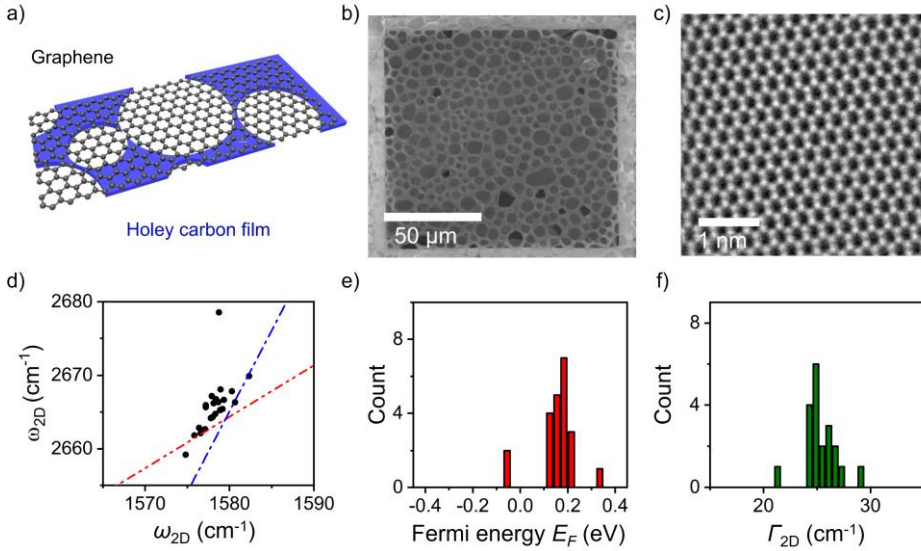
Figure 3.1 | Characterization of suspended high-quality graphene. (a) Sketch of graphene suspended on a holey carbon film. **(b)** Scanning electron microscopy images of suspended graphene on holey carbon, showing relatively large hole sizes and high yield. **(c)** TEM image of the suspended graphene, indicating the absence of disorder. **(d)** The plot of 2D peak frequency ω_{2D} as a function of G peak frequency ω_G. Dashed lines represent the expected dependence in the strain-free (red dot-dot-dashed line) and doping-free (blue dot-dashed line) material. **(e)** Fermi energy EF distribution extracted from vector decomposition of peaks positions in panel d [143], and centered at $|E_F| \approx$ 0.18 eV. **(f)** Obtained distribution of 2D-peak widths, indicating a mobility of > 17,000 $cm^2V^{-1}s^{-1}$, following calculations of Ref. [144].

In graphene with mobility above 10,000 $cm^2V^{-1}s^{-1}$, which we here refer to as "high-quality graphene", the disorder density is low enough that disorder-

assisted cooling will likely not play an important role. Recent experiments on high-quality *h*-BN-encapsulated graphene with mobility above $30,000\ \mathrm{cm^2 V^{-1} s^{-1}}$, however, did not show a strong increase in cooling time [17], as discussed in **Subsection 1.2.5**. The out-of-plane super-Planckian cooling for *h*-BN-encapsulated graphene occurs with a decay time of a few picoseconds at room temperature [17,100,105]. The important open question, therefore, remains: what is the intrinsic physical mechanism that ultimately limits the cooling of hot carriers in high-quality graphene?

3.2 Fast hot-carrier cooling dynamics in suspended graphene

Here, we address this question using time-resolved optical measurements of the cooling dynamics in a specifically chosen material system: suspended graphene. This system contains "high-quality" graphene, according to our definition of having a mobility $> 10,000\ \mathrm{cm^2 V^{-1} s^{-1}}$, which is high enough to make "supercollision" cooling inefficient. Furthermore, they basically have no substrate phonon environments, such that cooling to substrate does not play any role. We show that, despite eliminating these two relaxation channels, cooling still happens on a timescale of a few picoseconds. We attribute this to the high-energy tail of the hot-carrier distribution, where electrons with an energy $>$ 0.16 eV above the chemical potential reside. These electrons lose energy by coupling to optical phonons, which in turn couple to graphene acoustic phonons, while the electronic system continuously re-thermalizes. Probing the transient optical properties of graphene in the THz and VIS ranges, we will show that this cooling mechanism is consistent with the experimentally obtained cooling dynamics.

The high-quality suspended graphene contains large-area graphene grown by chemical vapor deposition (CVD), which was then transferred onto a transmission electron microscopy (TEM) grid, see **Figure 3.1a**. This was achieved through a polymer-free approach working with our collaborators Dr. Jincan Zhang and Prof. Huilin Peng at Peking University, using the method described in [145]. As a TEM grid, we used holey carbon, which is convenient as it has locations with relatively large holes with a diameter exceeding 10 µm. It has been shown that the graphene in such samples has mobility well over $10{,}000 \, \mathrm{cm^2V^{-1}s^{-1}}$ [146]. Given the large area and high quality of graphene prepared by this fabrication approach, which is furthermore scalable, this is a highly promising material system for a broad range of electronic and optoelectronic applications.

We characterize our suspended graphene sample using various microscopic techniques, see **Figure 3.1**. First, we show an image taken using scanning electron microscopy, evidencing excellent graphene coverage of the holes and providing an indication of hole sizes (see **Figure 3.1b**). TEM measurements furthermore show anatomically perfect lattices (see **Figure 3.1c**). We then perform Raman spectroscopy in order to estimate the Fermi energy and charge mobility of the suspended graphene. Performing a strain-doping analysis of the G-peak and 2D-peak, obtained from several positions on the sample (see **Figure 3.1d**), we obtain a distribution of carrier densities (see **Figure 3.1e**) which corresponds to an average Fermi energy of ~ 0.18 eV. Using the measured width of the 2D-peaks in **Figure 3.1d** and the empirical correlation of Ref. [144], we extract mobility of $> 17{,}000 \, \mathrm{cm^2V^{-1}s^{-1}}$. This result is in agreement with electrical measurements performed on a sample of suspended graphene, prepared in an identical way, see Ref. [146].
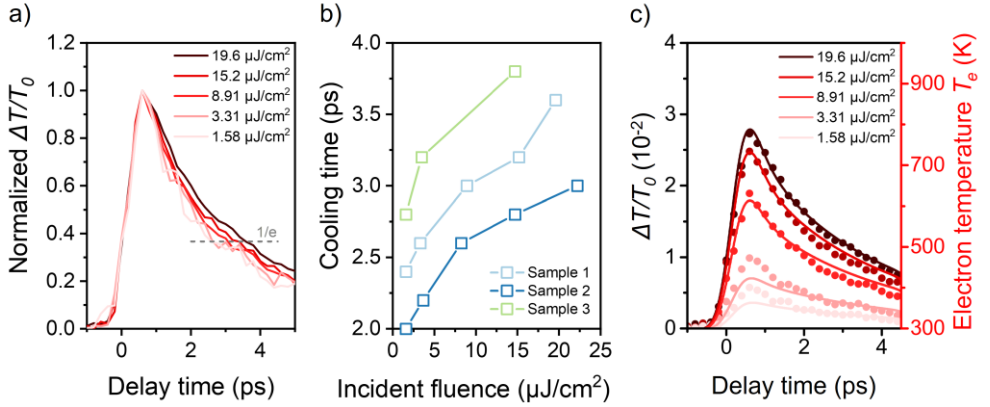
Figure 3.2 | Cooling dynamics of suspended graphene using THz pulses.
(a) Normalized OPTP dynamics for high-quality suspended graphene (Sample 1) with a pump photon energy of 1.55 eV (800 nm) and probe photon energy around 4 meV (1 THz). **(b)** Summary of cooling time defined by when the decays reach $1/e$ (grey dash line), for three high-quality suspended graphene samples. **(c)** OPTP dynamics for Sample 1 together with the calculated cooling dynamics for the electron temperature T_e (solid lines).

Having established the high quality of our suspended graphene sample, we now study its hot-carrier cooling dynamics using OPTP microscopy (see **Chapter 2** for details on the experiment), with a pump excitation at 800 nm (1.55 eV). We measured three high-quality suspended graphene samples. The experimental OPTP dynamics of Sample 1 are shown in **Figure 3.2c** for five different fluences. The right axis reports the temperature dynamics corresponding to the $\Delta T/T_0$ dynamics, showing an initial fast decay. We define the cooling time here by the time of decay at $1/e$ (see **Figure 3.2a**), and summarize their values for difference fluence in **Figure 3.2b**. As we can see, the hot carriers cool down quickly within $2 - 4$ ps for three samples. Quantitatively, however, based on the extracted mobility ($> 17,000$ cm^{2}V^{-1}s^{-1}) from Raman, disorder-assisted "supercollision" cooling would predict a longer cooling time

well above 10 ps for the suspended graphene sample (see **Figure 1.10b**), which is not what we observe.
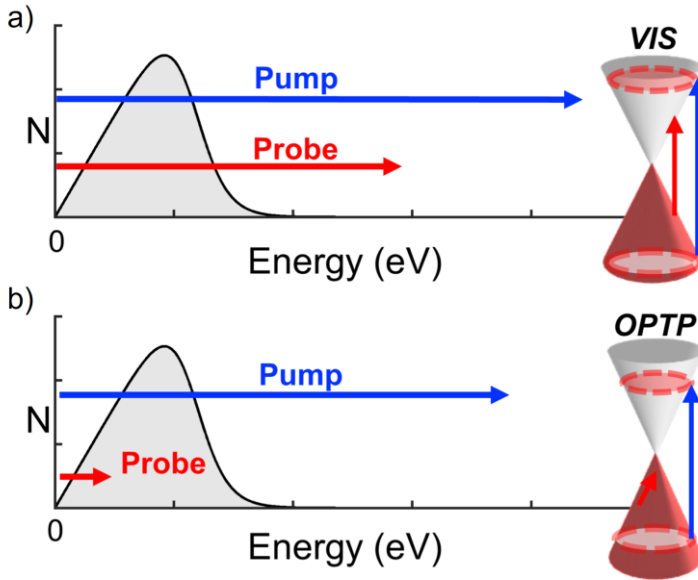
Figure 3.3 | Schematic illustration of the carrier density as a function of carrier energy compared to the pump and probe photon energies of the three experimental configurations that we used: (a) visible transient absorption (TA) and **(b)** optical-pump terahertz probe (OPTP). In all cases, the pump pulse is absorbed via interband transitions. For TA configuration, the probe pulse is also associated with interband transitions, whereas the THz probe pulses are associated with the intraband conductivity. This is also clear in the accompanying Dirac cones with energy vs. momentum.

In order to explain the relatively fast cooling dynamics observed in the suspended graphene, we, therefore, consider an intrinsic cooling mechanism based on the coupling of electrons with energy > 0.16 eV above the chemical potential to optical phonons. The optical phonons, at the Γ and K points, in turn, are anharmonically coupled to acoustic phonons. An important ingredient for this cooling channel is the continuous re-thermalization of the electronic system. Microscopically, this means that once the electrons with high enough

energy (more than 0.16 eV above the chemical potential) have relaxed by coupling to optical phonons, the remaining electrons will re-thermalize. This means that some electrons will end up with an energy that is high enough to emit optical phonons. Even at an electron temperature of 300 K, there are a significant fraction of electrons that can emit optical phonons. As a result, this is a relatively efficient cooling channel for graphene at room temperature. We will describe the analytical model of this cooling mechanism in more detail in the later sections.

We compare the experimental data to the calculated results on the cooling dynamics (for more details on the calculation, see **Section 3.3**). The calculation assumes the linear relation connecting the $\Delta T/T_0$ signal to the change in carrier temperature ΔT_e. As shown in **Figure 3.2**, the experimental data and calculated signal are in good agreement when we use an optical phonon lifetime of 1.2 ps and a Fermi energy of 0.15 eV. This optical phonon lifetime lies within the range of $1.2 - 2.55$ ps, previously reported [15,87,147–149] for graphene. We note that there is some underestimation of the signal magnitude for low fluences and some overestimation for higher fluences, which shows that the assumption of linear scaling between signal and temperature change is a simplification, as it is likely weakly sub-linear. However, the reasonable agreement between calculated and measured dynamics, confirms the validity of this intrinsic cooling mechanism. The slightly shorter optical phonon lifetime we extract by comparing the experimental data with the cooling model is likely the result of the assumption of linear scaling between OPTP signal and ΔT_e.
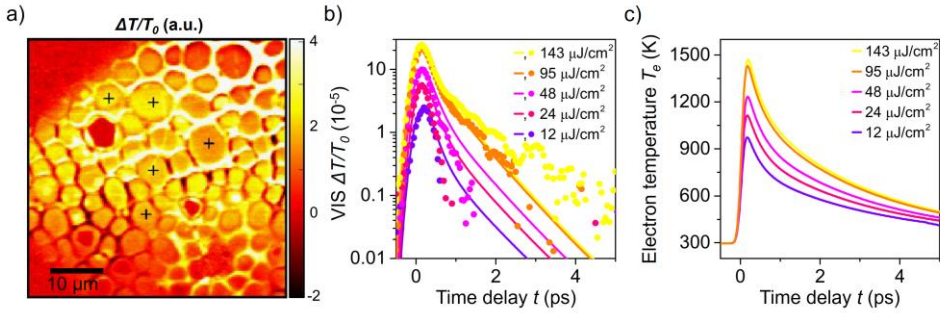
Figure 3.4 | Hot-carrier cooling dynamics of suspended graphene, measured by TA. (a) Transient transmission $\Delta T/T_0$ map at time zero, showing individual holes where graphene is suspended, acquired with pump tuned at 3.1 eV (400 nm) and probe at 1.55 eV (800 nm). **(b)** $\Delta T/T_0$ dynamics (coloured dots) for suspended graphene at five different pump fluences from 12 to 143 µJ/cm². The positive $\Delta T/T_0$ results from the pump-induced carrier heating that leads to decreased interband conductivity due to Pauli blocking, and thus reduced absorption of the NIR probe light. The colored lines are the calculated $\Delta T/T_0$ dynamics, based on the intrinsic cooling mechanism where hot electrons cool via the combination of emission of optical phonons, continuous re-thermalization of the electron distribution, and coupling of optical to acoustic phonons. **(c)** Dynamical evolution of the electron temperature T_e, corresponding to the calculated $\Delta T/T_0$ dynamics in panel b. Here, fast decay due to electron-optical-phonon coupling is followed by slower decay due to optical-to-acoustic phonon coupling.

As our next experimental test, we complement our OPTP measurements – which probe intraband transitions – with time-resolved transient absorption (TA) measurements – which probe interband transitions, see **Figure 3.3**. We work together with Dr. Alexander Block and Dr. Klaas-Jan Tielrooij at the Catalan Institute of Nanoscience and Nanotechnology (ICN2), using a pump tuned at 400 nm (3.1 eV) and a probe at 800 nm (1.55 eV). The TA and THz measurements have been conducted in the same samples to ensure a reliable comparison. In TA measurements, we observe photoinduced bleaching ($\Delta T/T_0 > 0$) of the probe, due to heating-induced Pauli blocking. Despite the

different optical transitions that are probed, both techniques essentially function as ultrafast electrical thermometers for graphene. This is because in both cases, the probe absorption is affected by pump-induced changes in the carrier temperature. The $\Delta T/T_0$ map at zero time delay (overlapping pump and probe pulses) in **Figure 3.4a** shows that we can resolve the individual holes spatially and that a clearly distinctive transient signal comes from inside – from the suspended graphene.

The experimental TA dynamics of our high-quality suspended graphene sample are shown in **Figure 3.4b** for five different fluences. Similar transient optical responses were observed in suspended graphene prepared by exfoliation, in the VIS (400 nm pump, 800 nm probe) [150], and in the NIR (830 nm pump, $1100 - 1400$ nm probe) [139]. We describe the dynamics with the same cooling mechanism as for OPTP results, with the optical-to-acoustic phonon coupling time of 2 ps and an $E_F = 0.15$ eV. **Figure 3.4c** reports the temperature dynamics corresponding to the $\Delta T/T_0$ dynamics in **Figure 3.4b**, again showing an initial fast decay due to coupling between electrons and optical phonons, followed by slower decay due to optical phonons coupling to acoustic phonons, which confirms the validity of this intrinsic cooling mechanism.

3.3 Efficient hot-carrier cooling by optical phonon collisions

We now discuss in more detail the cooling mechanism that we have used to describe the experimentally obtained cooling dynamics (schematically shown in **Figure 3.5a**). First, we note that in many early time-resolved studies on graphene, the dynamics were explained using a qualitatively similar mechanism involving electrons decaying to optical phonons, and a hot-phonon bottleneck,

cf. Refs. [87,139,150,151]. This mechanism, however, was thought to only mediate cooling for carriers with high enough energy to couple directly to optical phonons [152]. For the rest of the carriers in the hot-carrier distribution, alternative cooling channels were considered, such as disorder-assisted "supercollision cooling" to graphene acoustic phonons [16,75,86,141] and out-of-plane cooling to (hyperbolic) substrate phonons [17,100,105], which can both give rise to picosecond cooling at room temperature. In 2016, a microscopic, numerical simulation of the cooling dynamics of hot carriers in graphene was presented, based on electron-to-optical phonon coupling, and including rethermalization of the carrier system [140]. The calculated cooling times were used to explain qualitative trends in decay times measured by OPTP in samples of multilayer epitaxial graphene on SiC and monolayer graphene grown by CVD. These results motivated us to (re)consider cooling via optical phonons as the intrinsic cooling pathway for high-quality graphene, where disorder-assisted cooling and out-of-plane cooling are inefficient. The cooling mechanism is schematically explained in **Figure 3.5a**.

Dr. Alessandro Principi at the University of Manchester, developed an analytical model to describe the hot-carrier cooling dynamics in graphene. Briefly, the model is based on solving the following rate equations for the electron temperature $T_e(t)$, and phonon temperature $T_\alpha(t)$:

$$\begin{cases} C_e\big(T_e(t)\big)\partial_t T_e(t) = -\hbar \sum_\alpha \omega_\alpha \mathcal{R}_\alpha(T_e(t), T_\alpha(t)) \\ \mathcal{D}\big(\omega_\alpha, T_\alpha(t)\big)\partial_t T_\alpha(t) = \dfrac{\mathcal{R}_\alpha(T_e(t), T_\alpha(t))}{M_\alpha(T_e(t))} - \gamma_\alpha[n_\alpha\big(T_\alpha(t)\big) - n_\alpha\big(T_\alpha^{(0)}\big)] \end{cases}.$$

The left-hand side of the first rate equation contains the electronic heat capacity $C_e\big(T_e(t)\big)$ and the temporal derivative of the electron temperature. The

right-hand side describes the emission of optical phonons, where the sum is over the two optical phonon modes (labeled by α), at the Γ and K point, ω_α is the frequency of mode α, and $\mathcal{R}_\alpha(T_e, T_\alpha)$ is the rate of α -phonon emission. The rate is calculated analytically using a Boltzmann-equation approach, which contains one important input parameter, namely the electron-phonon coupling strength. For this, the value 11.4 eV/Å is used, obtained by density functional theory calculations, and verified by experiments [153]. The left-hand side of the second rate equation contains $\mathcal{D}(\omega_\alpha, T_\alpha) = \partial n_\alpha(T_\alpha)/(\partial T_\alpha)$, where $n_\alpha(T_\alpha)$ is the phonon occupation function. The righthand side contains the first term due to the emission of optical phonons by electrons, where the parameter $M_\alpha(T_e)$ measures the size of the portion (an annulus) of the phonon Brillouin zone that is heated in the electron-cooling process. This parameter depends, assuming the phonon dispersion to be flat, on the maximum momentum that can be exchanged between electrons and phonons, and thus on the electron temperature T_e. The second term describes the decay of optical phonons to acoustic phonons, where $T_\alpha^{(0)}$ is the equilibrium phonon temperature, i.e., the lattice temperature T_L. For the optical phonon decay term, the model uses the parameter γ_α as a phenomenological damping rate. There are essentially two adjustable parameters in the calculations: the optical phonon lifetime γ_α^{-1}, and the a parameter that governs the temperature dependence of the phonon number density.
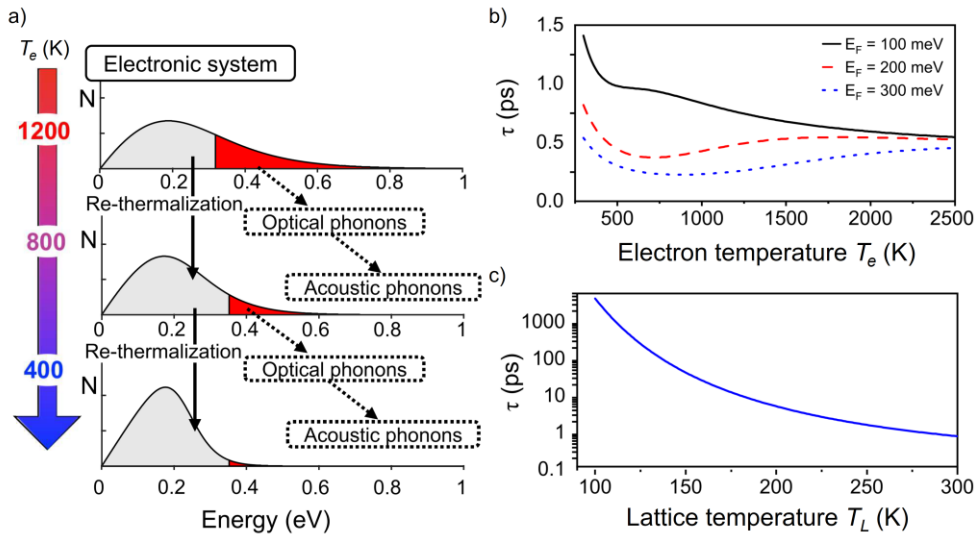
Figure 3.5 | Hot-carrier cooling dynamics in high-quality graphene. (a) The process of electronic cooling is explained through schematics of the carrier density as a function of carrier energy for three electron temperatures (1200, 800, and 400 K). Cooling occurs through a combination of i) optical phonon emission by electrons with energy > 0.16 eV above the chemical potential (red-shaded area) ii) re-thermalization of the electronic distribution, and iii) anharmonic coupling of optical phonons to acoustic phonons. **(b)** Calculated "instantaneous" cooling time for a given initial electron temperature for three different Fermi energies. **(c)** Calculated cooling time as a function of lattice temperature T_L for a very small ΔT_e and $E_F = 0.03$ eV. For panels b-c, cooling occurs through optical phonon emission and continuous re-thermalization of the electronic system. The hot-phonon bottleneck is not included.

We have seen that our experimentally obtained cooling dynamics can be accurately described by this analytical model. The hot-phonon bottleneck, occurring when the density of emitted optical phonons is so high that they cannot completely decay into acoustic phonons and part of their energy is scattered back to the electronic system, becomes more and more important with increasing initial T_e, and it leads to an overall slower cooling of the graphene hot carriers. For applications operating with a small heating ΔT_e, however, cooling is

ultimately determined by electron-optical-phonon cooling. This regime is likely relevant for applications that require low power consumption with low light intensities. Therefore, the model analytically studies the cooling in the absence of the hot-phonon bottleneck, i.e., when $\gamma_\alpha \to \infty$. The calculation, in this case, shows that cooling at room temperature takes between $\sim$ 500 fs, for $E_F = 0.3$ eV, and $\sim$ 1.4 ps for 0.1 eV. Cooling to optical phonons will quickly become less efficient upon decreasing the lattice temperature T_L. Around 200 K, the calculation shows a cooling time around 5 ps, whereas this increases to $\sim$ 4 ns at 100 K (see **Figure 3.5c**). When ΔT_e is not small, the effect of increased cooling time with decreased lattice temperature is much weaker. Thus, obtaining a longer intrinsic cooling time requires a reduction of both T_L and ΔT_e.

3.4 Conclusion

Using two different time-resolved measurement techniques (OPTP and TA) on one high-quality, technologically relevant graphene systems – suspended graphene, we have shown that hot carriers decay through an intrinsic mechanism involving optical phonon emission and constant re-thermalization of the electronic system. Electrons with an energy > 0.16 eV above the chemical potential couple to optical phonons, which in turn decay to acoustic phonons while the electronic system continuously re-thermalizes. The electron-to-optical-phonon cooling component gives rise to sub-picosecond cooling. Due to the hot-phonon bottleneck governed by the anharmonic coupling of optical to acoustic phonons, an approximately bi-exponential cooling occurs, where the second decay component has a characteristic timescale of a few picoseconds. The overall decay becomes slower for increasing initial electron temperature

(higher incident fluence) due to the hot-phonon bottleneck. The analytical model suggests that this mechanism will quickly become less efficient upon decreasing the ambient temperature T_L, provided that also the amount of heating is small $\Delta T_e < T_L$. Thus, operating graphene with low incident fluence and at reduced ambient temperatures is likely a promising approach to optimize optoelectronic applications exploiting hot carriers in graphene.

4 Controlling hot-carrier cooling dynamics by solvent dielectrics

In this chapter, we investigate the role of solvent dielectrics on the hot carrier cooling dynamics in graphene using OPTP spectroscopy. Our results indicate that the hot-carrier cooling can be tuned drastically by varying its dielectric environments. For solvents with the static dielectric constant $\epsilon < 20$, we observe that an increase in ε extends the hot-carrier lifetime in graphene. We rationalize the observation as a consequence of solvent with a specific dielectric constant, which screens the electron-electron (e-e) scattering. Therefore the solvent dielectric contacting causes a slowing-down in the hot-carrier thermalization and overall cooling process. On the other hand, with increasing ϵ further beyond 20, we find a negative correlation between cooling time and ϵ: i.e., the cooling time decreases with increasing with ϵ. This could be rationalized by considering two effects: (1) the dielectric constant at corresponding frequencies for charge carrier conduction and carrier-carrier scattering is much lower the static ϵ in polar solvents such as water; and (2) the surface-induced alignment of polar molecules can restrain the rotation of dipoles, resulting in further reduction of ϵ for solvents near graphene interfaces.

4.1 Motivation: controlling hot-carrier cooling in graphene

The ultrafast dynamics of photogenerated charge carriers in graphene has a strong impact on the performance of graphene-based optoelectronics. For many applications, e.g., photo-thermoelectric effect (PTE) photodetectors, long-lived hot carrier dynamics is preferable, as hot carrier-assisted intrinsic

photoresponse can be substantially enhanced [79]. On the other hand, some optoelectronic applications may profit from faster cooling. Therefore, it is paramount to achieve control over hot-carrier cooling dynamics in graphene, both for fundamental research and applications.
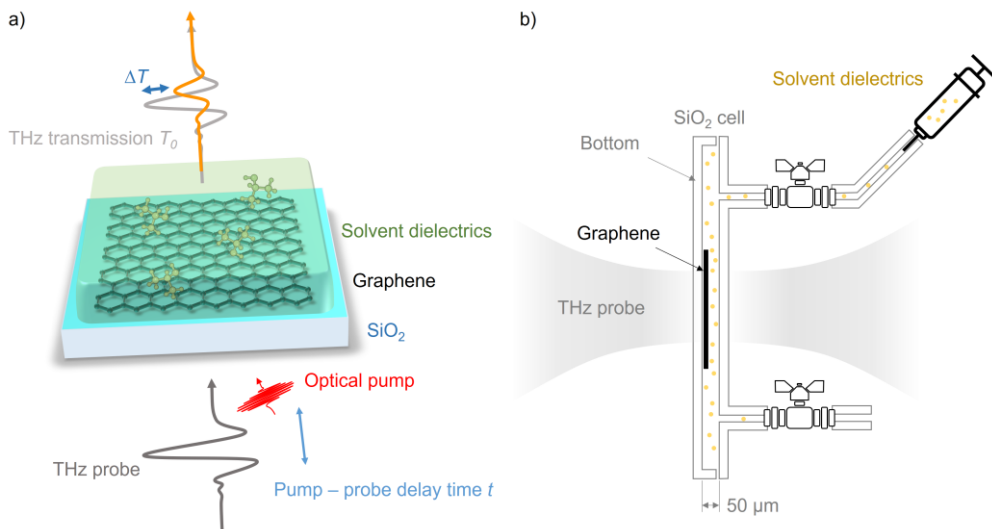
Figure 4.1 | Schematic illustration of optical pump-THz probe (OPTP) spectroscopy on the graphene/solvent dielectric system, with the graphene supported on one side of a silica (SiO₂) flow cell. (a) Graphene in contact with solvent dielectrics is photoexcited by a femtosecond laser pulse (in red) optical pump. The photo-induced photoconductivity is then probed by a THz probe pulse (in light grey). **(b)** Schematics of *in situ* measurement using a silica cell. A demountable flow-through cell connected to tubes enables us to switch the solvents attached to graphene. Such a demountable cell allows us to transfer a graphene layer onto the left silica slice. Once we inject a solvent, we close the two valves to make sure there is no flow impact. During the measurement, the position of the silica cell is fixed. Therefore, we always measure at a fixed spot of graphene.

The hot carrier lifetime in graphene is governed by the energy dissipation rates of hot electrons into environments, via e.g., optical- and acoustic-phonon emissions [67,85], disorder-assistant cooling [16,86,93], substrate cooling

paths [17,97,105], and plasmons [108,110,154]. Consequently, in principle, tuning the hot carrier cooling can be achieved by controlling "disorder" in graphene and its substrate [86]. In addition, the cooling time by disorder-assisted "supercollision" is tunable by controlling the ambient temperature of graphene [16]. However, such controlling requires cryogenic environments and not commonly practicable. Recently, tuning of hot carrier cooling in bilayer graphene has been achieved by controlling the pressure. The hot carrier dynamics has been reported to be accelerated using a high-pressure diamond anvil cell due to the possible intermediate phonon scattering path between high-frequency optical phonon and acoustic phonon under GPa order pressure [155]. While this method is effective, it remains challenging for practice implement due to limited access to high-pressure facilities. Therefore, developing a reproducible, easy and straightforward method for controlling hot-carrier cooling in graphene is desirable for both research and applications.

Here we report that tuning the dielectric environment of graphene can be exploited to effectively tune hot-carrier lifetime in graphene. For the solvent with static dielectric constant $\epsilon < 20$, we observe that increase in ε prolongs the hot-carrier lifetime in graphene. We attribute this effect to the dielectric screening the e-e scattering, leading to slower thermalization and overall slower cooling dynamics. With increasing ϵ further, interestingly, we observe an inverse correlation between cooling time and ϵ. Along with taking into account the frequency-dependent dielectric effect in a polar solvent, our results may be rationalized by a reduction in the effective ϵ of solvent near graphene, owing to the surface-induced alignment of polar molecules. Our findings reveal a critical role of dielectric engineering on hot carrier cooling and provide

convenient methods to control hot carrier dynamics for optoelectric applications.

4.2 Dielectric dependent graphene hot-carrier cooling dynamics

Here we adapt a silica flow cell (see the sketch in **Figure 4.1b**) to investigate the role of solvent dielectrics on the hot carrier cooling dynamics of graphene. For transferring CVD-grown graphene on the copper foil to SiO_2, cellulose acetate butyrate (CAB) dissolved in ethyl acetate is spin-coated on top of graphene. Subsequently, the copper is first etched in 3g/100 ml ammonium persulfate ((NH_4)$_2S_2O_8$) aqueous solution filtered by a 0.2 µm Nylon membrane filter in advance. After rinsing the CAB/graphene in Milli-Q water, we transfer the CAB/graphene (1 cm $\times$ 1 cm) on a silica slice, which serves as a detachable window for the flow cell. After the transferred CAB/graphene on SiO_2 is completed dried, the CAB is removed in an acetone bath for 12 hours. We carry out all steps in dust-free environments.

We characterize the initial Fermi level of graphene on silica by Raman spectroscopy and find it to be $|E_F| = \sim100$ meV. The silica window where graphene is on, is then mounted onto the counterpart to complete the cell. The thickness of the solvent is defined to be ~50 micrometers (µm) by the thickness of two sides of the window, ensuring sufficient THz transmission after some degree of THz absorption by the solvent. During the studies, we inject a solvent of interest into the silica cell by a syringe, bringing the graphene directly in contact with solvents. To exclude the effect of inhomogeneity of graphene and for a reliable comparison, we conduct all the THz measurements at

a single spot of the graphene sample by varying only the composition of solvents.

Sequence	Dielectrics	Bulk dielectric constant (ϵ)*
1	N$_2$	~1
2	Toluene	2.37
3	1-Hexanol	13.08
4	Acetophenone	17.40
5	Isopropanol (IPA)	19.4
6	Ethanol	24.30
7	Methanol	33.0
8	Milli-Q water	78.36

Table 4.1 | Sequence of measurements and bulk dielectric constants of the dielectric contacts on graphene. *Static dielectric constant at 298.2 K from [156].

To monitor how the dielectric constant ϵ of a solvent affects the graphene hot carrier dynamics, we employ optical pump-THz probe (OPTP) spectroscopy as detailed described in **Chapter 2**, with an 800 nm laser pulse with sub-100 fs duration photo-excites graphene. Subsequently, we record the modified THz transmission induced by the pump as a function of delay time [118] between the optical excitation pulse and the THz probe (**Figure 4.1a)**. This technique provides not only the photoconductivity of graphene [12,80,82,89,92, 157–160], but also time evolution of electronic temperature or cooling dynamics in graphene following optical excitations, by straightforwardly monitoring the time-dependent differential transmission $\Delta T/T_0(t)$. The change in transmission scales roughly linearly with the carrier temperature change ΔT_e for low excitation fluences [12,80,92].
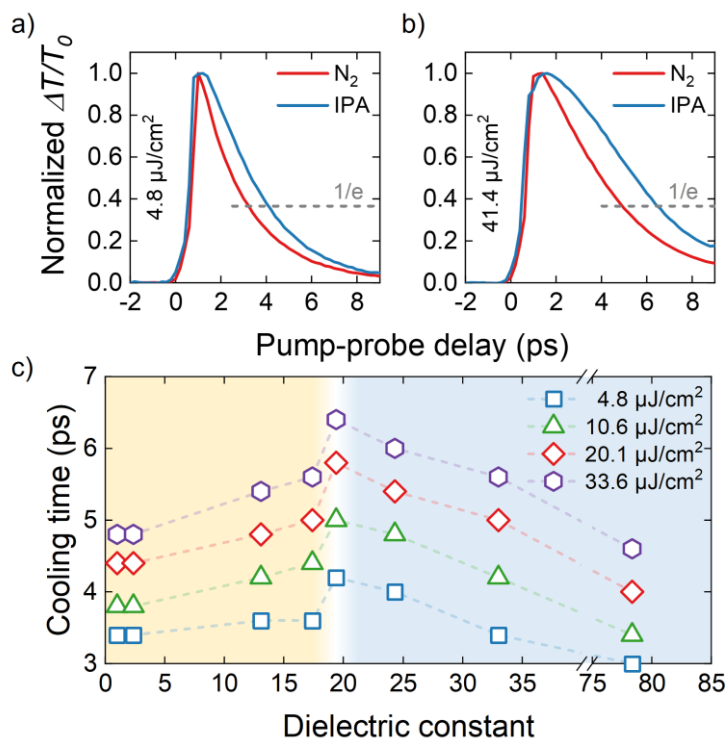
Figure 4.2 | The effect of solvent dielectrics on the hot carrier dynamics.
(a-b) Normalized OPTP dynamics of graphene in contact with IPA compared
to that in N_2 at low fluence $4.8 \, \mu J/cm^2$, and high fluence $41.4 \, \mu J/cm^2$. **(c)**
Cooling times for varied pump fluences for a series of solvent dielectrics with
the ε range from 1 (N_2) to 78.4 (Milli-Q water).

To interrogate the effect of the solvents, or more specifically, the role of the
dielectric constant of the solvents on the hot carrier dynamics of graphene, we
first measure graphene dynamics without solvent, e.g., in a purged try N_2 ($\epsilon \sim 1$)
atmosphere as a reference. Then, we systematically study seven different sol-
vents listed in **Table 4.1,** with a large tuning in static dielectric function from
~ 2.4 to ~ 78.4 All of measurements are conducted in a fixed sample spot. The
pump-probe scheme is designed in such a way, that both pulses go through first

graphene and then solvents, to ensure a similar incident excitations for graphene. The solvents solution does not absorb the excitation light and therefore show no differential terahertz response.
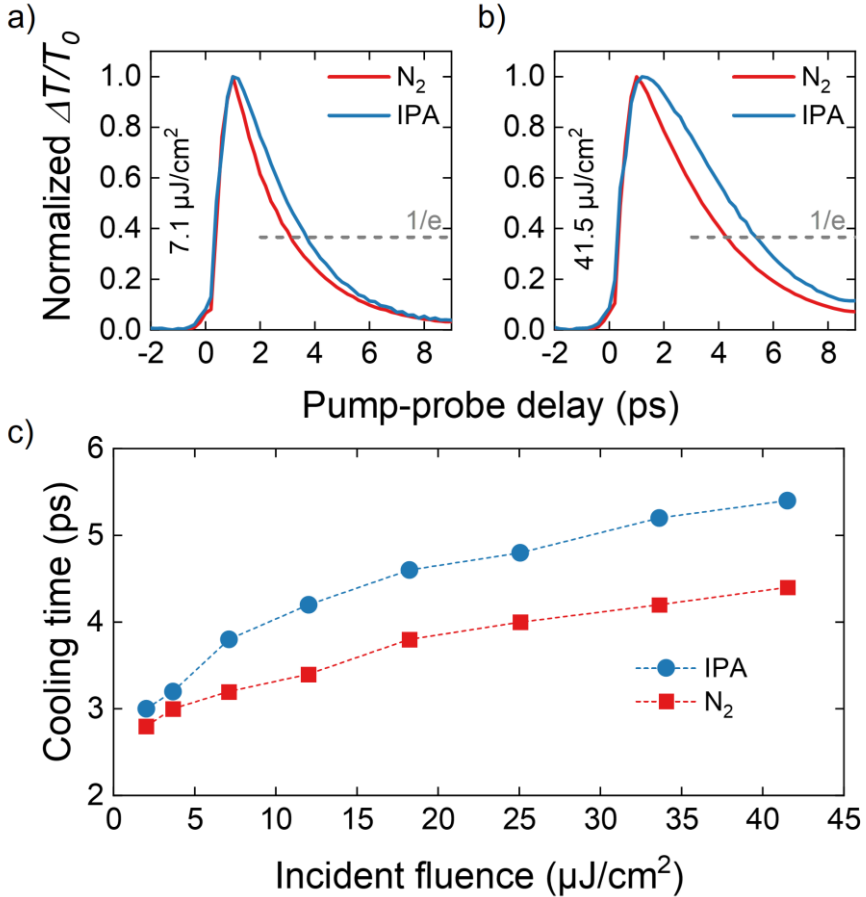
Figure 4.3 | The solvent dielectrics effect measured from a second graphene sample. (a) Normalized OPTP dynamics of graphene in contact with IPA compared to no solvent contact at low fluence $4.8 \, \mu J/cm^2$. **(b)** Normalized OPTP dynamics of graphene in contact with IPA compared to no solvent contact at high fluence $41.4 \, \mu J/cm^2$. **(c)** Cooling time for N_2 ($\epsilon = 1$) and IPA ($\epsilon = 19.4$) contact as a function of incident pump fluence.

In **Figure 4.2a** and **b**, we compare the conductivity dynamics for graphene in the dielectric environments of N_2 and IPA (with $\epsilon = \sim 20$). As clearly shown, we observe a slower cooling dynamics for graphene in contact with IPA than that in N_2 atmosphere. We define the cooling time τ as the time difference from the photoconductivity peak to its $1/e$ amplitude as $\tau_{\text{cooling}} = t_{1/e} - t_{\text{peak}}$. The cooling time contrast between N_2 and IPA increases with fluences.

To further quantify the dependence of the cooling time on the nature of the solvents, here we define the cooling time phenomenologically by the time period, during which the photoconductivity dynamics decays from 100% to $1/e$ of its maximum value. We summarize the cooling time of all solvent dielectrics as shown in **Figure 4.2c**. We reproduce the result by a second graphene sample, see the summary in **Figure 4.3**. The results indicate two distinct regimes for tuning hot carrier cooling via solvents: with increasing ϵ, the cooling time first increases and reaches a maximum for $\epsilon = \sim 20$. With further increasing ϵ further, the cooling time decreases.

4.3 Dielectric effect on the hot carrier cooling

Before concluding that tuning the hot carrier cooling dynamics originating purely from the dielectric effect, we need to exclude other possible scenarios, e.g., modification of cooling dynamics by changing the carrier density in graphene induced by the chemical doping from solvents. This is because, for hot-carrier cooling via "supercollision", the cooling time is predicted to depend on the graphene Fermi energy by altering the phonon space size available for collisions between electrons and acoustic phonons [86,93]. To this end, we monitor the G band position ω_G by Raman spectroscopy, from which the Fermi

level E_F can be obtained (following a well-established empirical correlation $\omega_G - 1580 \text{ cm}^{-1} = (42 \text{ cm}^{-1}/\text{eV}) \times |E_F|$ [161]). As shown in **Figure 4.4**, comparing graphene in N_2 and in contact with IPA (the solvent in which graphene shows the slowest cooling time), the chemical doping induced by IPA results in a tiny shift of Fermi level of $\sim$10 meV. Within this negligible change in chemical potential, the cooling time in graphene is expected to show no observable changes.
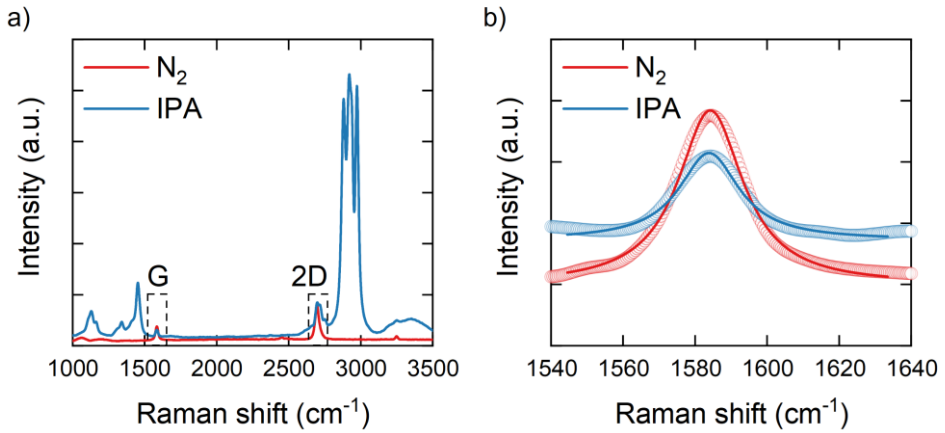
Figure 4.4 | Raman spectroscopy of graphene in N_2 and IPA. The G peak position shifts from 1584.3 cm^{-1} for graphene without solvent contact to 1583.9 cm^{-1} for graphene in contact with IPA, corresponding to a minor change of $\sim$0.4 cm^{-1}.

By excluding the doping effect from the solvent contact, now we discuss how our results can be rationalized from the perspective of the dielectric effect on hot carrier cooling. The dielectric screening from the environments is a well-known effect, which can drastically affect the e-e scattering process. A recent study illustrates that high dielectric proximity induced by a metal-gate can strongly suppress e-e scattering in monolayer graphene when the gate is

placed at a distance of about 1 nm [162]. For the solvent directly contacting with graphene, with increasing ϵ (for $\epsilon < 20$), effective dielectric screening of charge carrier can result in a reduced e-e scattering in graphene. As discussed in **Chapter 3**, the hot-carrier cooling process in graphene under normal conditions (no solvent dielectrics) involves both emissions of optical phonons (to dissipate the energy of the electronic system) and e-e scattering (to thermalize and/or rethermalize the electronic system). The e-e scattering occurs much faster than the phonon emission – tens of femtosecond compared to hundreds of femtosecond for phonon emission. In principle, the e-e scattering time scales with ϵ^2. Therefore, a finite increase in dielectric environments may substantially increase the e-e scattering time beyond the lifetime of optical phonon emissions. This results in a cooling of nonthermalized hot carriers by directly emitting optical phonons, and thus slower cooling dynamics.

By only taking into account the dielectric effect, in principle, by increasing the static dielectric constant beyond 20, one expects a further increase in the cooling time of graphene. The fact that the cooling time peaks at $\epsilon = \sim 20$, indicate that in very polar solvents, another effect comes into play. Here we discuss the two plausible scenarios by taking into account (1) the frequency-dependent dielectric function of polar solvents and (2) the interfacial dipole alignment effect. As we will see, both effects could result in a reduced effective dielectric constant, which is insufficient for screening the e-e scattering (and thus a fast cooling dynamics) in graphene.

Firstly, although a static dielectric constant is used here as a physical parameter to indicate the screening effect, it is not a good indicator for the screening effect to take place in high frequencies as in our case. In the polar solvents, the high static dielectric constant originates from the alignment of molecular

dipole moments in response to applied external fields. The dipole reorientation or so-called dielectric relaxation requires time and usually takes several pico-seconds [163], which is substantially slower than the e-e scattering. As such, the relevant dielectric constant relevant for e-e scattering process is expected substantially lower for polar solvents.

Secondly, it has been reported that polar molecules in a solvent are more likely to be less mobile due to the dipole interactions at the interfaces [164–167]. Atomistic molecular dynamics simulations at the nanoscale show that surfaces modify water dipolar fluctuations up to tens of nanometers where the out-of-plane fluctuations are suppressed; in contrast, the in-plane ones are enhanced [166,167]. This results in strong anisotropies in the dielectric relaxation components, which originates from the very presence of interfaces [167]. Experiments have shown that water may form ice-like ordered layers near surfaces [168–170]. The rotational freedom of highly polarized solvent molecules like water has been experimentally proven to decrease near surfaces [171]. This dramatic effect reduces the dielectric constant of polar solvent near interfaces. The dielectric constant ε of water drops from 80 to about 1.8 under strong interfacial effects [171]. Our observation of decreasing of hot carrier cooling for $\epsilon > 20$ is also consistent with an effectively lower dielectric constant for polar solvent at graphene surfaces, and dielectric screening effect discussed above.

4.4 Conclusion

To summarize, employing optical pump-THz probe spectroscopy, we investigate the role of a series of solvents with various static dielectric constant ϵ ranging from 2.4 to 78.4, on the hot-carrier cooling dynamics of graphene.

For ϵ below 20, we observe the cooling time of graphene increases with increasing ϵ. This result can be explained by a dielectric screening of charge carriers in graphene induced by the solvent, leading to a suppressed electron-electron scatting process. This gives rise to the direct cooling of non-thermalized hot carriers via electron-optical phonon emissions. For very polar solvents, our result indicates that interfacial ϵ has a reducing effect, which reverses the relation between cooling time and ϵ. These findings provide both new insights as well as practical methods to control and study the hot carrier dynamics in graphene and potentially other low-dimensional materials. Furthermore, we propose the dielectric contact methods as a practical solution to tune the graphene's photoresponse.

5 Hot-carrier dynamics at graphene/electro-lyte interface[*]

Thanks to its outstanding electrical properties and chemical stability, graphene finds widespread use in various electrochemical applications. Although the presence of electrolytes strongly affects its electrical conductivity, the underlying mechanism has remained elusive. Here, we employ terahertz spectroscopy as a contact-free means to investigate the impact of ubiquitous cations (Li^+, Na^+, K^+, and Ca^{2+}) in an aqueous solution on the electronic properties of SiO_2-supported graphene. We find that, without applying any external potential, cations can shift the Fermi energy of initially hole-doped graphene by ~200 meV up to the Dirac point, thus counteracting the initial, substrate-induced hole doping. Remarkably, the cation concentration and cation hydration complex size determine the kinetics and magnitude of this shift in Fermi level. Combined with theoretical calculations, we show that the ion-induced Fermi level shift of graphene involves cationic permeation through graphene. The interfacial cations located between graphene and SiO_2 electrostatically counteract the substrate-induced hole doping effect in graphene. These insights are crucial for graphene device processing and further developing graphene as an ion sensing material.

5.1 Graphene's usage in electrochemical systems

Graphene finds extensive use in various electrochemical applications, including ionic sensing [172,173], biochemical detection [174,175], lithium-ion batteries [176], dye-sensitized solar cells [177] and super-capacitors [178,179], thanks to its outstanding electrical and mechanical properties, large surface-to-volume ratio and excellent chemical stability. Despite its critical importance for these applications, the effect of electrolyte solutions on the electronic properties of graphene has remained poorly understood. There is particular debate regarding the microscopic mechanism underlying the effect of aqueous solutions on graphene's conductivity $\sigma = ne\mu_m$. While it is apparent that the presence of (aqueous) electrolyte solutions affects the conductivity of graphene, it is typically not straightforward to disentangle how μ_m and n are affected. In the case of polymer electrolyte solutions, it was found that they are extremely effective in inducing electron/hole doping in graphene through ions located in the Debye layer on top of graphene [180]. The effect of cations has been primarily ascribed to cations absorbed on the surface of graphene, where they also act as charge scattering centers [181–183], thus affecting μ_m. On the other hand, ions and water molecules have previously been reported to be able to permeate through the graphene layer via atomic defects [184–186]. While this process has been demonstrated to be useful for molecular separation and ionic sieving [184,187], its impact on the electronic and optoelectronic properties of graphene has not been considered and investigated. In addition, for graphene in contact with aqueous solutions, ion-induced variations of the charge carrier density n, the role of defects in graphene and the supporting substrate, have remained elusive or mostly unexplored.

5.2 Size-dependent cation induced doping effect in graphene
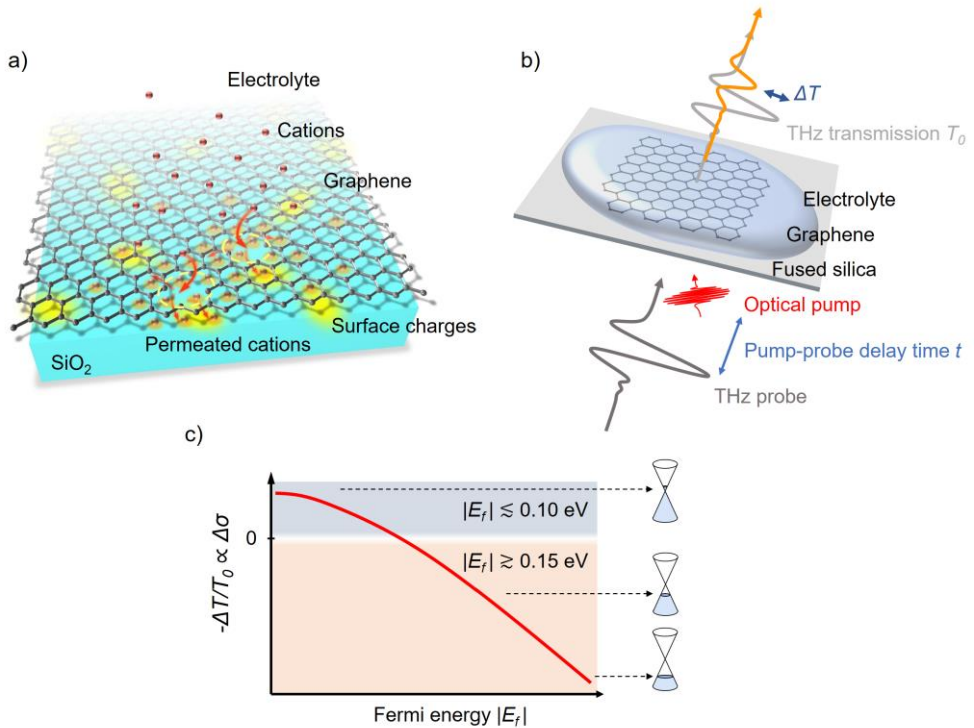
Figure 5.1 | Concept of cation-induced Fermi level shift in graphene and its measurement. (a) Illustration of cation permeation through the graphene sheet to the graphene-SiO$_2$ interface. Graphene is initially hole-doped due to the presence of negative surface charges (indicated in yellow) on the SiO$_2$ surface. Intercalated cations lead to a shift of the Fermi level of graphene towards the Dirac point. **(b)** Schematic picture of optical pump-THz probe (OPTP) spectroscopy on the graphene/electrolyte system, with the graphene supported by fused silica (SiO$_2$). **(c)** Illustration of typical Fermi energy-dependent THz photoconductivity $-\Delta T/T_0$ in graphene as discussed in **Section 2.5**. This distinct sign change allows us to assign the effect of cations on the graphene conductivity to a change in Fermi level.

Here, employing optical pump-THz probe (OPTP) spectroscopy as a non-contact, all-optical method to determine the conductivity, we investigate the impact of a series of cations (based on chloride salts XCl or YCl$_2$, with X =

Li$^+$, Na$^+$, K$^+$, and Y= Ca^{2+}) in aqueous solution on the electrical conductivity of graphene supported by SiO$_2$. We demonstrate that metal cations affect the conductivity mainly through a strong electrostatic effect that shifts the Fermi level towards the Dirac point ($\Delta E_F \sim 200$ meV). Through kinetic measurements, we find that it takes 10s of minutes for the Fermi energy shift to complete, where the timescale of this process depends critically on the solvation radius of the cations. We rationalize the concentration- and size-dependent cation-induced Fermi level shift that we observe as follows: cations permeate through pores or atomic defects in graphene (as schematically illustrated in **Figure 5.1a**) and diffuse further in between the graphene-SiO$_2$ interface. Through electrostatic effects, most likely involving screening of the negatively charged SiO$_2$ surface by the intercalated cations, the p-type doping effect from the substrate is counteracted. Based on first-principles calculations, we find that, in line with our experimental observations, cations favor residing in between graphene and SiO$_2$, rather than on top of graphene. Our report reveals the process of cation permeability through graphene and its impact on the electronic properties of graphene, highlighting the importance of interfacial chemistry for graphene's applications in electrochemistry and electronics. These results have implications for graphene-based ion sensing devices, graphene device processing, and possible applications of graphene in desalination membranes.

We study the electrolyte effect on the electronic properties of graphene using monolayer graphene grown by chemical vapor deposition (CVD) that is transferred onto a fused silica (SiO$_2$) substrate, which was performed by Karuppasamy Soundarapandian at the Institute of Photonic Sciences (ICFO). As typically observed, this leads to hole-doped graphene. The origin of this *p*-doping effect has been widely studied. Employing first-principles simulations,

Nistor *et al.* identified the (negatively charged) dangling oxygen bonds present in the SiO_2 substrate as one of the main sources [188]. Other origins, including hole donating impurities either in the substrate lattice or on the graphene surfaces (such as molecular O_2) have been reported and proposed [189–191]. We characterize the initial Fermi level of graphene on silica (without electrolyte) by Raman spectroscopy, and find it to be $|E_F| = 220 - 280$ meV (below the Dirac point). We then bring the graphene in contact with electrolytes, by sandwiching the electrolyte of interest between the graphene (supported by SiO_2) and a top SiO_2 glass; we limit the thickness of the electrolyte by a Teflon spacer to be ~ 10 μm, to ensure sufficient THz transmission. In our study, the fluence of the laser pump is chosen such that we observe no change of THz conductivity of graphene over 1 hour of measurements, as shown in **Figure 5.A.1** in **5.A Appendix**. This indicates that our technique is noninvasive and does not create new defects or increase the size of existing defects.

To monitor how cations affect the graphene conductivity, we again employ optical pump-THz probe (OPTP) spectroscopy (see **Chapter 2**) with 800 nm pump pulse to photoexcite graphene as shown in **Figure 5.1b**. The reason for this is that the sign and magnitude of the pump-induced THz photoconductivity ($-\Delta T/T_0$ or $\Delta\sigma$) are directly correlated to the Fermi energy in graphene, as we illustrate in **Figure 5.1c**, which is detailed discussed in **Section 2.5**. Thus, by monitoring the sign and magnitude of the changes in THz conductivity, we readily obtain the modulation of the Fermi energy in graphene. Importantly, this enables us to unambiguously disentangle changes in carrier density from changes in carrier mobility.
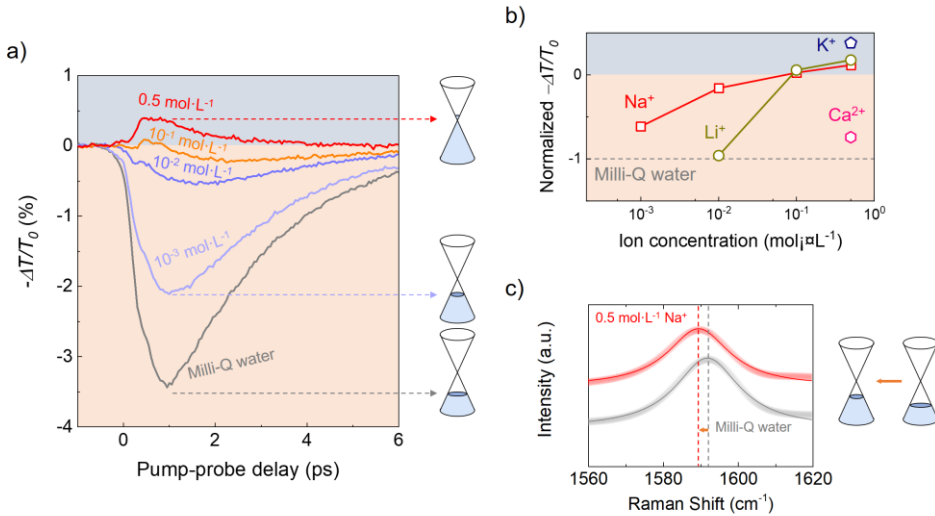
Figure 5.2 | The effect of cations on the THz photoconductivity and Raman spectrum of graphene. (a) Cation (Na^+) concentration-dependent THz conductivity ($-\Delta T/T_0$) dynamics. The dynamics are recorded when the signal is saturated after graphene in contact with electrolyte. **(b)** The peak value of the pump-induced THz conductivity for various ions (Li^+, Na^+, K^+, Ca^{2+}) as a function of ion concentration. All data points are normalized to the THz conductivity value in Milli-Q water (shown as the gray dashed line). **(c)** Raman spectroscopy of graphene in the electrolyte. The G peak positions are 1592.1 cm^{-1} for graphene in 0.01 M Na^+ and 1598.2 cm^{-1} for Milli-Q, respectively. This indicates a shift of the Fermi level towards the Dirac point, as shown in the schematics on the right.

To interrogate the effect of the electrolyte, or more specifically, the role of hydrated cations in aqueous solution on the carrier conductivity in graphene, we study four different metal chloride solutions with various cation sizes: KCl, NaCl, LiCl, and CaCl$_2$. To quantitatively study the effect of cations on Fermi level, we fix the anion to Cl$^-$ and the solvent to H$_2$O, thus focusing on the effect of cations. First, we investigate the effect of ionic concentration on the pump-induced THz conductivity (referred to as "THz photo-conductivity" below) of

graphene for the four different electrolytes. The electrolyte solutions do not absorb the excitation light and therefore show no differential terahertz response. We show typical results for NaCl in **Figure 5.2a**: the electrolyte gives rise to a decrease in the magnitude of the negative conductivity in graphene, using the THz photoconductivity of graphene in contact with Milli-Q water as a reference. At sufficiently high concentrations, the sign of the photoconductivity becomes positive (> 0.1 M for NaCl as presented in **Figure 5.2a**). Following the discussion related to **Figure 5.1b**, and given the fact that the initial doping of our graphene is p-type ($\sim 220 - 280$ meV below Dirac point), we conclude that the NaCl electrolyte induces a shift of the Fermi level towards the Dirac point (i.e., less hole doping) by an amount $\Delta E_F \sim 200$ meV.

As an independent verification of the observations using OPTP measurements, we perform Raman measurements, which allow for extracting the change of Fermi level in graphene. As shown in **Figure 5.2c**, we observe a shift of the G band from 1598.2 cm^{-1} for graphene in contact with 0.01 M NaCl electrolyte, to 1592.1 cm^{-1} for graphene in contact with Milli-Q water, corresponding to a shift of Fermi level of ~ 150 meV toward Dirac point, in agreement with our OPTP results (~ 200 meV upshift of the Fermi level in graphene by 0.5 M NaCl electrolyte).

In the following, we vary the cation concentration and study how this affects the THz photoconductivity with respect to that of graphene in contact with Milli-Q water as a reference. We summarize the cation-induced effect on the THz photoconductivity of graphene (by taking the peak values charge carrier dynamics shown in **Figure 5.2a**) for a series of cations with varying ionic concentration, as shown in **Figure 5.2b**. Whereas all electrolytes show qualitatively the same effect (less negative photoconductivity and thus a Fermi energy

shift towards the Dirac point), the achieved final Fermi level in graphene dis-
plays an obvious cation size effect with a trend from the largest shift for K^+
(with the smallest solvation radius ∼3.3 Å among all cations studied
here [192]), to the smallest change for Ca^{2+} (with the largest solvation radius
∼4.1 Å for the cations used [192]). Sodium and lithium ions with similar size
of hydrated radius have comparable effects at high concentrations. In our study,
we use the hydrated ion (solvation) radius (defined as the radius of the hydra-
tion sphere of the ions), rather than the ion radius, since the solvation radius is
relevant for transport in an aqueous solution.

5.3 Tracking the cation induced doping kinetics in graphene

To further investigate the underlying mechanism for the observed size-de-
pendent cation effect on the Fermi level, we monitor *in situ* the kinetics of the
Fermi level changes by tracking the THz photoconductivity as a function of
graphene-electrolyte contacting time. In **Figure 5.3a,** for graphene in contact
with a 0.5 M sodium chloride solution, the ion-induced Fermi level shift is not
an instantaneous process. Instead, it takes ∼80 minutes for the THz conduc-
tivity of graphene to gradually turn from negative to positive (corresponding
to a change from hole-doped graphene to graphene with a Fermi energy in the
vicinity of Dirac point). We also study these cation-induced dynamics for gra-
phene in contact with cations of different concentrations and sizes. First, we
measure the ionic effect induced by 10^{-2} M and 0.5 M NaCl electrolyte at the
same sample spot of a graphene sample, as demonstrated in **Figure 5.A.2a**.
The time required for reaching the final Fermi energy is much shorter for ele-
vated concentrations (∼80 minutes vs. 150 minutes to change the THz con-
ductivity sign from negative to positive for 0.5 M in comparison to 10^{-2} M

NaCl, respectively). Secondly, we compare concentration-dependent THz conductivity measurements for K^+, Li^+, and Ca^{2+}. For a reliable comparison, we conduct all the THz measurements in a single spot of a graphene sample and fix the cationic concentration to be 0.5 M for all cases (for all original data, see **Figure 5.A.2b**). We describe the normalized time-dependent dynamics of the photoconductivity change by a single exponential process, as indicated by the solid lines in **Figure 5.3b**. We plot the inferred exponential timescales and the final photoconductivity as a function of the solvation radius of the cations in **Figure 5.3c** and **d**. It appears that all three small cations (Li^+, Na^+, K^+) used here can effectively modify the carrier density of graphene. However, cations with a bigger ionic solvation radius ($K^+ < Na^+ < Li^+$) require an increasingly longer time to achieve the Fermi level shift. For the largest hydrated ions Ca^{2+}, we observe a rather slight change in graphene's conductivity, and, thus, Fermi energy. Finally, it is worth commenting that although the trend of the size-dependent kinetics and degree of Fermi energy shift induced by cations (as shown in **Figure 5.3c** and **d**) is highly reproducible for all samples, we find that the absolute changes (e.g., doping time and magnitude) are varied from sample to sample, presumably due to the variations in doping and defect densities (see the extended discussion in the next section) of graphene used here.
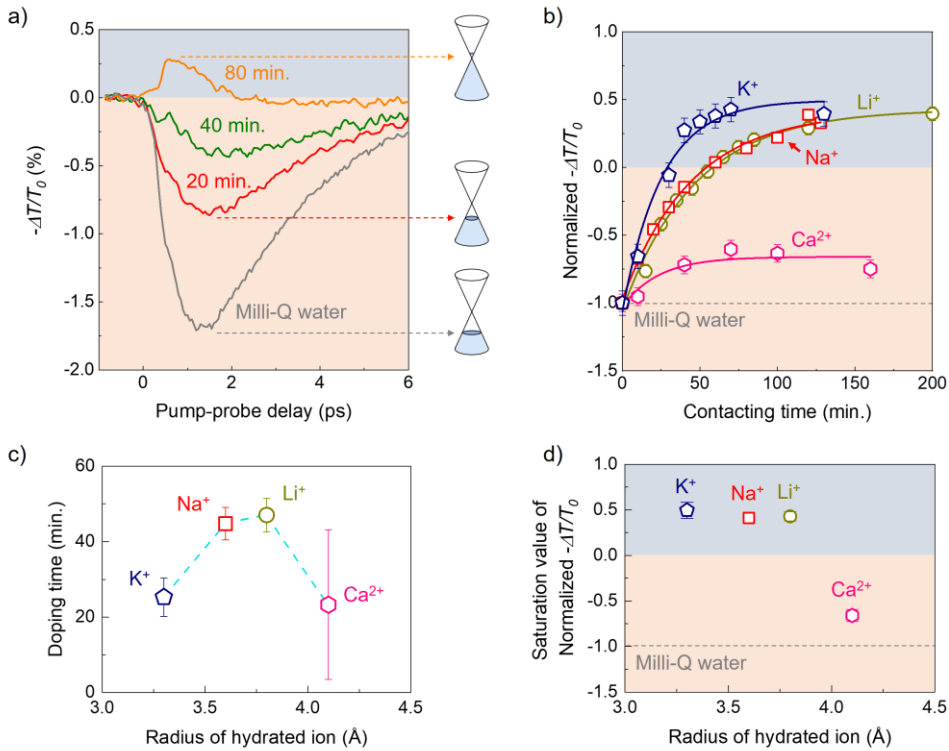
Figure 5.3 | Time evolution of the cation-induced Fermi level shift in graphene. (a) The kinetic sodium ion (Na^+) induced Fermi level shift in graphene, as revealed by monitoring the pump-induced change in THz transmission depending on the contacting time of sodium ion solution, 0.5 M NaCl aqueous solution. All measurements are conducted in the same spot of a graphene sample. **(b)** The peak value of the pump-induced THz change $-\Delta T/T_0$ as a function of contacting time for metal cations including K^+, Na^+, Li^+, and Ca^{2+}, respectively. All data points are normalized to the same starting point for a better comparison. **(c)** The doping time is plotted as the function of the radius of the hydrated ion. **(d)** The archived final Fermi levels (representing by the cation-induced THz conductivity changes in graphene) *vs* the hydrated cation radius.

5.4 Ionic permeation and interfacial doping of supported graphene

The observed cation-induced change in Fermi energy (more specifically, the reduced hole density) challenges the intuitive and straightforward view that the cations are located on the top surface of graphene (which would not give rise to the observed slow, size- and time-dependent doping processes), and that they act only passively as scattering centers, solely modifying the carrier mobility. Instead, our results here can be explained by an ionic process that involves concentration-, size- and time-dependent permeation of metal cations through atomic defects in graphene [184–186]. The intercalated cations in between the graphene and substrates surfaces then electrostatically screen the *p*-doping effect of the SiO_2 substrate, thus resulting in graphene with reduced *p*-doping. In principle, an atomically perfect graphene lattice is impermeable for all ions except for protons (H^+), thus acting as an ideal sieve to protons from other cations [187]. This picture, however, does not hold for large-area graphene with inevitable atomic defects, e.g., missing carbon atoms resulting in nanopores. Indeed, permeation of ions and water molecules through graphene atomic defects has previously been reported [184–186], and selective cation transport through graphene nanopores has also been demonstrated [184–186,193–195]. Moreover, based on AFM measurements of the CVD graphene used here (see **Figure 5.A.3**), we find disorder and grain boundaries and holes in the size range of up to several micrometers, which can be the initial sites for cation intercalation. As such, cation permeation is kinetically possible in our CVD graphene, and is thermodynamically favorable (which is further supported by the simulation discussion in **Figure 5.4**). The cations tend to move

to the supported silica surfaces and remain intercalated between graphene and the silica substrate, due to the negative surface potential of silica at neutral pH. The permeated cations can subsequently diffuse in-plane, away from the defect centers, along with the graphene-SiO$_2$ interface.

For a certain size and amount of atomic defects in graphene, ionic permeation, as well as the subsequent diffusion of ions intercalated between graphene and SiO$_2$, depend critically on the size of the hydrated ions [185,186,193–195]. Therefore, we expect cationic permeation and in-plane diffusion to speed up with smaller solvated ion size, as we indeed observe. When the size of hydrated cation or hydrated cation complex (as for the case of Ca^{2+} [196]) further increases to be comparable or bigger than the defects or nanopore size in graphene, the ionic blockade can take place [193], also in accordance with our experiment.

To further support our explanation and model of ionic permeation and the resultant shift of the Fermi energy of graphene by the intercalated cations, we highlight two additional experimental observations. First of all, following the equilibration of the graphene/silica system with a specific electrolyte solution, we exchange that solution with pure water and investigate the reverse process of Fermi level shift ("re-doping") (**Figure 5.A.2c**). We find that substrate-induced hole doping is recovered after rinsing away the solutions containing the cations Li$^+$, Na$^+$, and K$^+$. The recovery of the doping level in the absence of ions exhibits distinct size-dependent kinetics (detailed discussion in **Figure 5.A.2**). If the cations did not intercalate between SiO$_2$ and graphene, we would expect the ions to dissolve very quickly back into the water when the graphene is contacted with pure water. Instead, we observe a timescale on the order of

tens of minutes and a clear dependence on ion hydration size, thus corroborating our picture of intercalated cations. Secondly, we find that the relative change in THz conductivity (and thus Fermi level shift) for a given ionic composition and concentration, is much more pronounced when the graphene contains fewer polymer residues (by comparing two sets of graphene samples using different post-transfer treatments, details in **Figure 5.A.4**). We rationalize that the Fermi level shift depends crucially on the sample cleanness, i.e., when the cation permeation pathway is blocked by the polymer residuals; a smaller change in carrier density in graphene is achieved.

Simulations. Min Hu and Prof. Dr. Jun Jiang at the University of Science and Technology of China run first-principles calculations by which they explore the interaction between SiO_2-supported graphene and electrolyte solutions. The simulations are based on spin-polarized density functional theory (DFT) calculations as implemented in the Vienna ab initio simulation package (VASP) [197,198], using Perdew-Burke-Ernzerhof (PBE) [199] functionals and the plane-wave projector augmented wave (PAW) [200] method with van der Waals (vdW) interactions.

In the optimized structure of supported graphene, the Si-O bond lengths are in the range of $1.60 - 1.62\,\text{Å}$, in good agreement with previous studies [201,202]. The binding energy of -0.84 eV for a unit cell of the complex system is calculated as the energy difference between the bonded system and the isolated parts, suggesting high stability. They then add a Na atom (consisting of Na^+ ion plus an electron) into the model system to investigate the cation effect on graphene. To simplify the calculation, here only Na^+ is included in the simulation, and charge neutralization is realized by adding an electron instead of Cl^- anion. Despite the simplicity of the model, it captures the essence

of the cation-graphene interaction and explains our experimental data well (as shown below). First of all, they investigate the energetics for two configurations of Na^+ either on top of graphene or residing between graphene and the SiO_2 support. As shown in **Figure 5.4a**, the calculation results clearly illustrate that it is energetically more favorable for the cation to reside in between graphene and SiO_2 than to be adsorbed at the top surface of graphene, in good agreement with the conclusions from the experiments. Furthermore, they explore the kinetic Na^+ permeation processes for graphene with (e.g., single vacancies and double vacancies) and without atomic defects (details in the **5.A Appendix**). The permeation of Na^+ through a perfect graphene layer is associated with a prohibitively high energetic barrier (> 10 eV). The presence of a double vacancy reduces the barrier to 0.69 eV (3.22 eV with a single vacancy, as shown in **Figure 5.A.5**), which is comparable to the penetration barrier of 1.2~1.6 eV for a proton to migrate through the perfect graphene mono-layer [187]. Finally, to investigate the impact of intercalating cations on graphene, they compute the density of states (DOS) of the complex with and without Na^+ (**Figure 5.A.6**). The Fermi level appreciably shifts towards less negative values (from -0.93 eV to -0.49 eV) when Na^+ is included in the complex. **Figure 5.A.7** shows the partial DOS of the C atoms around Na^+. Substantial *p*-orbitals of these carbon atoms emerge in the vicinity of up-shifted Fermi level, suggesting that the new filled state originates from electrons in the *p*-orbitals of the C atoms in the vicinity of interfacial Na^+. The shift of Fermi level in the complex system induced by Na^+ is in line with the experimental results.
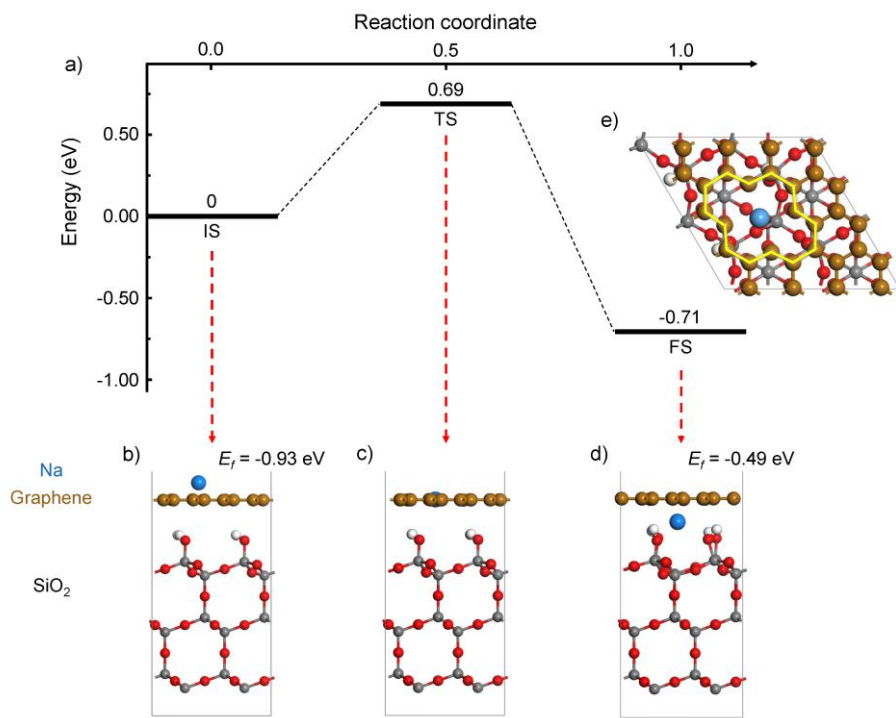
Figure 5.4 | Simulation of cation effect at the graphene/SiO₂ interface.
(a) The system energetics for Na adsorbing at graphene top surface, the energy barrier for Na permeation through a graphene double vacancy defect, and Na residing at graphene-SiO₂ substrate interfaces. **(b-d)** modeled atomic structures in cross-section views corresponded to the three energy states in (a). When Na is at graphene top surface and at SiO₂ surface beneath graphene, the calculated Fermi energies of the system are -0.93 eV and -0.49 eV, respectively (details in **Figure S5**). **(e)** Na residing at graphene-SiO₂ substrate interfaces after it permeates through a double vacancy defect (highlighted as a yellow polygon).

5.5 Conclusion

To summarize, employing optical pump-THz probe spectroscopy as a contact-free, all-optical conductivity measurement, we investigate the role of a series of cations with various solvation radius (based on chloride salt XCl and YCl₂ with X = Li⁺, Na⁺, K⁺, and Y = Ca²⁺) on the electrical conductivity of

graphene. We observe a cation-induced shift of the Fermi level in excess of 200 meV towards the Dirac point in graphene. Combined with theoretical calculations, such an ionic effect in graphene appears to involve cationic permeation through defects in graphene, which is kinetically controlled by the interplay of hydration radius of cations and the size of atomic defects in graphene.

These findings not only provide a new tool to monitor the ionic dynamics at graphene and potentially other materials interfaces but also offer new insights into the role of cation permeability through graphene and the influence of ion interfacial dynamics on electronic properties. Finally, these results are of interest for electrochemical charge and energy storage, graphene device processing (where, e.g., etching chemical or electrolytes are extensively in use), desalination membranes, and ionic sensing devices. Regarding the last case, controlling the size and density of atomic defects in graphene, as well as the nature of surface charges in supporting substrates can serve as effective and novel approaches to enhance the ionic sensitivity and specificity.

5.A Appendix

1. Electrolyte contacting. We control the volume of electrolyte precisely with a micropipette. We sandwich the electrolyte between two pieces of fused silica with the graphene being transferred on the bottom one and exposed to the electrolyte. The layer thickness of the electrolyte is controlled by a Teflon spacer to be ~10 μm. In each measurement, we fix the sample in the OPTP setup to the same position to prevent the doping inhomogeneity of graphene controlled by a translational stage. During the changing of each electrolyte, we use a small piece of absorbent paper to absorb the original electrolyte gently

from the edge of fused silica to avoid the damage of graphene, following by Milli-Q water rinsing, to remove the permeated ions at the interface.

2. The computational methods and details. The energy cutoff for the plane-wave basis set is 520 eV. The convergence criteria for structure relaxation are 10^{-5} eV on the energy and 0.01 eV/Å on the residual force of each atom. The Brillouin zone was sampled with a Monkhorst-Pack mesh with $3 \times 3 \times 1$ k-point grids.

Min Hu and Prof. Jun Jiang at the University of Science and Technology of China (USTC) simulate the interaction between graphene and SiO_2 surfaces using the repeated-slab model of three layers, and we set the vacuum separation to be 15 Å [203]. To model the amorphous SiO_2 (α-SiO_2) used in the experiment in the periodic DFT calculation, we use the β- cristobalite crystal reported to possess a similar structure to α-SiO_2 as an approximation. This approach has been adopted by other authors as well [204–206]. The cristobalite silica surface contains the (111) and (100) faces mainly [207,208]. The Bravais-Donnay-Friedel-Harker method shows that the β-cristobalite (111) plane is the dominant plane for SiO_2. Therefore, the (111) plane is simulated for the surface of the substrate. For the 1×1 surface of β-cristobalite, the 4×4 supercell of graphene has a negligible mismatch of lattice constants. For the simulation of the substrate in electrolytes, we employ a fully hydroxylated SiO_2 surface, which has been reported as a good approximation of the substrate [209].

3. Appendix figures
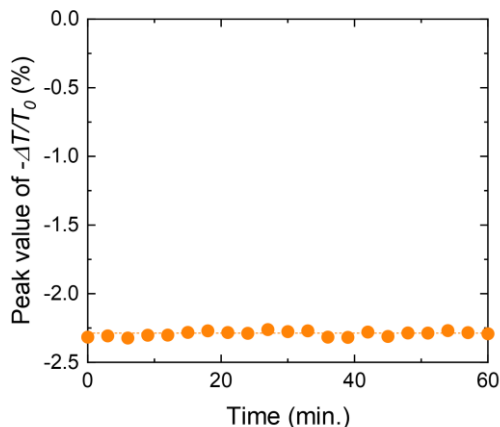
Figure 5.A.1 | The stability of graphene in laser excitation. The photo-conductivity signal (peak value of $-\Delta T/T_0$) of graphene as the function of laser excitation time.
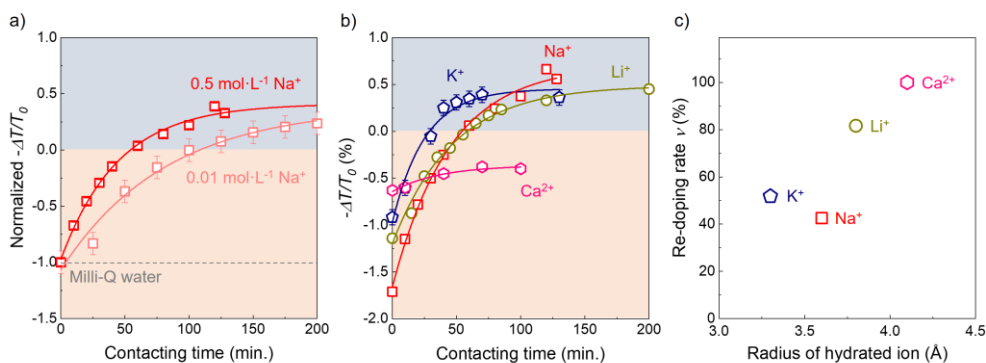
Figure 5.A.2 | Evolution of the cation-induced Fermi level upshift in graphene. (a) The peak value of the pump-induced THz change $-\Delta T/T_0$ as a function of Na$^+$ concentration. **(b)** The peak value of $-\Delta T/T_0$ as the function of electrolyte contacting time. **(c)** The reversibility of the cation doping effect on graphene. Here we plot the "re-doping rate v" (defined in the **Figure 5.A.2 Note**) *vs* the hydrated cation size.

Figure 5.A.2 Note: We note that, for sufficiently long immersion (up to several hours), the doping level returns to the initial doping level, indicating

that the cation doping effect is thermodynamically reversible. The doping re-covery, or reverse doping process, however, can be kinetically controlled by the cation size and Milli-Q water washing or immersion time. In order to quan-titatively compare the cation size-dependent reverse doping kinetics, we define here a parameter "re-doping rate v" as the relative THz conductivity recovery from the final doping towards the initial doping, after immersing cation treated graphene into Milli-Q water for 10 minutes (see more experiments details in the supplementary information). The re-doping rate v is ranging from 0% (i.e., rinsing is ineffective to remove the cation doping effect) to 100% (i.e., com-pletely back to the initial doping). Remarkably we observe size-dependent reverse doping kinetics, which is inherently connected to the doping kinetics, as discussed in the following: (1) For three small cations K^+, Na^+, Li^+, which give rise to strong electron doping effect, we observe that after 10-minute im-mersion of graphene into Milli-Q water, none of them go back to the initial doping. Generally, the re-doping rate is very similar as $40 - 50\%$ for Na^+ and K^+, and dramatically increase with increasing the hydrated ionic size (80% for Li^+) and eventually approached to 100% for the Ca^{2+} (the largest solvated ion used here). This observation is in line with the size-dependent cation doping effect: the larger the ion, the less doping in graphene, and thus the faster the de-doping. The size-dependent reverse doping kinetics discussed here, pro-vides further strong evidence that cation doping and reverse doping processes involve cation permeation through defects in graphene, and interfacial interca-lation or diffusion along with the graphene-SiO_2 interfaces.
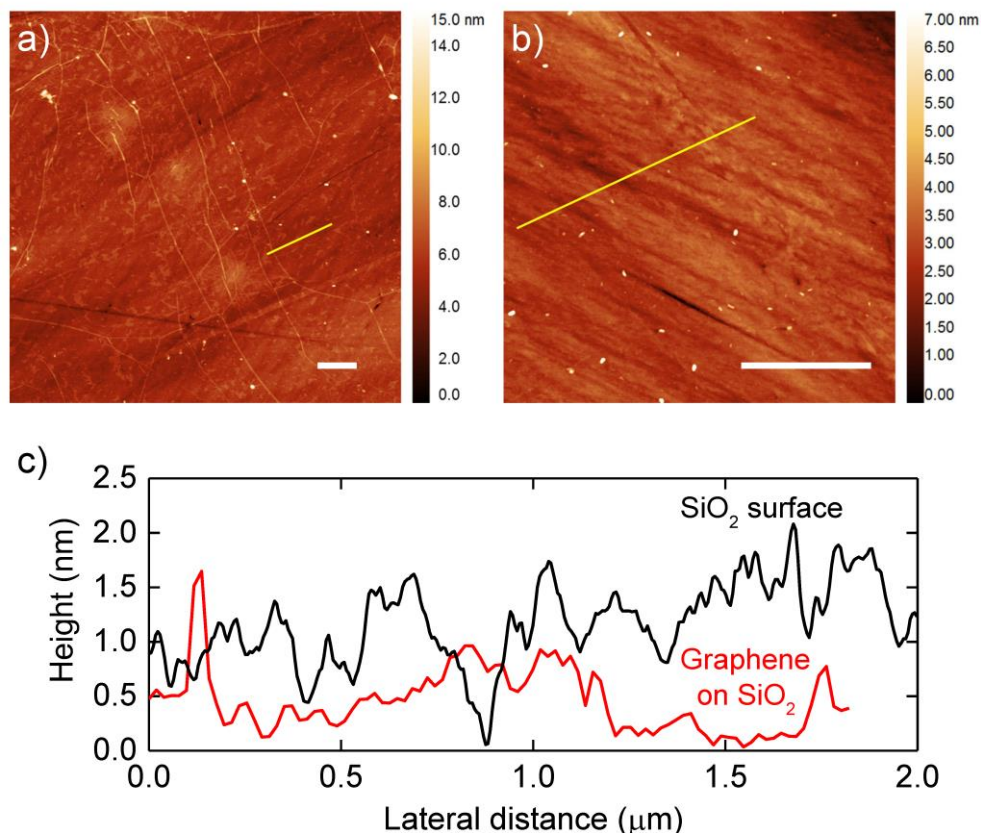
Figure 5.A.3 | Surface characterization of graphene on SiO₂. (a) AFM image of the graphene on fused silica. **(b)** AFM image of the same fused silica before graphene transfer. The scale bars in (a) and (b) (white lines) are 1 μm. **(c)** Line profile along the guided golden lines in (a) and (b). The black curve shows the surface roughness for fused silica which has been used in the experiments with roughness in the range of 1.23 nm. It is clear the roughness (0.54 nm) for graphene-covered SiO₂ sample is much less than that of the fused silica surface.
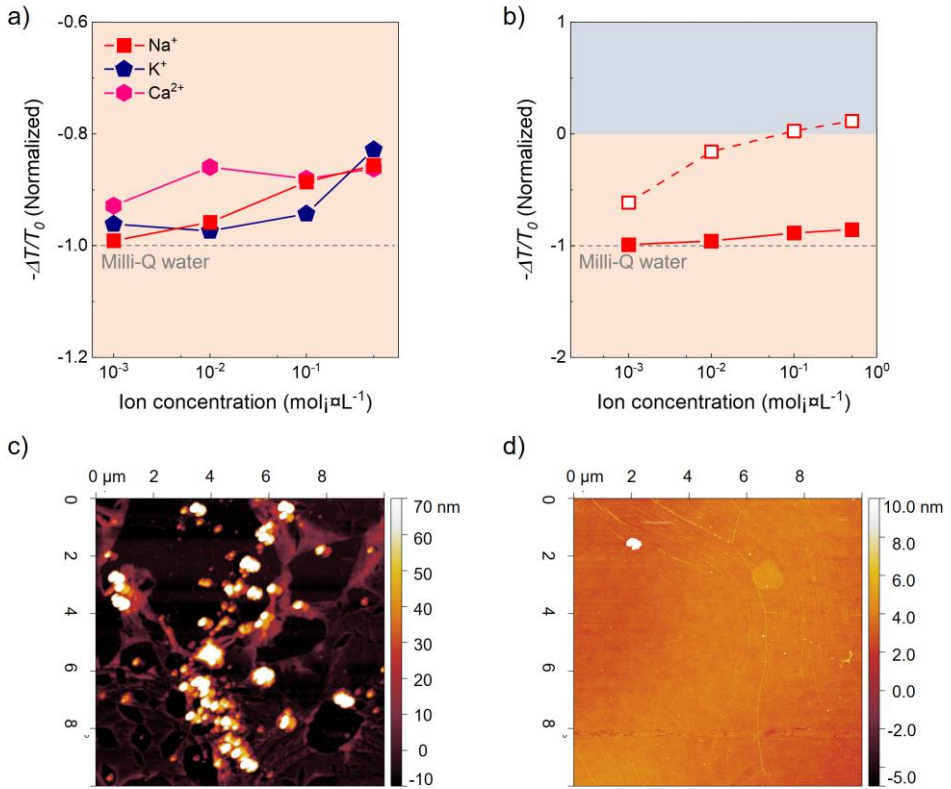
Figure 5.A.4 | The comparison between less-clean graphene and clean graphene on fused silica. (a) The peak value of the pump-induced THz conductivity for various ions (Na⁺, K⁺, Ca²⁺) as a function of ion concentration, measured on less-clean graphene on fused silica. All data points are normalized to the THz conductivity value in Milli-Q water (shown as a gray dashed line). **(b)** The peak value of the pump-induced THz conductivity for sodium ions (Na⁺) as a function of ion concentration, measured on less-clean graphene (red filled squares) and clean graphene (red open squares) on fused silica. **(c)** AFM images of one typical area of less-clean graphene on fused silica. **(d)** AFM image of one typical area of clean graphene on fused silica.
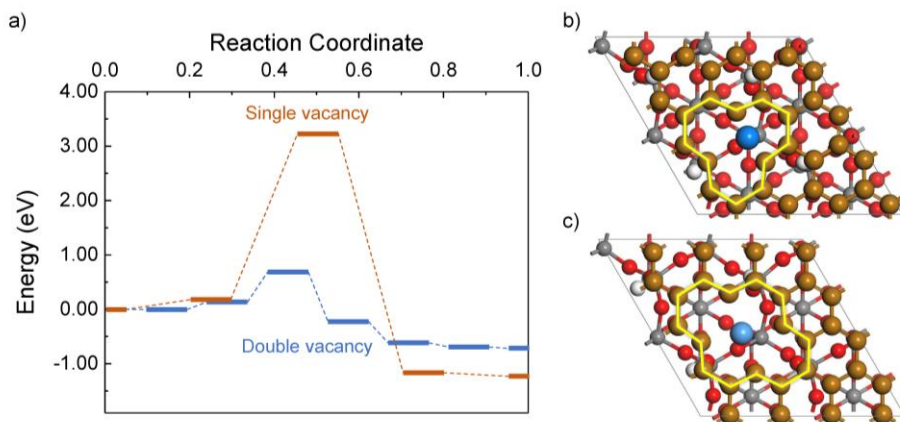
Figure 5.A.5 | The energy landscape and modeled structures for Na⁺ ion penetrating vacancies. (a) The energy landscape for Na⁺ adsorbed at graphene top surface, the energy barrier for Na⁺ permeation through a vacancy defect, and Na residing at graphene-SiO_2 substrate interfaces for single and double vacancies, respectively. **(b)** Na⁺ residing at graphene-SiO_2 substrate interfaces after it permeates through a double vacancy defect (highlighted as a yellow polygon). **(c)** Na⁺ residing at graphene-SiO_2 substrate interfaces after it permeates through a single vacancy defect (highlighted as a yellow polygon).
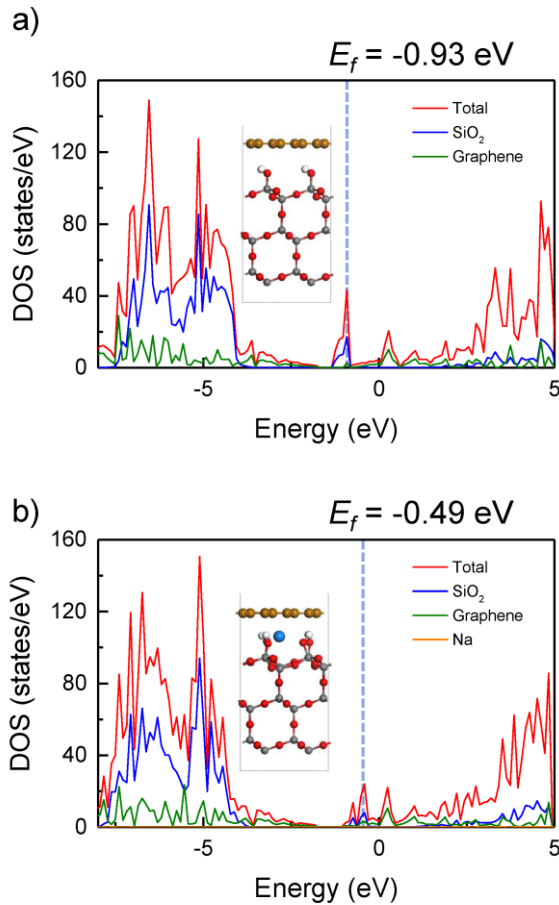
Figure 5.A.6 | The density of state (DOS) calculation result of the graphene-SiO$_2$ interface. (a), Computed DOS of supported graphene. Inserts are the atomic structures of graphene on SiO$_2$. **(b),** Computed DOS of the system with Na residing at graphene-SiO$_2$ interface. Insert the atomic structure of Na residing at graphene-SiO$_2$ interface.
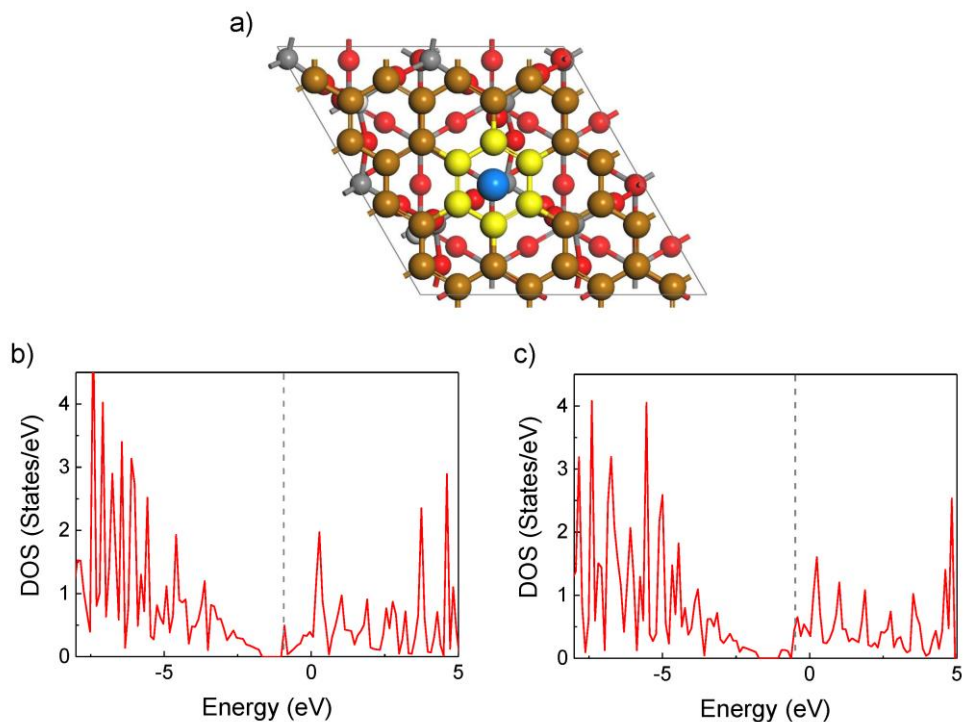
Figure 5.A.7 | The calculated PDOS of C atom around Na$^+$, **a,** The top view of supported graphene, where yellow C atoms were selected for the PDOS. **b,** The calculated PDOS without Na$^+$. **c,** The calculated PDOS with Na$^+$.

Summary

This thesis studies the hot carrier dynamics in photoexcited graphene, a critical optoelectronic process relevant for both fundamental physical studies and many practical applications of graphene. The aim of the thesis is first to shed light and further achieve affective control on hot carrier cooling processes in graphene [10–14]. This is because both fast and slow cooling dynamics of hot carriers can be useful, depending on the applications. For example, slow cooling provides long-lived hot carriers, which are beneficial for photocurrent generation in high-sensitive photodetectors. On the flip side, fast cooling leads to a fast photoresponse, which is essential for high speed and broadband modulation bandwidth optical modulator applications [18]. We use state-of-art ultrafast THz spectroscopies to explore the carrier dynamics in several unique graphene systems, to provide microscopic insights into the cooling mechanisms. In summary, the main results reported in this thesis are: i) we demonstrate that the electron-optical phonon interaction plays a dominant role as an efficient cooling pathway during hot-carrier cooling in high-quality graphene systems; ii) we show that solvent dielectric environment engineering can provide an effective approach to control the hot carrier lifetime in graphene; iii) By monitoring the photoconductivity of electrolyte-contacted graphene (supported by SiO_2), we report a kinetic ionic permeation process through the defects of graphene. We find that the size of the solvated cations critically governs the permeation kinetics and determines the doping magnitude induced by the interfacial cations.

The thesis starts with building up the basic theory for graphene and its electronic properties (massless Dirac Fermions, Fermi-Dirac distribution, and scattering mechanisms in graphene). We then review the hot carrier response in graphene following photoexcitation, and discuss the existing hot carrier heating and cooling models for photoexcited charge carriers. In chapter 2, we introduce THz spectroscopy and its working principle for probing the hot carrier dynamics in graphene. Notably, the semiclassical approach in analyzing the conduction discloses the relationship between photoconductivity and the electron temperature of graphene.

In chapter 3, we investigate the ultrafast carrier dynamics in high-quality suspended graphene. For that, we choose one type of high-quality graphene sample – suspended graphene single crystals, where "supercollision" cooling via acoustic phonon emissions is predicted inefficient due to the disorder density present in the sample. We can also exclude extrinsic substrate effects because single-crystal graphene is suspended. With OPTP and TA measurements, we observed a still fast cooling process with a cooling time $2 - 4$ ps. The dynamics observed from such a unique graphene system matches well with theoretical analyses based on efficient cooling in intrinsic high-quantity graphene via optical phonon emissions. A physics picture of the cooling through the combination of three physical processes is proposed to explain the fast cooling in high-quality graphene: i) optical phonon emission by electrons with energy > 0.16 eV above the chemical potential, ii) continuous re-thermalization of the electronic distribution, and iii) anharmonic coupling of optical phonons to acoustic phonons. The theoretical model revealed the importance of continuous re-thermalization via electron-electron scattering for hot-carrier cooling in high-quality graphene.

In chapter 4, we studied and achieved controlling the cooling dynamics in graphene by tuning its dielectric environments. Our results showed the hot-carrier cooling dynamics is tunable by varying the dielectric constant ϵ of dielectric solvents near graphene. When the environmental dielectric constant ϵ is below 20, we observed that the hot carrier cooling slows down with the dielectric increase. We rationalized our observation by the consequence of the suppression of electron-electron scattering due to the dielectric screening effect from solvents. Such suppression results in a direct cooling of nonthermalized hot carriers via electron-optical phonon collisions, and thus slower cooling dynamics. We also observed an inverse ϵ-dependence of cooling time when the ϵ is higher than 20. One scenario to explain such trends is that the interfacial ϵ is much lower than the bulk due to the molecules in polar solvents are more immobilized at interfaces.

In chapter 5 we have investigated the effect of ions, in particular, aqueous cations (Li^+, Na^+, K^+, and Ca^{2+}) in solution, on the hot-carrier dynamics in graphene supported on SiO_2. We found cations can lead to an upshift of the Fermi level (up to 200 meV) in graphene from initially hole-doping to the vicinity of Dirac point. This leads to a transition in hot-carrier response, i.e., photoconductivity of graphene from negative (for hole-doped graphene) to positive for (intrinsic graphene). Markedly, the kinetics and magnitude of this Fermi level shift correlate with the cation concentrations and hydrated ion sizes: the smaller the hydrated cation size, or the higher the ion concertation, the faster and larger the resultant Fermi level shift. Employed theoretical calculations, we attribute the kinetic cation-induced Fermi level shift to the consequence of cationic permeation through graphene lattice defects. The permeated cations locate between graphene and SiO_2 and electrostatically counteract the

substrate-induced hole-doping effect in graphene. Our findings provide a novel method to monitor the ionic dynamics at graphene interfaces in a contact-free manner, relevant for graphene and other 2D materials for applications in electrochemical energy storage.

All in all, our studies and findings provide basic understandings and tuning knobs for controlling hot carrier responses in graphene. Our results and discussions are of interest to academia and industry, where graphene has been intensely proposed as an ideal platform for next-generation optoelectronics and optical communication systems.

Samenvatting

Dit proefschrift bestudeert de hete ladingsdrager dynamica in foto-geëxciteerd grafeen, een kritisch opto-elektronisch proces dat relevant is voor zowel fundamentele fysische studies als praktische toepassingen van grafeen. Het doel van het proefschrift is ten eerste om licht te werpen op de afkoelingsprocessen van hete ladingsdragers in grafeen en deze verder te beheersen [10–14]. De reden hiervoor is dat zowel snelle als langzame afkoeling van hete ladingsdragers nuttig kan zijn, afhankelijk van de toepassingen. Langzame koeling zorgt voor langlevende hete dragers, die bijvoorbeeld gunstig zijn voor het genereren van fotostromen in hoog-gevoelige fotodetectoren. Aan de andere kant leidt snelle koeling tot een snelle fotorespons, essentieel voor optische modulatortoepassingen met hoge snelheid en modulatiebandbreedte [18]. We gebruiken state-of-art ultrasnelle THz spectroscopie om de drager dynamica te onderzoeken in verschillende unieke grafeen systemen, om microscopisch inzicht te verschaffen in de afkoelingsmechanismen. Samenvattend zijn de belangrijkste resultaten van dit proefschrift: i) we tonen aan dat de elektron-optische fononinteractie een dominante rol speelt als een efficiënte koelroute tijdens het koelen van warme ladingsdragers in grafeensystemen van hoge kwaliteit; ii) we tonen aan dat de engineering van de solvent-diëlektrische omgeving een effectieve benadering kan bieden om de levensduur van warme ladingsdragers in grafeen te controleren; iii) door het monitoren van de fotogeleidbaarheid van met elektrolyt gecontacteerd grafeen (ondersteund door SiO_2), rapporteren we een kinetisch ionisch permeatieproces door de defecten

van grafeen. We stellen vast dat de afmeting van de opgeloste kationen de permeatiekinetiek kritisch bepaalt en bepalend is voor de grootte van de dopering geïnduceerd door de interfaciale kationen.

Het proefschrift begint met het opbouwen van de basistheorie voor grafeen en zijn elektronische eigenschappen (massaloze Dirac Fermionen, Fermi-Dirac verdeling en verstrooiingsmechanismen in grafeen). Vervolgens bespreken we de reactie van hete dragers in grafeen na foto-excitatie, en bespreken we de bestaande modellen voor het opwarmen en afkoelen van hete dragers voor foto-exciterende ladingsdragers. In hoofdstuk 2 introduceren we THz spectroscopie en het werkingsprincipe ervan voor het onderzoeken van de dynamica van warme ladingsdragers in grafeen. Met name de semiklassieke benadering in het analyseren van de geleiding onthult de relatie tussen fotogeleidbaarheid en de elektronentemperatuur van grafeen.

In hoofdstuk 3 onderzoeken we de ultrasnelle ladingsdragerdynamica in gesuspendeerd grafeen van hoge kwaliteit. Daarvoor kiezen we een type grafeen van hoge kwaliteit - gesuspendeerde grafeen-enkelkristallen, waarbij „supercollision" koeling via akoestische fonon emissie inefficiënt is vanwege het gebrek aan defecten in het monster. We kunnen ook extrinsieke substraateffecten uitsluiten omdat het grafeen in één kristal is opgehangen. Met OPTP- en TA-metingen nemen we desondanks een nog steeds snel afkoelingsproces waar, met een koeltijd van $2 - 4$ ps. De waargenomen dynamiek van zo'n uniek grafeen systeem komt goed overeen met theoretische analyses gebaseerd op efficiënte koeling in intrinsiek grafeen via optische fononemissies. Een fysisch beeld van de afkoeling door de combinatie van drie fysische processen wordt voorgesteld om de snelle afkoeling in grafeen van hoge kwaliteit te verklaren: i) optische fonon emissie door elektronen met energie > 0.16 eV boven de

chemische potentiaal, ii) continue re-thermalisatie van de elektronische distributie, en iii) anharmonische koppeling van optische fononen aan akoestische fononen. Ons model onthult het belang van continue her-thermalisatie via elektron-elektron verstrooiing voor het koelen van hete ladingsdragers in hoogwaardig grafeen.

In hoofdstuk 4 bestudeerden we het beheersen van de koeldynamica in grafeen door het afstemmen van de diëlektrische omgevingen. Onze resultaten laten zien dat de koeling van de hete drager kan worden beinvloed door de diëlektrische constante ϵ van de diëlektrische oplosmiddelen in de buurt van grafeen te variëren. Wanneer de diëlektrische constante ϵ lager is dan 20, zien we dat de koeling van de warme drager vertraagt naarmate de diëlektrische constante toeneemt. We verklaren onze waarneming door de onderdrukking van elektron-elektronverstrooiing ten gevolge van het diëlektrische screeningseffect van oplosmiddelen met hogere diëlektrische functie. Dergelijke onderdrukking resulteert in een directe afkoeling van niet-thermische hete dragers via elektron-optische fonon botsingen, en dus een tragere afkoeldynamiek. We hebben ook een omgekeerde ϵ-afhankelijkheid van de koeltijd waargenomen wanneer de ϵ hoger is dan 20. Een scenario om deze trends te verklaren is dat de lokale ϵ veel lager is aan het oppervlak van het grafeen dan in de bulk, doordat de moleculen in polaire oplosmiddelen meer geïmmobiliseerd zijn aan de interfaces.

In hoofdstuk 5 hebben we het effect onderzocht van ionen, in het bijzonder waterige kationen (Li^+, Na^+, K^+, en Ca^{2+}) in oplossing, op de hot-carrier dynamica in grafeen ondersteund op SiO_2. We ontdekten dat kationen kunnen leiden tot een verschuiving van het Fermi-niveau (tot 200 meV) in grafeen van aanvankelijk hole-doping naar de buurt van het Dirac-punt. Dit leidt tot een

overgang in de hete-drager respons, d.w.z. de fotogeleidbaarheid van grafeen, van negatief (voor gat-gedoteerd grafeen) naar positief voor (intrinsiek grafeen). Opvallend is dat de kinetiek en de grootte van deze Fermi-niveauverschuiving correleren met de kationconcentraties en gehydrateerde ionengroottes: hoe kleiner de gehydrateerde kationengrootte, of hoe hoger de ion-concertatie, hoe sneller en groter de resulterende Fermi-niveauverschuiving. Met behulp van theoretische berekeningen schrijven wij de kinetische kation-geïnduceerde Fermi-niveauverschuiving toe aan het gevolg van kationische permeatie door grafeenrooster-defecten. De doorgelaten kationen bevinden zich tussen grafeen en SiO_2 en werken elektrostatisch het substraat-geïnduceerde gat-doping effect in grafeen tegen. Onze bevindingen bieden een nieuwe methode om de ionendynamiek bij grafeeninterfaces op een contactloze manier te monitoren, wat relevant is voor grafeen en andere 2D-materialen voor toepassingen in elektrochemische energieopslag.

Al met al leveren onze studies en bevindingen fundamenteel begrip, alsook praktische tips voor het controleren van hete ladingsdragerreacties in grafeen. Onze resultaten en discussies zijn van belang voor de academische wereld en de industrie, waar grafeen in toenemende mate toegepast wordt als platform voor de volgende generatie opto-elektronica en optische communicatiesystemen.

Bibliography

[1]   K. S. Novoselov, A. K. Geim, S. V. Morozov, D. Jiang, Y. Zhang, S. V. Dubonos, I. V. Grigorieva, and A. A. Firsov, *Electric Field Effect in Atomically Thin Carbon Films*, Science **306**, 666 (2004).

[2]   K. S. Novoselov, A. K. Geim, S. V. Morozov, D. Jiang, M. I. Katsnelson, I. V. Grigorieva, S. V. Dubonos, and A. A. Firsov, *Two-Dimensional Gas of Massless Dirac Fermions in Graphene*, Nature **438**, 197 (2005).

[3]   Y. Zhang, Y.-W. Tan, H. L. Stormer, and P. Kim, *Experimental Observation of the Quantum Hall Effect and Berry's Phase in Graphene*, Nature **438**, 201 (2005).

[4]   L. Banszerus, T. Sohier, A. Epping, F. Winkler, F. Libisch, F. Haupt, K. Watanabe, T. Taniguchi, K. Müller-Caspary, N. Marzari, F. Mauri, B. Beschoten, and C. Stampfer, *Extraordinary High Room-Temperature Carrier Mobility in Graphene-WSe$_2$ Heterostructures*, ArXiv190909523 Cond-Mat (2019).

[5]   Q. Bao, H. Zhang, Y. Wang, Z. Ni, Y. Yan, Z. X. Shen, K. P. Loh, and D. Y. Tang, *Atomic-Layer Graphene as a Saturable Absorber for Ultrafast Pulsed Lasers*, Adv. Funct. Mater. **19**, 3077 (2009).

[6]   F. Bonaccorso, Z. Sun, T. Hasan, and A. C. Ferrari, *Graphene Photonics and Optoelectronics*, Nat. Photonics **4**, 9 (2010).

[7]   F. H. L. Koppens, T. Mueller, P. Avouris, A. C. Ferrari, M. S. Vitiello, and M. Polini, *Photodetectors Based on Graphene, Other Two-Dimensional Materials and Hybrid Systems*, Nat. Nanotechnol. **9**, 10 (2014).

[8]   F. Xia, H. Wang, D. Xiao, M. Dubey, and A. Ramasubramaniam, *Two-Dimensional Material Nanophotonics*, Nat. Photonics **8**, 899 (2014).

[9]   S. Schuler, D. Schall, D. Neumaier, L. Dobusch, O. Bethge, B. Schwarz, M. Krall, and T. Mueller, *Controlled Generation of a p–n Junction in a Waveguide Integrated Graphene Photodetector*, Nano Lett. **16**, 7107 (2016).

[10] P. A. George, J. Strait, J. Dawlaty, S. Shivaraman, M. Chandrashekhar, F. Rana, and M. G. Spencer, *Ultrafast Optical-Pump Terahertz-Probe Spectroscopy of the Carrier Relaxation and Recombination Dynamics in Epitaxial Graphene*, Nano Lett. **8**, 4248 (2008).

[11] M. Breusing, S. Kuehn, T. Winzer, E. Malić, F. Milde, N. Severin, J. P. Rabe, C. Ropers, A. Knorr, and T. Elsaesser, *Ultrafast Nonequilibrium*

Carrier Dynamics in a Single Graphene Layer, Phys. Rev. B **83**, 153410 (2011).

[12] K. J. Tielrooij, J. C. W. Song, S. A. Jensen, A. Centeno, A. Pesquera, A. Zurutuza Elorza, M. Bonn, L. S. Levitov, and F. H. L. Koppens, *Photoexcitation Cascade and Multiple Hot-Carrier Generation in Graphene*, Nat. Phys. **9**, 248 (2013).

[13] D. Brida, A. Tomadin, C. Manzoni, Y. J. Kim, A. Lombardo, S. Milana, R. R. Nair, K. S. Novoselov, A. C. Ferrari, G. Cerullo, and M. Polini, *Ultrafast Collinear Scattering and Carrier Multiplication in Graphene*, Nat. Commun. **4**, 1 (2013).

[14] I. Gierz, J. C. Petersen, M. Mitrano, C. Cacho, I. C. E. Turcu, E. Springate, A. Stöhr, A. Köhler, U. Starke, and A. Cavalleri, *Snapshots of Non-Equilibrium Dirac Carrier Distributions in Graphene*, Nat. Mater. **12**, 12 (2013).

[15] C. H. Lui, K. F. Mak, J. Shan, and T. F. Heinz, *Ultrafast Photoluminescence from Graphene*, Phys. Rev. Lett. **105**, 127404 (2010).

[16] M. W. Graham, S.-F. Shi, D. C. Ralph, J. Park, and P. L. McEuen, *Photocurrent Measurements of Supercollision Cooling in Graphene*, Nat. Phys. **9**, 103 (2013).

[17] K.-J. Tielrooij, N. C. H. Hesp, A. Principi, M. B. Lundeberg, E. A. A. Pogna, L. Banszerus, Z. Mics, M. Massicotte, P. Schmidt, D. Davydovskaya, D. G. Purdie, I. Goykhman, G. Soavi, A. Lombardo, K. Watanabe, T. Taniguchi, M. Bonn, D. Turchinovich, C. Stampfer, A. C. Ferrari, G. Cerullo, M. Polini, and F. H. L. Koppens, *Out-of-Plane Heat Transfer in van Der Waals Stacks through Electron–Hyperbolic Phonon Coupling*, Nat. Nanotechnol. **13**, 41 (2018).

[18] M. Liu, X. Yin, E. Ulin-Avila, B. Geng, T. Zentgraf, L. Ju, F. Wang, and X. Zhang, *A Graphene-Based Broadband Optical Modulator*, Nature **474**, 7349 (2011).

[19] A. K. Geim and K. S. Novoselov, *The Rise of Graphene*, Nat. Mater. **6**, 183 (2007).

[20] P. R. Wallace, *The Band Theory of Graphite*, Phys. Rev. **71**, 622 (1947).

[21] J. W. McClure, *Diamagnetism of Graphite*, Phys. Rev. **104**, 666 (1956).

[22] J. C. Slonczewski and P. R. Weiss, *Band Structure of Graphite*, Phys. Rev. **109**, 272 (1958).

[23] E. Fradkin, *Critical Behavior of Disordered Degenerate Semiconductors. II. Spectrum and Transport Properties in Mean-Field Theory*, Phys. Rev. B **33**, 3263 (1986).

[24] K. S. Novoselov, A. Mishchenko, A. Carvalho, and A. H. C. Neto, *2D Materials and van Der Waals Heterostructures*, Science **353**, (2016).

[25] R. R. Nair, P. Blake, A. N. Grigorenko, K. S. Novoselov, T. J. Booth, T. Stauber, N. M. R. Peres, and A. K. Geim, *Fine Structure Constant Defines Visual Transparency of Graphene*, Science **320**, 1308 (2008).

[26] K. S. Novoselov, Z. Jiang, Y. Zhang, S. V. Morozov, H. L. Stormer, U. Zeitler, J. C. Maan, G. S. Boebinger, P. Kim, and A. K. Geim, *Room-Temperature Quantum Hall Effect in Graphene*, Science **315**, 1379 (2007).

[27] A. H. Castro Neto, F. Guinea, N. M. R. Peres, K. S. Novoselov, and A. K. Geim, *The Electronic Properties of Graphene*, Rev. Mod. Phys. **81**, 109 (2009).

[28] N. M. R. Peres, *Colloquium: The Transport Properties of Graphene: An Introduction*, Rev. Mod. Phys. **82**, 2673 (2010).

[29] S. Das Sarma, S. Adam, E. H. Hwang, and E. Rossi, *Electronic Transport in Two-Dimensional Graphene*, Rev. Mod. Phys. **83**, 407 (2011).

[30] Y. Zhang, Electronic Transport in Graphene, 2006.

[31] H. Jussila, H. Yang, N. Granqvist, and Z. Sun, *Surface Plasmon Resonance for Characterization of Large-Area Atomic-Layer Graphene Film*, Optica **3**, 151 (2016).

[32] D. R. Cooper, B. D'Anjou, N. Ghattamaneni, B. Harack, M. Hilke, A. Horth, N. Majlis, M. Massicotte, L. Vandsburger, E. Whiteway, and V. Yu, *Experimental Review of Graphene*, ISRN Condens. Matter Phys. **2012**, e501686 (2012).

[33] C. Kittel, *Introduction to Solid State Physics* (Wiley, 2004).

[34] A. W, N. W. Ashcroft, N. D. Mermin, and N. D. Mermin, *Solid State Physics* (Holt, Rinehart and Winston, 1976).

[35] D. K. Ferry, *Semi-Classical Boltzmann Transport Theory in Semiconductors*, in *Physics of Nonlinear Transport in Semiconductors*, edited by D. K. Ferry, J. R. Barker, and C. Jacoboni (Springer US, Boston, MA, 1980), pp. 117–125.

[36] D. Shoenberg, *Magnetic Oscillations in Metals* (Cambridge University Press, 2009).

[37] P. Avouris and M. Freitag, *Graphene Photonics, Plasmonics, and Optoelectronics*, IEEE J. Sel. Top. Quantum Electron. **20**, 72 (2014).

[38] E. H. Hwang, S. Adam, and S. D. Sarma, *Carrier Transport in Two-Dimensional Graphene Layers*, Phys. Rev. Lett. **98**, 186806 (2007).

[39] S. Adam, E. H. Hwang, V. M. Galitski, and S. D. Sarma, *A Self-Consistent Theory for Graphene Transport*, Proc. Natl. Acad. Sci. **104**, 18392 (2007).

[40] C. Jang, S. Adam, J.-H. Chen, E. D. Williams, S. Das Sarma, and M. S. Fuhrer, *Tuning the Effective Fine Structure Constant in Graphene: Opposing Effects of Dielectric Screening on Short- and Long-Range Potential Scattering*, Phys. Rev. Lett. **101**, 146805 (2008).

[41] T. Stauber, N. M. R. Peres, and F. Guinea, *Electronic Transport in Graphene: A Semiclassical Approach Including Midgap States*, Phys. Rev. B **76**, 205423 (2007).

[42] F. T. Vasko and V. Ryzhii, *Voltage and Temperature Dependencies of Conductivity in Gated Graphene*, Phys. Rev. B **76**, 233404 (2007).

[43] E. H. Hwang and S. Das Sarma, *Acoustic Phonon Scattering Limited Carrier Mobility in Two-Dimensional Extrinsic Graphene*, Phys. Rev. B **77**, 115449 (2008).

[44] A. Principi, M. Carrega, M. B. Lundeberg, A. Woessner, F. H. L. Koppens, G. Vignale, and M. Polini, *Plasmon Losses Due to Electron-Phonon Scattering: The Case of Graphene Encapsulated in Hexagonal Boron Nitride*, Phys. Rev. B **90**, 165408 (2014).

[45] J. Bardeen and W. Shockley, *Deformation Potentials and Mobilities in Non-Polar Crystals*, Phys. Rev. **80**, 72 (1950).

[46] J.-H. Chen, C. Jang, S. Xiao, M. Ishigami, and M. S. Fuhrer, *Intrinsic and Extrinsic Performance Limits of Graphene Devices on SiO_2*, Nat. Nanotechnol. **3**, 4 (2008).

[47] L. Wang, I. Meric, P. Y. Huang, Q. Gao, Y. Gao, H. Tran, T. Taniguchi, K. Watanabe, L. M. Campos, D. A. Muller, J. Guo, P. Kim, J. Hone, K. L. Shepard, and C. R. Dean, *One-Dimensional Electrical Contact to a Two-Dimensional Material*, Science **342**, 614 (2013).

[48] M. I. Katsnelson, *Zitterbewegung, Chirality, and Minimal Conductivity in Graphene*, Eur. Phys. J. B - Condens. Matter Complex Syst. **51**, 157 (2006).

[49] J. Tworzydło, B. Trauzettel, M. Titov, A. Rycerz, and C. W. J. Beenakker, *Sub-Poissonian Shot Noise in Graphene*, Phys. Rev. Lett. **96**, 246802 (2006).

[50] M. Gibertini, A. Tomadin, F. Guinea, M. I. Katsnelson, and M. Polini, *Electron-Hole Puddles in the Absence of Charged Impurities*, Phys. Rev. B **85**, 201405 (2012).

[51] M. Bernardi, M. Palummo, and J. C. Grossman, *Extraordinary Sunlight Absorption and One Nanometer Thick Photovoltaics Using Two-Dimensional Monolayer Materials*, Nano Lett. **13**, 3664 (2013).

[52] L. Britnell, R. V. Gorbachev, R. Jalil, B. D. Belle, F. Schedin, A. Mishchenko, T. Georgiou, M. I. Katsnelson, L. Eaves, S. V. Morozov, N. M. R. Peres, J. Leist, A. K. Geim, K. S. Novoselov, and L. A. Ponomarenko, *Field-Effect Tunneling Transistor Based on Vertical Graphene Heterostructures*, Science **335**, 947 (2012).

[53] Y. M. Zuev, W. Chang, and P. Kim, *Thermoelectric and Magnetothermoelectric Transport Measurements of Graphene*, Phys. Rev. Lett. **102**, 096807 (2009).

[54] P. Wei, W. Bao, Y. Pu, C. N. Lau, and J. Shi, *Anomalous Thermoelectric Transport of Dirac Particles in Graphene*, Phys. Rev. Lett. **102**, 166808 (2009).

[55] A. Mai, M. Lisker, M. Lukosius, and G. Lupina, *(Invited) Large Scale Graphene Integration for Silicon Technologies*, ECS Trans. **79**, 3 (2017).

[56] S. Rahimi, L. Tao, Sk. F. Chowdhury, S. Park, A. Jouvray, S. Buttress, N. Rupesinghe, K. Teo, and D. Akinwande, *Toward 300 Mm Wafer-Scalable High-Performance Polycrystalline Chemical Vapor Deposited Graphene Transistors*, ACS Nano **8**, 10471 (2014).

[57] D. Akinwande, C. Huyghebaert, C.-H. Wang, M. I. Serna, S. Goossens, L.-J. Li, H.-S. P. Wong, and F. H. L. Koppens, *Graphene and Two-Dimensional Materials for Silicon Technology*, Nature **573**, 7775 (2019).

[58] N. M. Gabor, J. C. W. Song, Q. Ma, N. L. Nair, T. Taychatanapat, K. Watanabe, T. Taniguchi, L. S. Levitov, and P. Jarillo-Herrero, *Hot Carrier–Assisted Intrinsic Photoresponse in Graphene*, Science **334**, 648 (2011).

[59] J. C. W. Song, M. S. Rudner, C. M. Marcus, and L. S. Levitov, *Hot Carrier Transport and Photocurrent Response in Graphene*, Nano Lett. **11**, 4688 (2011).

[60] J. Renard, M. Studer, and J. A. Folk, *Origins of Nonlocality Near the Neutrality Point in Graphene*, Phys. Rev. Lett. **112**, 116601 (2014).

[61] J. Yan, M.-H. Kim, J. A. Elle, A. B. Sushkov, G. S. Jenkins, H. M. Milchberg, M. S. Fuhrer, and H. D. Drew, *Dual-Gated Bilayer Graphene Hot-Electron Bolometer*, Nat. Nanotechnol. **7**, 7 (2012).

[62] P. K. Herring, A. L. Hsu, N. M. Gabor, Y. C. Shin, J. Kong, T. Palacios, and P. Jarillo-Herrero, *Photoresponse of an Electrically Tunable Ambipolar Graphene Infrared Thermocouple*, Nano Lett. **14**, 901 (2014).

[63] J. C. W. Song and L. S. Levitov, *Energy-Driven Drag at Charge Neutrality in Graphene*, Phys. Rev. Lett. **109**, 236602 (2012).

[64] D. Sun, G. Aivazian, A. M. Jones, J. S. Ross, W. Yao, D. Cobden, and X. Xu, *Ultrafast Hot-Carrier-Dominated Photocurrent in Graphene*, Nat. Nanotechnol. **7**, 2 (2012).

[65] V. Sorianello, M. Midrio, G. Contestabile, I. Asselberghs, J. Van Campenhout, C. Huyghebaert, I. Goykhman, A. K. Ott, A. C. Ferrari, and M. Romagnoli, *Graphene–Silicon Phase Modulators with Gigahertz Bandwidth*, Nat. Photonics **12**, 1 (2018).

[66] J. C. Johannsen, S. Ulstrup, F. Cilento, A. Crepaldi, M. Zacchigna, C. Cacho, I. C. E. Turcu, E. Springate, F. Fromm, C. Raidel, T. Seyller, F. Parmigiani, M. Grioni, and P. Hofmann, *Direct View of Hot Carrier Dynamics in Graphene*, Phys. Rev. Lett. **111**, 027403 (2013).

[67] J. C. W. Song and L. S. Levitov, *Energy Flows in Graphene: Hot Carrier Dynamics and Cooling*, J. Phys. Condens. Matter **27**, 164201 (2015).

[68] T. Winzer, A. Knorr, and E. Malic, *Carrier Multiplication in Graphene*, Nano Lett. **10**, 4839 (2010).

[69] T. Kampfrath, L. Perfetti, F. Schapper, C. Frischkorn, and M. Wolf, *Strongly Coupled Optical Phonons in the Ultrafast Dynamics of the Electronic Energy and Current Relaxation in Graphite*, Phys. Rev. Lett. **95**, 187403 (2005).

[70] F. Rana, *Electron-Hole Generation and Recombination Rates for Coulomb Scattering in Graphene*, Phys. Rev. B **76**, 155431 (2007).

[71] M. Breusing, C. Ropers, and T. Elsaesser, *Ultrafast Carrier Dynamics in Graphite*, Phys. Rev. Lett. **102**, 086809 (2009).

[72] R. Kim, V. Perebeinos, and P. Avouris, *Relaxation of Optically Excited Carriers in Graphene*, Phys. Rev. B **84**, 075449 (2011).

[73] S. Winnerl, M. Orlita, P. Plochocka, P. Kossacki, M. Potemski, T. Winzer, E. Malic, A. Knorr, M. Sprinkle, C. Berger, W. A. de Heer, H. Schneider, and M. Helm, *Carrier Relaxation in Epitaxial Graphene Photoexcited Near the Dirac Point*, Phys. Rev. Lett. **107**, 237401 (2011).

[74] S. Butscher, F. Milde, M. Hirtschulz, E. Malić, and A. Knorr, *Hot Electron Relaxation and Phonon Dynamics in Graphene*, Appl. Phys. Lett. **91**, 203103 (2007).

[75] M. W. Graham, S.-F. Shi, Z. Wang, D. C. Ralph, J. Park, and P. L. McEuen, *Transient Absorption and Photocurrent Microscopy Show That Hot Electron Supercollisions Describe the Rate-Limiting Relaxation Step in Graphene*, Nano Lett. **13**, 5497 (2013).

[76] J. C. W. Song, K. J. Tielrooij, F. H. L. Koppens, and L. S. Levitov, *Photoexcited Carrier Dynamics and Impact-Excitation Cascade in Graphene*, Phys. Rev. B **87**, 155429 (2013).

[77] T. Winzer and E. Malić, *Impact of Auger Processes on Carrier Dynamics in Graphene*, Phys. Rev. B **85**, 241404 (2012).

[78] S. Wu, L. Wang, Y. Lai, W.-Y. Shan, G. Aivazian, X. Zhang, T. Taniguchi, K. Watanabe, D. Xiao, C. Dean, J. Hone, Z. Li, and X. Xu, *Multiple Hot-Carrier Collection in Photo-Excited Graphene Moiré Superlattices*, Sci. Adv. **2**, e1600002 (2016).

[79] Q. Ma, C. H. Lui, J. C. W. Song, Y. Lin, J. F. Kong, Y. Cao, T. H. Dinh, N. L. Nair, W. Fang, K. Watanabe, T. Taniguchi, S.-Y. Xu, J. Kong, T. Palacios, N. Gedik, N. M. Gabor, and P. Jarillo-Herrero, *Giant Intrinsic Photoresponse in Pristine Graphene*, Nat. Nanotechnol. **14**, 145 (2019).

[80] A. Tomadin, S. M. Hornett, H. I. Wang, E. M. Alexeev, A. Candini, C. Coletti, D. Turchinovich, M. Kläui, M. Bonn, F. H. L. Koppens, E. Hendry, M. Polini, and K.-J. Tielrooij, *The Ultrafast Dynamics and Conductivity of Photoexcited Graphene at Different Fermi Energies*, Sci. Adv. **4**, eaar5313 (2018).

[81] W.-K. Tse and S. Das Sarma, *Energy Relaxation of Hot Dirac Fermions in Graphene*, Phys. Rev. B **79**, 235406 (2009).

[82] S. A. Jensen, Z. Mics, I. Ivanov, H. S. Varol, D. Turchinovich, F. H. L. Koppens, M. Bonn, and K. J. Tielrooij, *Competing Ultrafast Energy Relaxation Pathways in Photoexcited Graphene*, Nano Lett. **14**, 5839 (2014).

[83] E. Pop, V. Varshney, and A. K. Roy, *Thermal Properties of Graphene: Fundamentals and Applications*, MRS Bull. **37**, 1273 (2012).

[84] N. Mounet and N. Marzari, *First-Principles Determination of the Structural, Vibrational and Thermodynamic Properties of Diamond, Graphite, and Derivatives*, Phys. Rev. B **71**, 205214 (2005).

[85] R. Bistritzer and A. H. MacDonald, *Electronic Cooling in Graphene*, Phys. Rev. Lett. **102**, 206410 (2009).

[86] J. C. W. Song, M. Y. Reizer, and L. S. Levitov, *Disorder-Assisted Electron-Phonon Scattering and Cooling Pathways in Graphene*, Phys. Rev. Lett. **109**, 106602 (2012).

[87] H. Wang, J. H. Strait, P. A. George, S. Shivaraman, V. B. Shields, M. Chandrashekhar, J. Hwang, F. Rana, M. G. Spencer, C. S. Ruiz-Vargas, and J. Park, *Ultrafast Relaxation Dynamics of Hot Optical Phonons in Graphene*, Appl. Phys. Lett. **96**, 081917 (2010).

[88] A. K. Geim and I. V. Grigorieva, *Van Der Waals Heterostructures*, Nature **499**, 7459 (2013).

[89] S.-F. Shi, T.-T. Tang, B. Zeng, L. Ju, Q. Zhou, A. Zettl, and F. Wang, *Controlling Graphene Ultrafast Hot Carrier Response from Metal-like to Semiconductor-like by Electrostatic Gating*, Nano Lett. **14**, 1578 (2014).

[90] H. A. Hafez, S. Kovalev, K.-J. Tielrooij, M. Bonn, M. Gensch, and D. Turchinovich, *Terahertz Nonlinear Optics of Graphene: From Saturable Absorption to High-Harmonics Generation*, Adv. Opt. Mater. **8**, 1900771 (2020).

[91] I. Ivanov, M. Bonn, Z. Mics, and D. Turchinovich, *Perspective on Terahertz Spectroscopy of Graphene*, EPL Europhys. Lett. **111**, 67001 (2015).

[92] A. J. Frenzel, C. H. Lui, Y. C. Shin, J. Kong, and N. Gedik, *Semiconducting-to-Metallic Photoconductivity Crossover and Temperature-Dependent Drude Weight in Graphene*, Phys. Rev. Lett. **113**, 056602 (2014).

[93] A. C. Betz, S. H. Jhang, E. Pallecchi, R. Ferreira, G. Fève, J.-M. Berroir, and B. Plaçais, *Supercollision Cooling in Undoped Graphene*, Nat. Phys. **9**, nphys2494 (2012).

[94] S. S. Kubakaddi, *Interaction of Massless Dirac Electrons with Acoustic Phonons in Graphene at Low Temperatures*, Phys. Rev. B **79**, 075417 (2009).

[95] E. Malic, T. Winzer, E. Bobkin, and A. Knorr, *Microscopic Theory of Absorption and Ultrafast Many-Particle Kinetics in Graphene*, Phys. Rev. B **84**, 205406 (2011).

[96] F. R. Eder, J. Kotakoski, U. Kaiser, and J. C. Meyer, *A Journey from Order to Disorder — Atom by Atom Transformation from Graphene to a 2D Carbon Glass*, Sci. Rep. **4**, 1 (2014).

[97] T. Low, V. Perebeinos, R. Kim, M. Freitag, and P. Avouris, *Cooling of Photoexcited Carriers in Graphene by Internal and Substrate Phonons*, Phys. Rev. B **86**, 045413 (2012).

[98] A. S. Price, S. M. Hornett, A. V. Shytov, E. Hendry, and D. W. Horsell, *Nonlinear Resistivity and Heat Dissipation in Monolayer Graphene*, Phys. Rev. B **85**, 161411 (2012).

[99] S. Fratini and F. Guinea, *Substrate-Limited Electron Dynamics in Graphene*, Phys. Rev. B **77**, 195415 (2008).

[100] W. Yang, S. Berthou, X. Lu, Q. Wilmart, A. Denis, M. Rosticher, T. Taniguchi, K. Watanabe, G. Fève, J.-M. Berroir, G. Zhang, C. Voisin, E.

Baudin, and B. Plaçais, *A Graphene Zener–Klein Transistor Cooled by a Hyperbolic Substrate*, Nat. Nanotechnol. 1 (2017).

[101]   M. i Katsnelson and A. k Geim, *Electron Scattering on Microscopic Corrugations in Graphene*, Philos. Trans. R. Soc. Math. Phys. Eng. Sci. **366**, 195 (2008).

[102]   A. L. Vázquez de Parga, F. Calleja, B. Borca, M. C. G. Passeggi, J. J. Hinarejos, F. Guinea, and R. Miranda, *Periodically Rippled Graphene: Growth and Spatially Resolved Electronic Structure*, Phys. Rev. Lett. **100**, 056807 (2008).

[103]   C. R. Dean, A. F. Young, I. Meric, C. Lee, L. Wang, S. Sorgenfrei, K. Watanabe, T. Taniguchi, P. Kim, K. L. Shepard, and J. Hone, *Boron Nitride Substrates for High-Quality Graphene Electronics*, Nat. Nanotechnol. **5**, 722 (2010).

[104]   L. Britnell, R. M. Ribeiro, A. Eckmann, R. Jalil, B. D. Belle, A. Mishchenko, Y.-J. Kim, R. V. Gorbachev, T. Georgiou, S. V. Morozov, A. N. Grigorenko, A. K. Geim, C. Casiraghi, A. H. C. Neto, and K. S. Novoselov, *Strong Light-Matter Interactions in Heterostructures of Atomically Thin Films*, Science **340**, 1311 (2013).

[105]   A. Principi, M. B. Lundeberg, N. C. H. Hesp, K.-J. Tielrooij, F. H. L. Koppens, and M. Polini, *Super-Planckian Electron Cooling in a van Der Waals Stack*, Phys. Rev. Lett. **118**, 126804 (2017).

[106]   J. D. Caldwell, A. V. Kretinin, Y. Chen, V. Giannini, M. M. Fogler, Y. Francescato, C. T. Ellis, J. G. Tischler, C. R. Woods, A. J. Giles, M. Hong, K. Watanabe, T. Taniguchi, S. A. Maier, and K. S. Novoselov, *Sub-Diffractional Volume-Confined Polaritons in the Natural Hyperbolic Material Hexagonal Boron Nitride*, Nat. Commun. **5**, 1 (2014).

[107]   P. Li, M. Lewin, A. V. Kretinin, J. D. Caldwell, K. S. Novoselov, T. Taniguchi, K. Watanabe, F. Gaussmann, and T. Taubner, *Hyperbolic Phonon-Polaritons in Boron Nitride for near-Field Optical Imaging and Focusing*, Nat. Commun. **6**, 1 (2015).

[108]   J. M. Hamm, A. F. Page, J. Bravo-Abad, F. J. Garcia-Vidal, and O. Hess, *Nonequilibrium Plasmon Emission Drives Ultrafast Carrier Relaxation Dynamics in Photoexcited Graphene*, Phys. Rev. B **93**, 041408 (2016).

[109]   F. Rana, J. H. Strait, H. Wang, and C. Manolatou, *Ultrafast Carrier Recombination and Generation Rates for Plasmon Emission and Absorption in Graphene*, Phys. Rev. B **84**, 045437 (2011).

[110]   L. Kim, S. Kim, P. K. Jha, V. W. Brar, and H. A. Atwater, *Mid-Infrared Radiative Emission from Bright Hot Plasmons in Graphene*, ArXiv200111052 Cond-Mat (2020).

[111]   C. Sirtori, *Applied Physics: Bridge for the Terahertz Gap*, Nature **417**, 132 (2002).

[112]   Ch. Fattinger and D. Grischkowsky, *Terahertz Beams*, Appl. Phys. Lett. **54**, 490 (1989).

[113]   M. van Exter, Ch. Fattinger, and D. Grischkowsky, *High-brightness Terahertz Beams Characterized with an Ultrafast Detector*, Appl. Phys. Lett. **55**, 337 (1989).

[114]   X. -C. Zhang, Y. Jin, and X. F. Ma, *Coherent Measurement of THz Optical Rectification from Electro-optic Crystals*, Appl. Phys. Lett. **61**, 2764 (1992).

[115]   R. W. Boyd, *Nonlinear Optics* (Elsevier, 2008).

[116]   J. B. Baxter and G. W. Guglietta, *Terahertz Spectroscopy*, Anal. Chem. **83**, 4342 (2011).

[117]   I. van de Beld, Ultrafast Terahertz Spectroscopy on Photoexcitations in Nanostructured Semiconductors, Delft University of Technology, 2011.

[118]   R. Ulbricht, E. Hendry, J. Shan, T. F. Heinz, and M. Bonn, *Carrier Dynamics in Semiconductors Studied with Time-Resolved Terahertz Spectroscopy*, Rev. Mod. Phys. **83**, 543 (2011).

[119]   E. Hecht, *Optics* (Pearson Education, Incorporated, 2017).

[120]   D. Gonçalves and E. A. Irene, *Fundamentals and Applications of Spectroscopic Ellipsometry*, Quím. Nova **25**, 794 (2002).

[121]   D. J. Griffiths, *Introduction to Electrodynamics* (Prentice Hall, 1999).

[122]   W. C. Elmore, W. C. Elmore, and M. A. Heald, *Physics of Waves* (Courier Corporation, 1985).

[123]   P. C. M. Planken, H.-K. Nienhuys, H. J. Bakker, and T. Wenckebach, *Measurement and Calculation of the Orientation Dependence of Terahertz Pulse Detection in ZnTe*, JOSA B **18**, 313 (2001).

[124]   C. F. Klingshirn, *Semiconductor Optics* (Springer, Berlin ; New York, 2005).

[125]   J. E. Murphy, M. C. Beard, and A. J. Nozik, *Time-Resolved Photoconductivity of PbSe Nanocrystal Arrays*, J. Phys. Chem. B **110**, 25455 (2006).

[126]   A. Tomadin, D. Brida, G. Cerullo, A. C. Ferrari, and M. Polini, *Nonequilibrium Dynamics of Photoexcited Electrons in Graphene: Collinear Scattering, Auger Processes, and the Impact of Screening*, Phys. Rev. B **88**, 035430 (2013).

[127]   Y. Yu, F. Yang, X. F. Lu, Y. J. Yan, Y.-H. Cho, L. Ma, X. Niu, S. Kim, Y.-W. Son, D. Feng, S. Li, S.-W. Cheong, X. H. Chen, and Y. Zhang, *Gate-Tunable Phase Transitions in Thin Flakes of 1T-TaS$_2$*, Nat. Nanotechnol. **10**, 270 (2015).

[128]   F. Xia, T. Mueller, Y. Lin, A. Valdes-Garcia, and P. Avouris, *Ultrafast Graphene Photodetector*, Nat. Nanotechnol. **4**, 12 (2009).

[129]   S. Castilla, B. Terres, M. Autore, L. Viti, J. Li, A. Nikitin, I. Vangelidis, K. Watanabe, T. Taniguchi, E. Lidorikis, M. S. Vitiello, R. Hillenbrand, K.-J. Tielrooij, and F. H. L. Koppens, *Fast and Sensitive Terahertz Detection Using an Antenna-Integrated Graphene Pn-Junction*, Nano Lett. (2019).

[130]   D. A. Bandurin, D. Svintsov, I. Gayduchenko, S. G. Xu, A. Principi, M. Moskotin, I. Tretyakov, D. Yagodkin, S. Zhukov, T. Taniguchi, K. Watanabe, I. V. Grigorieva, M. Polini, G. N. Goltsman, A. K. Geim, and G. Fedorov, *Resonant Terahertz Detection Using Graphene Plasmons*, Nat. Commun. **9**, 1 (2018).

[131]   L. Viti, D. G. Purdie, A. Lombardo, A. C. Ferrari, and M. S. Vitiello, *HBN-Encapsulated, Graphene-Based, Room-Temperature Terahertz Receivers, with High Speed and Low Noise*, Nano Lett. **20**, 3169 (2020).

[132]   M. Romagnoli, V. Sorianello, M. Midrio, F. H. L. Koppens, C. Huyghebaert, D. Neumaier, P. Galli, W. Templ, A. D'Errico, and A. C. Ferrari, *Graphene-Based Integrated Photonics for next-Generation Datacom and Telecom*, Nat. Rev. Mater. **3**, 392 (2018).

[133]   J. E. Muench, A. Ruocco, M. A. Giambra, V. Miseikis, D. Zhang, J. Wang, H. F. Y. Watson, G. C. Park, S. Akhavan, V. Sorianello, M. Midrio, A. Tomadin, C. Coletti, M. Romagnoli, A. C. Ferrari, and I. Goykhman, *Waveguide-Integrated, Plasmonic Enhanced Graphene Photodetectors*, Nano Lett. **19**, 7632 (2019).

[134]   H. A. Hafez, S. Kovalev, J.-C. Deinert, Z. Mics, B. Green, N. Awari, M. Chen, S. Germanskiy, U. Lehnert, J. Teichert, Z. Wang, K.-J. Tielrooij, Z. Liu, Z. Chen, A. Narita, K. Müllen, M. Bonn, M. Gensch, and D. Turchinovich, *Extremely Efficient Terahertz High-Harmonic Generation in Graphene by Hot Dirac Fermions*, Nature **561**, 507 (2018).

[135]   G. Soavi, G. Wang, H. Rostami, D. G. Purdie, D. De Fazio, T. Ma, B. Luo, J. Wang, A. K. Ott, D. Yoon, S. A. Bourelle, J. E. Muench, I. Goykhman, S. Dal Conte, M. Celebrano, A. Tomadin, M. Polini, G. Cerullo, and A. C. Ferrari, *Broadband, Electrically Tunable Third-Harmonic Generation in Graphene*, Nat. Nanotechnol. **13**, 7 (2018).

[136]   G. Soavi, G. Wang, H. Rostami, A. Tomadin, O. Balci, I. Paradisanos, E. A. A. Pogna, G. Cerullo, E. Lidorikis, M. Polini, and A. C. Ferrari, *Hot Electrons Modulation of Third-Harmonic Generation in Graphene*, ACS Photonics **6**, 2841 (2019).

[137]   J.-C. Deinert, D. Alcaraz Iranzo, R. Pérez, X. Jia, H. A. Hafez, I. Ilyakov, N. Awari, M. Chen, M. Bawatna, A. N. Ponomaryov, S. Germanskiy, M. Bonn, F. H. L. Koppens, D. Turchinovich, M. Gensch, S. Kovalev, and K.-J. Tielrooij, *Grating-Graphene Metamaterial as a Platform for Terahertz Nonlinear Photonics*, ACS Nano (2020).

[138]   K.-J. Tielrooij, L. Piatkowski, M. Massicotte, A. Woessner, Q. Ma, Y. Lee, K. S. Myhro, C. N. Lau, P. Jarillo-Herrero, N. F. van Hulst, and F. H. L. Koppens, *Generation of Photovoltage in Graphene on a Femtosecond Time Scale through Efficient Carrier Heating*, Nat. Nanotechnol. **10**, 437 (2015).

[139]   P. J. Hale, S. M. Hornett, J. Moger, D. W. Horsell, and E. Hendry, *Hot Phonon Decay in Supported and Suspended Exfoliated Graphene*, Phys. Rev. B **83**, 121404 (2011).

[140]   M. T. Mihnev, F. Kadi, C. J. Divin, T. Winzer, S. Lee, C.-H. Liu, Z. Zhong, C. Berger, W. A. de Heer, E. Malic, A. Knorr, and T. B. Norris, *Microscopic Origins of the Terahertz Carrier Relaxation and Cooling Dynamics in Graphene*, Nat. Commun. **7**, 11617 (2016).

[141]   A. C. Betz, F. Vialla, D. Brunel, C. Voisin, M. Picher, A. Cavanna, A. Madouri, G. Fève, J.-M. Berroir, B. Plaçais, and E. Pallecchi, *Hot Electron Cooling by Acoustic Phonons in Graphene*, Phys. Rev. Lett. **109**, 056805 (2012).

[142]   T. V. Alencar, M. G. Silva, L. M. Malard, and A. M. de Paula, *Defect-Induced Supercollision Cooling of Photoexcited Carriers in Graphene*, Nano Lett. **14**, 5621 (2014).

[143]   J. E. Lee, G. Ahn, J. Shim, Y. S. Lee, and S. Ryu, *Optical Separation of Mechanical Strain from Charge Doping in Graphene*, Nat. Commun. **3**, 1 (2012).

[144]   J. A. Robinson, M. Wetherington, J. L. Tedesco, P. M. Campbell, X. Weng, J. Stitt, M. A. Fanton, E. Frantz, D. Snyder, B. L. VanMil, G. G.

Jernigan, R. L. Myers-Ward, C. R. Eddy, and D. K. Gaskill, *Correlating Raman Spectral Signatures with Carrier Mobility in Epitaxial Graphene: A Guide to Achieving High Mobility on the Wafer Scale*, Nano Lett. **9**, 2873 (2009).

[145]   J. Zhang, L. Lin, L. Sun, Y. Huang, A. L. Koh, W. Dang, J. Yin, M. Wang, C. Tan, T. Li, Z. Tan, Z. Liu, and H. Peng, *Clean Transfer of Large Graphene Single Crystals for High-Intactness Suspended Membranes and Liquid Cells*, Adv. Mater. **29**, 1700639 (2017).

[146]   L. Lin, J. Zhang, H. Su, J. Li, L. Sun, Z. Wang, F. Xu, C. Liu, S. Lopatin, Y. Zhu, K. Jia, S. Chen, D. Rui, J. Sun, R. Xue, P. Gao, N. Kang, Y. Han, H. Q. Xu, Y. Cao, K. S. Novoselov, Z. Tian, B. Ren, H. Peng, and Z. Liu, *Towards Super-Clean Graphene*, Nat. Commun. **10**, 1 (2019).

[147]   K. Kang, D. Abdula, D. G. Cahill, and M. Shim, *Lifetimes of Optical Phonons in Graphene and Graphite by Time-Resolved Incoherent Anti-Stokes Raman Scattering*, Phys. Rev. B **81**, 165405 (2010).

[148]   S. Wu, W.-T. Liu, X. Liang, P. J. Schuck, F. Wang, Y. R. Shen, and M. Salmeron, *Hot Phonon Dynamics in Graphene*, Nano Lett. **12**, 5495 (2012).

[149]   N. Bonini, M. Lazzeri, N. Marzari, and F. Mauri, *Phonon Anharmonicities in Graphite and Graphene*, Phys. Rev. Lett. **99**, 176802 (2007).

[150]   L. M. Malard, K. F. Mak, A. H. C. Neto, N. M. R. Peres, and T. F. Heinz, *Observation of Intra- and Inter-Band Transitions in the Transient Optical Response of Graphene*, New J. Phys. **15**, 015009 (2013).

[151]   L. Huang, B. Gao, G. Hartland, M. Kelly, and H. Xing, *Ultrafast Relaxation of Hot Optical Phonons in Monolayer and Multilayer Graphene on Different Substrates*, Surf. Sci. **605**, 1657 (2011).

[152]   J. K. Viljas and T. T. Heikkilä, *Electron-Phonon Heat Transfer in Monolayer and Bilayer Graphene*, Phys. Rev. B **81**, 245404 (2010).

[153]   T. Sohier, M. Calandra, C.-H. Park, N. Bonini, N. Marzari, and F. Mauri, *Phonon-Limited Resistivity of Graphene by First-Principles Calculations: Electron-Phonon Interactions, Strain-Induced Gauge Field, and Boltzmann Equation*, Phys. Rev. B **90**, 125414 (2014).

[154]   A. F. Page, J. M. Hamm, and O. Hess, *Polarization and Plasmons in Hot Photoexcited Graphene*, Phys. Rev. B **97**, 045428 (2018).

[155]   K. Ni, J. Du, J. Yang, S. Xu, X. Cong, N. Shu, K. Zhang, A. Wang, F. Wang, L. Ge, J. Zhao, Y. Qu, K. S. Novoselov, P. Tan, F. Su, and Y. Zhu,

Stronger Interlayer Interactions Contribute to Faster Hot Carrier Cooling of Bilayer Graphene under Pressure, Phys. Rev. Lett. **126**, 027402 (2021).

[156]   Ch. Wohlfahrt, *2 Pure Liquids: Data*, in *Static Dielectric Constants of Pure Liquids and Binary Liquid Mixtures*, edited by O. Madelung, Vol. 6 (Springer-Verlag, Berlin/Heidelberg, 1991), pp. 5–228.

[157]   G. Jnawali, Y. Rao, H. Yan, and T. F. Heinz, *Observation of a Transient Decrease in Terahertz Conductivity of Single-Layer Graphene Induced by Ultrafast Optical Excitation*, Nano Lett. **13**, 524 (2013).

[158]   A. J. Frenzel, C. H. Lui, W. Fang, N. L. Nair, P. K. Herring, P. Jarillo-Herrero, J. Kong, and N. Gedik, *Observation of Suppressed Terahertz Absorption in Photoexcited Graphene*, Appl. Phys. Lett. **102**, 113111 (2013).

[159]   H. I. Wang, M.-L. Braatz, N. Richter, K.-J. Tielrooij, Z. Mics, H. Lu, N.-E. Weber, K. Müllen, D. Turchinovich, M. Kläui, and M. Bonn, *Reversible Photochemical Control of Doping Levels in Supported Graphene*, J. Phys. Chem. C **121**, 4083 (2017).

[160]   H. A. Hafez, X. Chai, Y. Sekine, M. Takamura, K. Oguri, I. Al-Naib, M. M. Dignam, H. Hibino, and T. Ozaki, *Effects of Environmental Conditions on the Ultrafast Carrier Dynamics in Graphene Revealed by Terahertz Spectroscopy*, Phys. Rev. B **95**, 165428 (2017).

[161]   H. Yan, F. Xia, W. Zhu, M. Freitag, C. Dimitrakopoulos, A. A. Bol, G. Tulevski, and P. Avouris, *Infrared Spectroscopy of Wafer-Scale Graphene*, ACS Nano **5**, 9854 (2011).

[162]   M. Kim, S. G. Xu, A. I. Berdyugin, A. Principi, S. Slizovskiy, N. Xin, P. Kumaravadivel, W. Kuang, M. Hamer, R. Krishna Kumar, R. V. Gorbachev, K. Watanabe, T. Taniguchi, I. V. Grigorieva, V. I. Fal'ko, M. Polini, and A. K. Geim, *Control of Electron-Electron Interaction in Graphene by Proximity Screening*, Nat. Commun. **11**, 1 (2020).

[163]   N. Nandi, K. Bhattacharyya, and B. Bagchi, *Dielectric Relaxation and Solvation Dynamics of Water in Complex Chemical and Biological Systems*, Chem. Rev. **100**, 2013 (2000).

[164]   D. Ben-Yaakov, D. Andelman, and R. Podgornik, *Dielectric Decrement as a Source of Ion-Specific Effects*, J. Chem. Phys. **134**, 074705 (2011).

[165]   A. Chandra, *Static Dielectric Constant of Aqueous Electrolyte Solutions: Is There Any Dynamic Contribution?*, J. Chem. Phys. **113**, 903 (2000).

[166]   A. Schlaich, E. W. Knapp, and R. R. Netz, *Water Dielectric Effects in Planar Confinement*, Phys. Rev. Lett. **117**, 048001 (2016).

[167]   C. Zhang, F. Gygi, and G. Galli, *Strongly Anisotropic Dielectric Relaxation of Water at the Nanoscale*, J. Phys. Chem. Lett. **4**, 2477 (2013).

[168]   J. N. Israelachvili and R. M. Pashley, *Molecular Layering of Water at Surfaces and Origin of Repulsive Hydration Forces*, Nature **306**, 5940 (1983).

[169]   M. F. Toney, J. N. Howard, J. Richer, G. L. Borges, J. G. Gordon, O. R. Melroy, D. G. Wiesler, D. Yee, and L. B. Sorensen, *Voltage-Dependent Ordering of Water Molecules at an Electrode–Electrolyte Interface*, Nature **368**, 6470 (1994).

[170]   J.-J. Velasco-Velez, C. H. Wu, T. A. Pascal, L. F. Wan, J. Guo, D. Prendergast, and M. Salmeron, *The Structure of Interfacial Water on Gold Electrodes Studied by X-Ray Absorption Spectroscopy*, Science **346**, 831 (2014).

[171]   L. Fumagalli, A. Esfandiar, R. Fabregas, S. Hu, P. Ares, A. Janardanan, Q. Yang, B. Radha, T. Taniguchi, K. Watanabe, G. Gomila, K. S. Novoselov, and A. K. Geim, *Anomalously Low Dielectric Constant of Confined Water*, Science **360**, 1339 (2018).

[172]   W. Fu, L. Jiang, E. P. van Geest, L. M. C. Lima, and G. F. Schneider, *Sensing at the Surface of Graphene Field-Effect Transistors*, Adv. Mater. **29**, 1603610 (2017).

[173]   R. Pfattner, A. M. Foudeh, S. Chen, W. Niu, J. R. Matthews, M. He, and Z. Bao, *Dual-Gate Organic Field-Effect Transistor for PH Sensors with Tunable Sensitivity*, Adv. Electron. Mater. **5**, 1800381 (2019).

[174]   Y. Shao, J. Wang, H. Wu, J. Liu, I. A. Aksay, and Y. Lin, *Graphene Based Electrochemical Sensors and Biosensors: A Review*, Electroanalysis **22**, 1027 (2010).

[175]   Y. Liu, X. Dong, and P. Chen, *Biological and Chemical Sensors Based on Graphene Materials*, Chem. Soc. Rev. **41**, 2283 (2012).

[176]   G. Kucinskis, G. Bajars, and J. Kleperis, *Graphene in Lithium Ion Battery Cathode Materials: A Review*, J. Power Sources **240**, 66 (2013).

[177]   X. Wang, L. Zhi, and K. Müllen, *Transparent, Conductive Graphene Electrodes for Dye-Sensitized Solar Cells*, Nano Lett. **8**, 323 (2008).

[178]   Z. Weng, Y. Su, D.-W. Wang, F. Li, J. Du, and H.-M. Cheng, *Graphene–Cellulose Paper Flexible Supercapacitors*, Adv. Energy Mater. **1**, 917 (2011).

[179]   Z. Liu, H. I. Wang, A. Narita, Q. Chen, Z. Mics, D. Turchinovich, M. Kläui, M. Bonn, and K. Müllen, *Photoswitchable Micro-Supercapacitor Based on a Diarylethene-Graphene Composite Film*, J. Am. Chem. Soc. **139**, 9443 (2017).

[180]   A. Das, S. Pisana, B. Chakraborty, S. Piscanec, S. K. Saha, U. V. Waghmare, K. S. Novoselov, H. R. Krishnamurthy, A. K. Geim, A. C. Ferrari, and A. K. Sood, *Monitoring Dopants by Raman Scattering in an Electrochemically Top-Gated Graphene Transistor*, Nat. Nanotechnol. **3**, 210 (2008).

[181]   A. K. M. Newaz, Y. S. Puzyrev, B. Wang, S. T. Pantelides, and K. I. Bolotin, *Probing Charge Scattering Mechanisms in Suspended Graphene by Varying Its Dielectric Environment*, Nat. Commun. **3**, 734 (2012).

[182]   P. Sharma and Z. L. Mišković, *Ionic Screening of Charged Impurities in Electrolytically Gated Graphene: A Partially Linearized Poisson-Boltzmann Model*, J. Chem. Phys. **143**, 134118 (2015).

[183]   G. Hu, G. P. Pandey, Q. Liu, R. S. Anaredy, C. Ma, M. Liu, J. Li, S. K. Shaw, and J. Wu, *Self-Organization of Ions at the Interface between Graphene and Ionic Liquid DEME-TFSI*, ACS Appl. Mater. Interfaces **9**, 35437 (2017).

[184]   S. C. O'Hern, M. S. H. Boutilier, J.-C. Idrobo, Y. Song, J. Kong, T. Laoui, M. Atieh, and R. Karnik, *Selective Ionic Transport through Tunable Subnanometer Pores in Single-Layer Graphene Membranes*, Nano Lett. **14**, 1234 (2014).

[185]   J. L. Achtyl, R. R. Unocic, L. Xu, Y. Cai, M. Raju, W. Zhang, R. L. Sacci, I. V. Vlassiouk, P. F. Fulvio, P. Ganesh, D. J. Wesolowski, S. Dai, A. C. T. van Duin, M. Neurock, and F. M. Geiger, *Aqueous Proton Transfer across Single-Layer Graphene*, Nat. Commun. **6**, 6539 (2015).

[186]   A. Esfandiar, B. Radha, F. C. Wang, Q. Yang, S. Hu, S. Garaj, R. R. Nair, A. K. Geim, and K. Gopinadhan, *Size Effect in Ion Transport through Angstrom-Scale Slits*, Science **358**, 511 (2017).

[187]   S. Hu, M. Lozada-Hidalgo, F. C. Wang, A. Mishchenko, F. Schedin, R. R. Nair, E. W. Hill, D. W. Boukhvalov, M. I. Katsnelson, R. a. W. Dryfe, I. V. Grigorieva, H. A. Wu, and A. K. Geim, *Proton Transport through One-Atom-Thick Crystals*, Nature **516**, 227 (2014).

[188]   R. A. Nistor, M. A. Kuroda, A. A. Maarouf, and G. J. Martyna, *Doping of Adsorbed Graphene from Defects and Impurities in SiO_2 Substrates*, Phys Rev B **86**, 041409 (2012).

[189] S. Ryu, L. Liu, S. Berciaud, Y.-J. Yu, H. Liu, P. Kim, G. W. Flynn, and L. E. Brus, *Atmospheric Oxygen Binding and Hole Doping in Deformed Graphene on a SiO2 Substrate*, Nano Lett. **10**, 4944 (2010).

[190] S. M. Hornett, M. Heath, D. W. Horsell, and E. Hendry, *Optically Induced Oxygen Desorption from Graphene Measured Using Femtosecond Two-Pulse Correlation*, Phys Rev B **90**, 081401 (2014).

[191] A. Piazza, F. Giannazzo, G. Buscarino, G. Fisichella, A. L. Magna, F. Roccaforte, M. Cannas, F. M. Gelardi, and S. Agnello, *Graphene P-Type Doping and Stability by Thermal Treatments in Molecular Oxygen Controlled Atmosphere*, J. Phys. Chem. C **119**, 22718 (2015).

[192] B. E. Conway, *Ionic Hydration in Chemistry and Biophysics* (1981).

[193] J. Feng, K. Liu, M. Graf, D. Dumcenco, A. Kis, M. Di Ventra, and A. Radenovic, *Observation of Ionic Coulomb Blockade in Nanopores*, Nat. Mater. **15**, 850 (2016).

[194] R. C. Rollings, A. T. Kuan, and J. A. Golovchenko, *Ion Selectivity of Graphene Nanopores*, Nat. Commun. **7**, 11408 (2016).

[195] L. Chen, G. Shi, J. Shen, B. Peng, B. Zhang, Y. Wang, F. Bian, J. Wang, D. Li, Z. Qian, G. Xu, G. Liu, J. Zeng, L. Zhang, Y. Yang, G. Zhou, M. Wu, W. Jin, J. Li, and H. Fang, *Ion Sieving in Graphene Oxide Membranes via Cationic Control of Interlayer Spacing*, Nature **550**, 380 (2017).

[196] S. Friesen, G. Hefter, and R. Buchner, *Cation Hydration and Ion Pairing in Aqueous Solutions of MgCl2 and CaCl2*, J. Phys. Chem. B **123**, 891 (2019).

[197] G. Kresse and J. Furthmüller, *Efficiency of Ab-Initio Total Energy Calculations for Metals and Semiconductors Using a Plane-Wave Basis Set*, Comput. Mater. Sci. **6**, 15 (1996).

[198] G. Kresse and J. Furthmüller, *Efficient Iterative Schemes for Ab Initio Total-Energy Calculations Using a Plane-Wave Basis Set*, Phys. Rev. B **54**, 11169 (1996).

[199] J. P. Perdew, K. Burke, and M. Ernzerhof, *Generalized Gradient Approximation Made Simple*, Phys. Rev. Lett. **77**, 3865 (1996).

[200] P. E. Blöchl, *Projector Augmented-Wave Method*, Phys. Rev. B **50**, 17953 (1994).

[201] A. F. Wright and A. J. Leadbetter, *The Structures of the β-Cristobalite Phases of SiO2 and AlPO4*, Philos. Mag. J. Theor. Exp. Appl. Phys. **31**, 1391 (1975).

[202]   J. Yang, S. Meng, L. Xu, and E. G. Wang, *Water Adsorption on Hydroxylated Silica Surfaces Studied Using the Density Functional Theory*, Phys. Rev. B **71**, 035413 (2005).

[203]   X. F. Fan, W. T. Zheng, V. Chihaia, Z. X. Shen, and J.-L. Kuo, *Interaction between Graphene and the Surface of SiO$_2$*, J. Phys. Condens. Matter **24**, 305004 (2012).

[204]   F. Vigné-Maeder and P. Sautet, *Theoretical Study of Hydroxylated and Dehydroxylated Surfaces of a Cristobalite Model of Silica*, J. Phys. Chem. B **101**, 8197 (1997).

[205]   D. Ceresoli, M. Bernasconi, S. Iarlori, M. Parrinello, and E. Tosatti, *Two-Membered Silicon Rings on the Dehydroxylated Surface of Silica*, Phys. Rev. Lett. **84**, 3887 (2000).

[206]   D. Ricci and G. Pacchioni, *Structure of Ultrathin Crystalline SiO$_2$ Films on Mo(112)*, Phys. Rev. B **69**, 161307 (2004).

[207]   J. Peri and A. Hensley Jr, *The Surface Structure of Silica Gel*, J. Phys. Chem. **72**, 2926 (1968).

[208]   D. W. Sindorf and G. E. Maciel, *Silicon-29 NMR Study of Dehydrated/Rehydrated Silica Gel Using Cross Polarization and Magic-Angle Spinning*, J. Am. Chem. Soc. **105**, 1487 (1983).

[209]   K. Muthukumar, I. Opahle, J. Shen, H. O. Jeschke, and R. Valentí, *Interaction of W(CO)$_6$ with SiO$_2$ Surfaces: A Density Functional Study*, Phys. Rev. B **84**, 205442 (2011).

Acknowledgments

During my PhD and writing of this thesis, many people have helped and supported me. I want to express my thanks to my supervisors, collaborators, teammates, friends, and family.

First, I am most indebted to my supervisor, Prof. Dr. Mischa Bonn, for offering me such a fantastic opportunity to perform my research in a world-leading institute. It is a wonderful experience to work in his department. Mischa's inspirational guidance on scientific ideas helped me make directions in the past three years. His role model as a successful scientist will keep me going for years to come.

Great thanks to Dr. Hai Wang. He is a great person to work with and to learn from. His dedication and passion for science influenced me as a source of enthusiasm. I was impressed by the first months we worked together that Hai joined and instructed me in the lab whenever I need. He always provided smart solutions to problems in all stages of my PhD. Exchanging ideas with Hai on both research and life shaped my growth to a more logical thinker with a determined personality.

I am fortunate to have Dr. Klaas-Jan Tielrooij as my co-supervisor. I enjoyed the enlightening discussions with him and was amazed by his insights and deep understanding of his topics. I want to thank Klaas for having me spend some time in his group in Barcelona. That three-month visit inspired me with some proper ways to do research – down-to-earth hard work and intelligent problem solving by applying knowledge and experience.

Part of the experiments and simulations described in this thesis was in productive collaborations with some remarkable people worldwide. I thank them for their openness and cooperation. Dr. Jincan Zhang and Prof. Dr. Hailin Peng, from Peking University, provided their unique and outstanding sample and coordinated the STEM measurements presented in Chapter 3. Min Hu and Prof. Dr. Jun Jiang, from USTC, run the first-principle simulations to support my experimental results theoretically in Chapter 5. Dr. Alessandro Principi, at the University of Manchester, developed the analytical model to describe the hot-carrier cooling dynamics in graphene in Chapter 3. Dr. Alexander Block, at ICN2, run the TA measurements mentioned in Chapter 3. Karuppasamy Soundarapandian and Prof. Dr. Frank H. L. Koppens, at ICFO, provided some graphene samples and shared their preparation methods. Dr. Zhaoyang Liu and Dr. Zongping Chen also provided some graphene samples.

Next, I would like to give a big thanks to Laurie, one of the most helpful and influential people, along with my time at MPIP. We are in connection since the first day I got in touch with the group. Your assistance and support made everything eventually possible.

MAINZ Graduate School of Excellence was the stepping-stone to my PhD in Germany. The summer school, student seminars, and soft-skill workshops are great opportunities for me to integrate myself into such a warm international big family. I want to thank Dr. Michael Fuchs for his suggestions and assistance. Later, I was delighted to join a second graduate school – MPGC. It was a fabulous memory to expand my network in it.

My fellow Low-dimensional Stars are incredible. Working together with them is of great pleasure. I wish them all the best in their future. They are Heng Zhang, Wenhao Zheng, Shuai Fu, Lucia Di Virgilio, Shuai Chen, Sven Krasel,

It must be a challenge to list everyone I benefited from during my PhD. With this, I apologize if I missed some names.

Finally, I thank my parents and friends who always care about and encourage me.

Publication List

Publications covered in this thesis

Chapter 3 – Eva A. A. Pogna, **Xiaoyu Jia**, Alessandro Principi, Alexander Block, Luca Banszerus, Jincan Zhang, Xiaoting Liu, Thibault Sohier, Stiven Forti, Karuppasamy Soundarapandian, Bernat Terrés, Jake D. Mehew, Chiara Trovatello, Camilla Coletti, Frank H. L. Koppens, Mischa Bonn, Hai I. Wang, Niek van Hulst, Matthieu J. Verstraete, Hailin Peng, Zhongfan Liu, Christoph Stampfer, Giulio Cerullo, and Klaas-Jan Tielrooij "*Hot-Carrier Cooling in High-Quality Graphene is Intrinsically Limited by Optical Phonons*" (Submitted) arXiv:2103.03527 (Preprint)

Chapter 4 – Xiaoyu Jia, Mischa Bonn, Klaas-Jan Tielrooij, Hai I. Wang "*Controlling Hot-carrier Cooling Dynamics by Solvent Dielectrics*" (In preparation)

Chapter 5 – Xiaoyu Jia, Min Hu, Karuppasamy Soundarapandian, Xiaoqing Yu, Zhaoyang Liu, Zongping Chen, Akimitsu Narita, Klaus Müllen, Frank H. L. Koppens, Jun Jiang, Klaas-Jan Tielrooij, Mischa Bonn, and Hai I. Wang "*Kinetic Ionic Permeation and Interfacial Doping of Supported Graphene*" Nano Letters 2019, 19, 12, 9029-9036.

Other publications during PhD

Haibing Xie, Zaiwei Wang, Zehua Chen, Carlos Pereyra, Mike Pols, Krzysztof Gałkowski, Miguel Anaya, Shuai Fu, **Xiaoyu Jia**, Pengyi Tang,

Dominik Józef Kubicki, Anand Agarwalla, Hui-Seon Kim, Daniel Prochowicz, Xavier Borrisé, Mischa Bonn, Chunxiong Bao, Xiaoxiao Sun, Shaik Mohammed Zakeeruddin, Lyndon Emsley, Jordi Arbiol, Feng Gao, Fan Fu, Hai I. Wang, Klaas-Jan Tielrooij, Samuel D. Stranks, Shuxia Tao, Michael Grätzel, Anders Hagfeldt, and Monica Lira-Cantu "*Decoupling the Effects of Defects on Efficiency and Stability through Phosphonates in Stable Halide Perovskite Solar Cells*" Joule 2021, 5 (5), 1246-1266.

Shuai Fu, Indy du Fossé, **Xiaoyu Jia**, Jingyin Xu, Xiaoqing Yu, Heng Zhang, Wenhao Zheng, Sven Krasel, Zongping Chen, Zhiming M. Wang, Klaas-Jan Tielrooij, Mischa Bonn, Arjan J. Houtepen, and Hai I. Wang "*Long-Lived Charge Separation Following Pump-Energy Dependent Ultrafast Charge Transfer in Graphene/WS$_2$*" Science Advances 2021, 7 (9), eabd9061.

Jan-Christoph Deinert, David Alcaraz Iranzo, Raul Perez, **Xiaoyu Jia**, Hassan A. Hafez, Igor Ilyakov, Nilesh Awari, Min Chen, Mohammed Bawatna, Alexey N. Ponomaryov, Semyon Germanskiy, Mischa Bonn, Frank H.L. Koppens, Dmitry Turchinovich, Michael Gensch, Sergey Kovalev, and Klaas-Jan Tielrooij "*Grating-graphene metamaterial as a platform for terahertz nonlinear photonics*" ACS Nano 2021, 15, 1, 1145-1154.

Weixiang Ye, Katja Krüger, Ana Sánchez-Iglesias, Isabel García, **Xiaoyu Jia**, Johannes Sutter, Sirin Celiksoy, Benjamin Foerster, Luis M. Liz-Marzán, Rubén Ahijado-Guzmán, and Carsten Sönnichsen "*CTAB Stabilizes Silver on Gold Nanorods*" Chem. Mater. 2020, 32, 4, 1650-1656.

T. P. Ying, M. X. Wang, X. X. Wu, Z. Y. Zhao, Z. Z. Zhang, B. Q. Song, Y. C. Li, B. Lei, Q. Li, Y. Yu, E. J. Cheng, Z. H. An, Y. Zhang, **X. Y. Jia**, W. Yang, X. H. Chen, and S. Y. Li "*Discrete Superconducting Phases in FeSe-Derived Superconductors*" Physical Review Letters 2018, 121 (20), 207003.